

**ELECTROMAGNETIC MODELING OF PORPHYRY  
SYSTEMS FROM THE GRAIN-SCALE TO THE  
DEPOSIT-SCALE USING THE GENERALIZED  
EFFECTIVE MEDIUM THEORY OF  
INDUCED POLARIZATION**

by

Abraham M. Emond

A thesis submitted to the faculty of  
The University of Utah  
in partial fulfillment of the requirements for the degree of

Master of Science

in

Geophysics

Department of Geology and Geophysics

The University of Utah

December 2007

Copyright © Abraham M. Emond 2007

All Rights Reserved

THE UNIVERSITY OF UTAH GRADUATE SCHOOL

## SUPERVISORY COMMITTEE APPROVAL

of a thesis submitted by

Abraham M. Emond

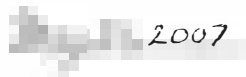
This thesis has been read by each member of the following supervisory committee and by majority vote has been found to be satisfactory.



Chair: Michael Zhdanov



David S. Chapman

 2007

Erich U. Petersen


THE UNIVERSITY OF UTAH GRADUATE SCHOOL

## FINAL READING APPROVAL

To the Graduate Council of the University of Utah:

I have read the thesis of Abraham M. Emond in its final form and have found that (1) its format, citations and bibliographic style are consistent and acceptable; (2) its illustrative materials including figures, tables and charts are in place; and (3) the final manuscript is satisfactory to the supervisory committee and is ready for submission to The Graduate School.


  
Date

  
Zhdanov  
Chair, Supervisory Committee

Approved for the Major Department

  
Marjorie A. Chan  
Chair

Approved for the Graduate Council

  
David S. Chapman  
Dean of The Graduate School

## ABSTRACT

A new conductivity model, the Generalized Effective Medium Theory of Induced Polarization (GEMTIP) is tested with complex resistivity data and detailed mineralogy of porphyry system rock samples. The induced polarization (IP) effects are important phenomena for EM exploration. GEMTIP represents an expansion of the rock properties used for electromagnetic modeling of bulk apparent resistivity. The new model includes, mineral type, mineral size, mineral conductivity and other petrographic information. Rocks containing disseminated sulfides from porphyry systems are chosen as a good analog to the testing of the spherical grain analytic solution of GEMTIP. GEMTIP predicts the same trend in peak IP response as function of grain size for both chalcopyrite and pyrite containing synthetic rocks as a previous study. Inversion routines are developed and tested using synthetic data to recover the two empirical variables from recorded complex resistivity data. The two empirical variables are surface polarizability ( $\alpha$ ) and the decay coefficient ( $C$ ). For three porphyry system rock samples, detailed geologic analysis using optical mineralogy, and X-ray tomography is conducted to determine GEMTIP model inputs. Sulfides in the rock samples exhibited a range of forms including near perfect cubes, stacked cubes, rounded, and complex amorphous forms. The sizes of sulfides varied from less than 0.01 mm to over 2 mm in radius. Measured surface area and surface area to volume ratios for each sample do not match the computed values assuming uniform spherical grains. Complex resistivity values are calculated from recorded EM data from 0.0156 Hz to 9216 Hz. Using the observed mineralogical data the GEMTIP model was able to fit the recorded complex resistivity data for the three samples with the inclusion of an empirical factor to account for the difference in measured and computed spherical surface area reinforcing the role of

surface area in the IP effect. Successful GEMTIP modeling of the rock samples provided insight into controlling factors of the IP effect.

Forward geophysical modeling of copper porphyry systems is accomplished using geologic inputs from rock-scale to deposit-scale. For deposit scale modeling an Integral Equation method Electromagnetic forward modeling code IBCEM3DIP, developed by the Consortium for Electromagnetic Modeling and Inversion (CEMI) is used. A new interface to allow modeling of geometrically complex geologic systems was developed for the IBCEM3DIP code. The GEMTIP conductivity model was incorporated into IBCEM3DIP. Both the rock type and associated electric properties and mineralogical properties (approximate) are used for synthetic data creation. Using the new interface and developed Simplified Porphyry Model as a template the effect of deposit-scale changes in sulfide distribution are tested on synthetic IP data. Although differences in the apparent resistivity data are subtle, changes in sulfide distribution strongly influence the apparent phase data. This highlights the importance of IP data and its use for mineral discrimination. With advances in the understanding of the IP effect through GEMTIP, forward modeling and inversion, detection and discrimination capability will improve for porphyry systems and other geologic targets, leading to greater efficiency in mineral exploration.

## CONTENTS

<b>ABSTRACT</b> .....	<b>iv</b>
<b>LIST OF TABLES</b> .....	<b>viii</b>
<b>ACKNOWLEDGMENTS</b> .....	<b>ix</b>
<b>1. OVERVIEW OF THE PRINCIPLES, APPLICATION, AND MODELING OF THE INDUCED POLARIZATION EFFECT</b>	<b>1</b>
1.1 Introduction .....	1
1.2 The Induced Polarization Effect .....	1
1.3 Time Domain Chargeability and the Frequency Effect .....	3
1.4 Conductivity Models .....	7
1.5 Application .....	11
1.6 Summary .....	16
<b>2. TESTING THE GENERALIZED EFFECTIVE MEDIUM THEORY OF INDUCED POLARIZATION WITH PORPHYRY ANALOGS</b> .....	<b>17</b>
2.1 Introduction .....	17
2.2 GEMTIP Overview .....	18
2.3 Comparison to 1978 Ostrander and Zonge Data .....	20
2.4 Alpha and C Inversion on Synthetic Data .....	21
2.5 Geologic Analog and Samples Chosen for Analysis .....	31
2.6 X-ray Microtomography .....	32
2.7 EM Measurements .....	37
2.8 GEMTIP Models of Rock Samples .....	45
<b>3. DEPOSIT SCALE MODELING OF A PORPHYRY SYSTEM, GEMTIP APPLICATION ON A LARGE SCALE</b> .....	<b>60</b>
3.1 Introduction .....	60
3.2 Porphyry Overview .....	61
3.3 Simple Porphyry Model Development .....	61
3.4 GEMTIP Incorporation into INTEM .....	62
3.5 Simple Porphyry Model Front End .....	63
3.6 Deposit Scale Forward Modeling .....	64

4. CONCLUSIONS .....	77
4.1 Conclusions .....	77
4.2 Future Directions / Recommendations .....	78
APPENDICES	
A. EM DATA .....	79
B. ELECTRONIC DATA .....	83
REFERENCES.....	84



## LIST OF TABLES

1.1 Variables of Cole-Cole model described by Equation 1.5. . . . .	8
1.2 Maxwell equation variables from <i>Wong</i> [1979]. . . . .	10
1.3 Descriptive guide for GEMTIP parameters. . . . .	12
2.1 Descriptive guide for GEMTIP parameter. . . . .	19
2.2 Comparison of GEMTIP parameters for CEMI and <i>Ostrander and Zonge</i> [1978] . . . . .	25
2.3 Two-phase inversion GEMTIP variables. . . . .	27
2.4 Four-phase media inversion GEMTIP variables that produce good convergence. . . . .	28
2.5 Four-phase media inversion GEMTIP variables that produce poor convergence. . . . .	29
2.6 Two-phase N grain sizes inversion GEMTIP variables. . . . .	30
2.7 Sample mineralogical assessment summary. . . . .	36
2.8 Imaginary data shift to enable better inversion. . . . .	45
2.9 Variables for two-phase inversion of K01 for $3k$ . . . . .	47
2.10 Variables for N grain sizes one $\alpha$ one $C$ inversion of K01 for $5k$ . . . . .	50
2.11 Variables for two-phase inversion of M02 for $12k$ . . . . .	50
2.12 Variables for two-phase inversion of SB03 for $3k$ . . . . .	53
2.13 True surface area to volume ratios of samples K01, M02, and SB03 (pyrite and chalcopyrite). The trend in true SAVR follows the trend of multiples of $k$ used. There is good agreement between the multiple of $k$ used and $\frac{\text{true SAVR}}{\text{spherical SAVR}}$ for sample K01. . . . .	58
2.14 Geometric information for grains shown in Figure 2.33. Grain ID refers to the letter assigned in Figure 2.33. Surface area and volume were computed using marching cubes [ <i>Lorensen and Cline</i> , 1987]. . . . .	59
3.1 Geometry of 3-D porphyry model. . . . .	66
3.2 Modeling parameters and performance summary for synthetic data presented in Figures 3.8, 3.9, 3.10, and 3.11. . . . .	66
3.3 Geoelectric and mineralogic parameters for all Model 1. . . . .	68
3.4 Geoelectric and mineralogical parameters for all Models 2-4. . . . .	69

## ACKNOWLEDGMENTS

This work was supported by the Department of Energy and the following members of the MDCA project: BHP Billiton World Exploration Inc. Kennecott Exploration Company, Placer Dome, Phelps Dodge Mining Company, and Zonge Engineering and Research Organization Inc.

The author is thankful to Seong Kon Lee and Takumi Ueda for developing the INTEM3DIP forward modeling code.

A special thanks to Zonge Engineering and Research Organization Inc. for their help with EM measurements of the rock samples and to Dr. Lin and University of Utah Metallurgy department for the X-ray micro tomography data.

The author appreciates the support of the Consortium for Electromagnetic Modeling and Inversion (CEMI)

Support to attend and present research results at the Society of Economic Geologists, Wealth Creation in the Minerals Industry conference held May 2006 in Keystone Colorado was generously provided by the Society of Economic Geologists.

# CHAPTER 1

## OVERVIEW OF THE PRINCIPLES, APPLICATION, AND MODELING OF THE INDUCED POLARIZATION EFFECT

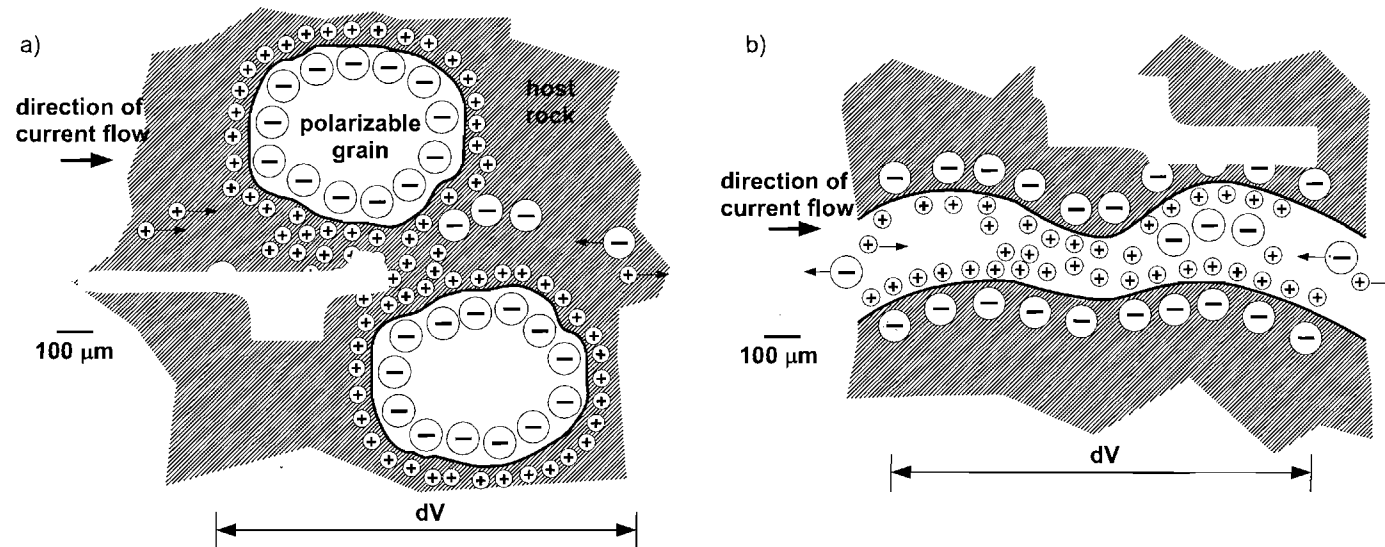
### 1.1 Introduction

The induced polarization (IP) effect is an important tool for mineral exploration and has been utilized for over 50 years. IP surveys can be more sensitive to mineralization, pore fluids, and more compared to DC resistivity surveys. The phenomenon was first noticed by Schlumberger in the early 20th century. The 1950s saw some of the first successful applications of the IP method and notable publications including the comprehensive *Overvoltage research and geophysical applications* by Wait [1959]. Over the years models have been proposed to describe the IP effect, the Cole-Cole model [Cole and Cole, 1941] first adopted by Pelton [Pelton et al., 1978] is a well-accepted empirical model. Most models describing the IP are empirical in contrast the newly developed Generalized Effective Medium Theory of IP by Zhdanov [2006] and tested in the following chapters. An overview of the IP phenomenon and selected applications and conductivity models is presented in this chapter.

### 1.2 The Induced Polarization Effect

The IP effect is thought to be caused by electrochemical reactions and charge build up at interfaces, grain boundaries, vein walls, and other boundaries. The polarizable behavior (IP effect) of a disseminated mineralization and a mineralized vein is shown in Figure 1.1.

This charge build up has a capacitive effect and can be seen in both time domain data shown by Figure 1.2 and in frequency domain data (Figure 1.3). The concepts



modified from Frazier 1964

**Figure 1.1.** Conceptual illustrations of surface polarization. a) Surface polarization of disseminated minerals in a uniformly conductive host rock. b) Surface polarization of a mineralized vein after *Frazier* [1964].

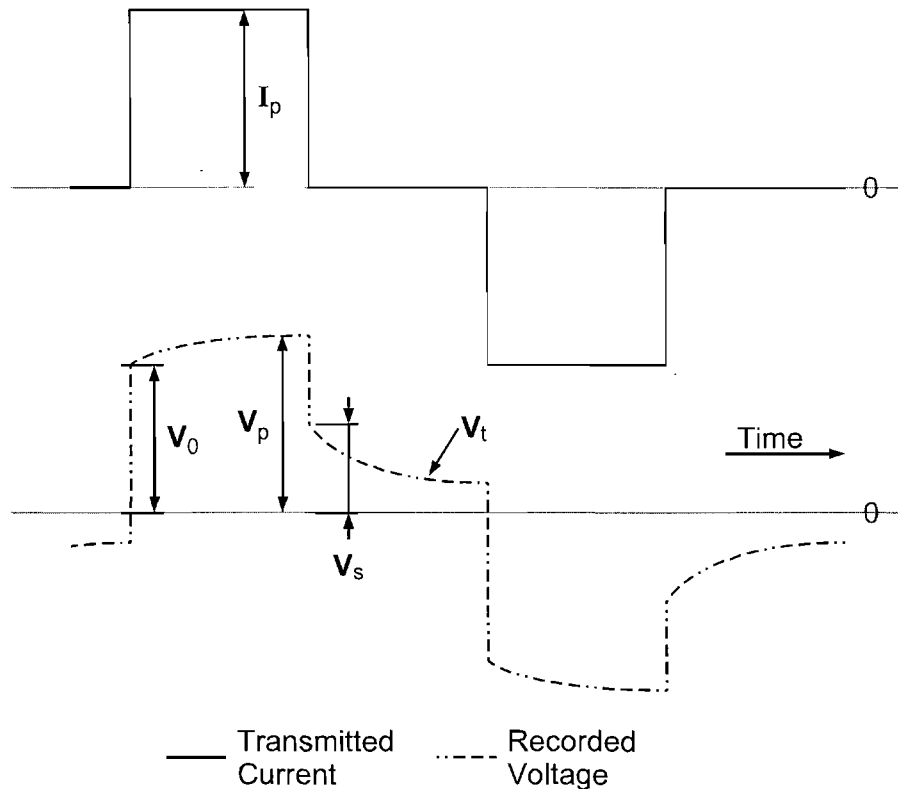


**Figure 1.2.** The IP effect on recorded time domain data after *Sumner* [1976]. Transmitted current waveform and resulting recorded voltage shown. The initial recorded voltage is smaller amplitude ( $V_0$ ) than the later recorded peak voltage ( $V_p$ ) is recorded. A secondary voltage ( $V_s$ ) is recorded after the transmitter turns off and decays over time ( $V_t$ ).

illustrated in Figure 1.3 can be expanded to the idea of complex resistivity as a function of frequency plotted in Figure 1.4. This complex behavior of resistivity can provide useful geologic information and has been modeled by several approaches.

### 1.3 Time Domain Chargeability and the Frequency Effect

[Time Domain Chargeability and the Frequency Effect] New interpretation techniques came about with the adoption of the IP method. Time domain chargeability, the Frequency Effect (FE), and the Percent FE, are notable and effective techniques still used today.

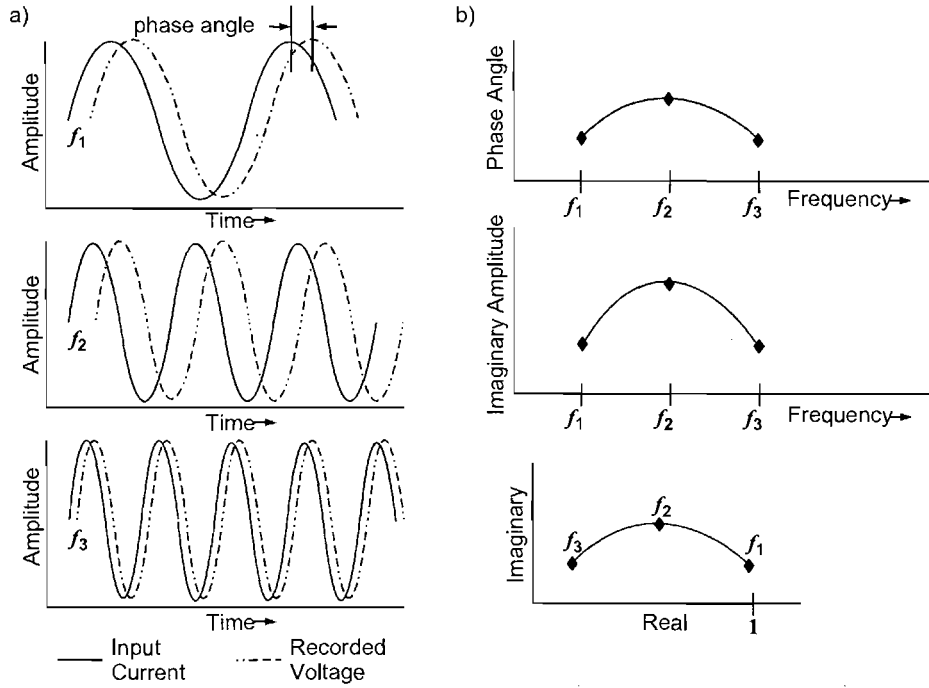


**Figure 1.3.** The IP effect in the frequency domain. a) Three transmitted waveforms of increasing frequency and the resulting phase shifted record voltages after *Sumner* [1976]. b) Three methods of viewing recorded data as a function of frequency: phase angle as a function of frequency, imaginary amplitude as a function of frequency, and normalized magnitude on the complex plain adopted by *Zonge et al.* [1972]. The recorded amplitude and resulting computed resistivity can be divided in real and imaginary parts using the phase angle and the appropriate trigonometric functions. The result is complex resistivity.

Chargeability in time domain ( $M$ ) refers to the discharge of the polarizable media and can be measured with two different methods. The first method is the ratio of the secondary voltage ( $V_s$ ) to the primary voltage ( $V_p$ ) shown by Equation 1.1 and illustrated in Figure 1.2 [*Sumner*, 1976]. The second method integrates the decaying secondary voltage ( $V_t$ ) over the time interval  $t_1$  to  $t_2$  and divides by the primary voltage ( $V_p$ ) expressed in Equation 1.2 [*Sumner*, 1976] (Figure 1.5). The first form of chargeability is given by

$$M = \frac{V_s}{V_p}. \quad (1.1)$$

Alternately, chargeability can be expressed as

pg 55  
Sumner 1976

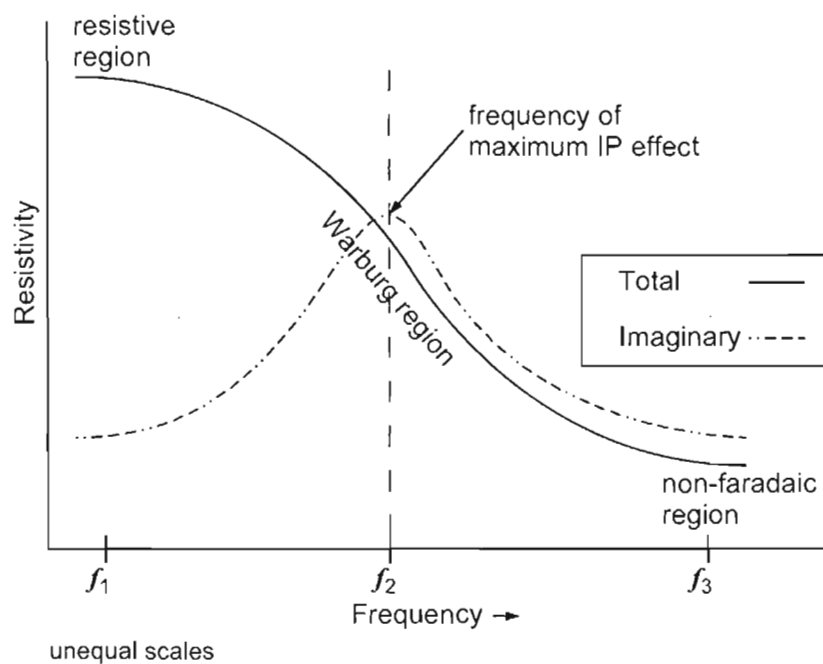


**Figure 1.4.** Complex resistivity as a function of frequency after Sumner [1976]. The three regions of resistivity are shown. Resistivity generally decays  $\frac{1}{f^2}$  in the Warburg region [Sumner, 1976]. The peak IP frequency is located where the imaginary resistivity is largest.

$$M = \frac{1}{V_p} \int_{t_2}^{t_1} V_t dt . \quad (1.2)$$

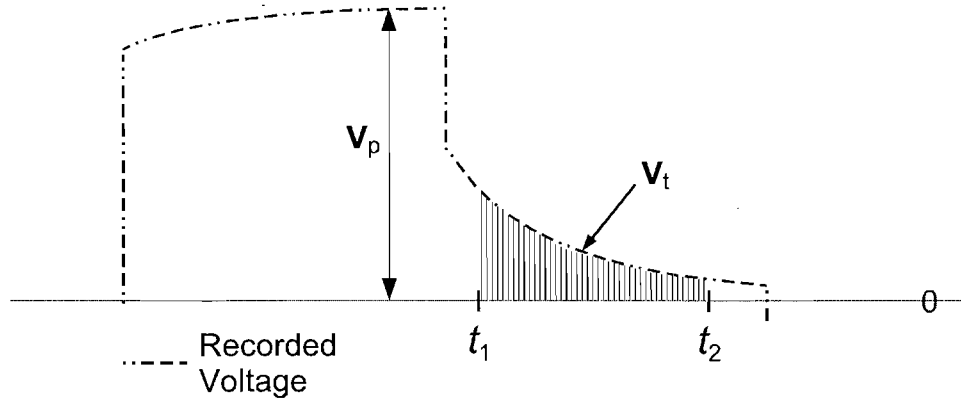


**Figure 1.5.** Integration of decay voltage ( $V_t$ ) after *Sumner* [1976].

The frequency effect ( $FE$ ) is determined from data of two different frequencies generally a decade apart [*Zonge et al.*, 1972]. Because differences in subsurface geology cause different perturbations in the observed data,  $FE$  can be useful for interpretation of IP data. The frequency effect found from

$$FE = \frac{V_2 - V_1}{V_1}, \quad (1.3)$$

or in terms of resistivity,

$$FE = \frac{\rho_2 - \rho_1}{\rho_1}. \quad (1.4)$$

The simplest form of  $FE$  compares the recorded voltages at two frequencies and is given by Equation 1.3. It can be expanded to Equation 1.4 by using the calculated apparent resistivity values. Percent  $FE$  is calculated multiplying  $FE$  by 100 [*Zonge et al.*, 1972].

The above interpretation techniques proved useful for obtaining geologic information and exploration, but did not attempt to describe the observed IP phenomena.



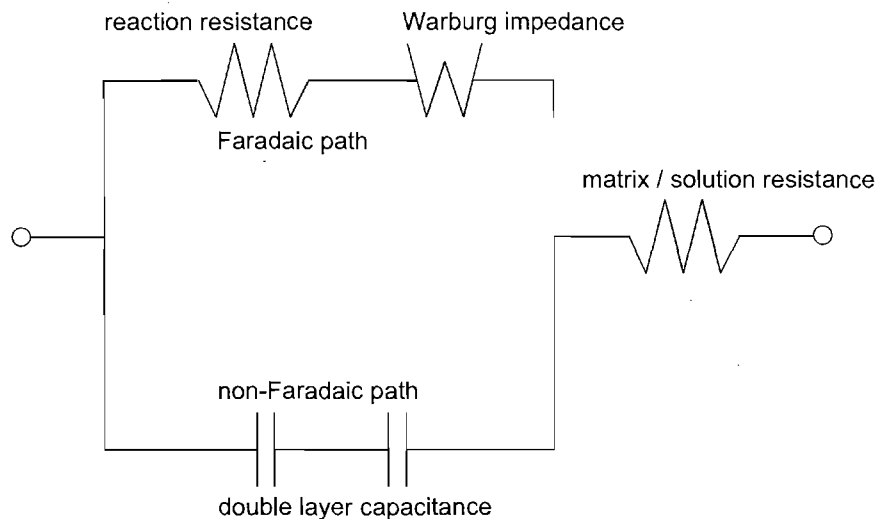


**Figure 1.6.** Equivalent circuit including Warburg impedance after *Sumner* [1976]. This circuit can describe the real resistivity depicted in Figure 1.4.

## 1.4 Conductivity Models

To describe the observed IP effect several conductivity models both empirical and theoretical have been developed. Five models including the newly developed GEMTIP model will be discussed below.

### 1.4.1 Warburg Impedance

To describe the observed decay in resistivity a simple equivalent circuit was developed with a Warburg impedance [*Sumner*, 1976]. The inclusion of this circuit element is shown in the circuit presented in Figure 1.6. The Warburg element allows the resistivity to decay as a function of the square root of frequency. The equivalent circuit containing the Warburg element can describe the behavior of the real resistivity in Figure 1.4. This model describes only the real behavior of resistivity.

### 1.4.2 Ostrander and Zonge

Ostrander and Zonge [*Ostrander and Zonge*, 1978] conducted an extensive study of the complex resistivity of disseminated sulfides. In addition to their study of

**Table 1.1.** Variables of Cole-Cole model described by Equation 1.5.

variable	units	explanation
$R_0$	Ohm-m	DC resistivity
$m$	-	chargeability
$\tau$	seconds	time constant
$C$	-	decay coefficient
$\omega$	Hertz	angular frequency

recorded data they formulated an electrochemical based model that described both the amplitude and phase of the recorded data as a function of the material. The Ostrander and Zonge model included ion valence, Faraday's constant, concentration of reactants at electrode interface (grain boundary), diffusion coefficient, the gas constant, temperature, and electrode (grain) surface area. Ostrander and Zonge found their model to describe their recorded data accurately.

### 1.4.3 Cole-Cole

The Cole-Cole model [Cole and Cole, 1941], incorporated by Pelton [Pelton et al., 1978] describes the complex resistivity (real and imaginary) of a mineralized rock with an equivalent circuit given in Figure 1.7. The frequency dependent complex resistivity of this circuit is given by

$$Z(\omega) = R_0 \left\{ 1 - m \left\{ 1 - \frac{1}{1 + \{i\omega\tau\}^C} \right\} \right\}. \quad (1.5)$$

and contains three empirical parameters: chargeability ( $m$ ), the time constant ( $\tau$ ), and the decay coefficient ( $C$ ) [Pelton et al., 1978]. Table 1.1 describes each variable in Equation 1.5. The effect of each of these parameters is shown in Figure 1.8. The terms  $m$ ,  $\tau$ , and  $C$  can be used with varying accuracy to determine subsurface geology [Pelton et al., 1978; Major and Silic, 1981]. Although widely accepted, this model describes bulk resistivity and does not account for rock structure or composition directly.

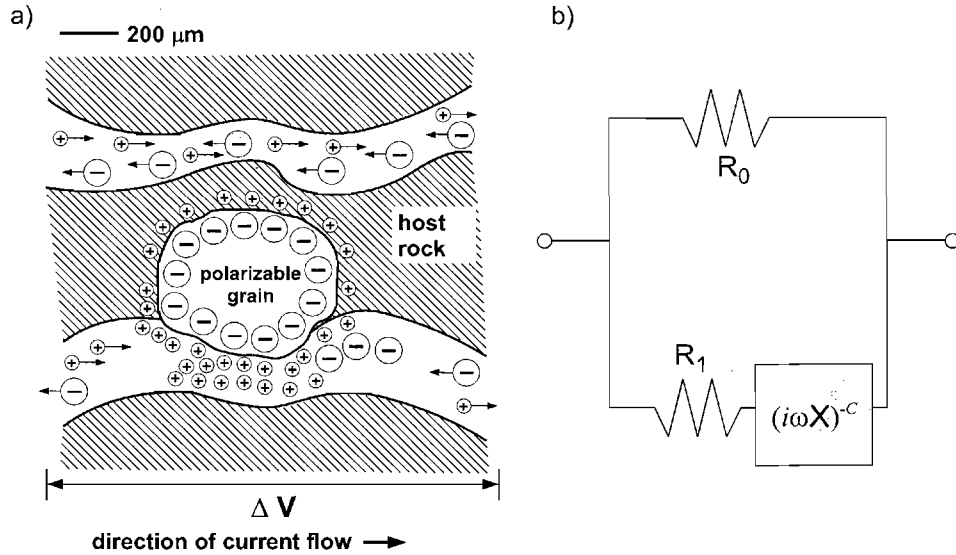


**Figure 1.7.** Cole-Cole model for mineralization after by *Pelton et al.* [1978]. a) Rock containing disseminated mineralization. The polarized grain impedes current flow acting like a capacitor. b) Equivalent circuit for the mineralized rock. Unobstructed current flow given by  $R_0$ . Frequency dependent current flow given by  $R_1$  and component  $[i\omega X]^{-C}$ . Equation 1.5 describes the behavior of this circuit.

#### 1.4.4 Wong Models

Complex electrochemical models for conductive spherical and prolate spheroidal grains to simulate sulfide mineralization were developed by *Wong* [1979] and *Wong and Strangway* [1981]. Both models expand on the Maxwell formula [*Maxwell*, 1891] given by

$$\frac{\sigma_e(j\omega)}{\sigma_0} = \frac{1 + 2vf(j\omega)}{1 - vf(j\omega)}. \quad (1.6)$$

Table 1.2 describes each variable in Equation 1.6. Equation 1.6 holds true if the disseminated phase volume fraction is less than 16 percent. Wong expands the formula to include disseminated mineralization of discrete sizes defining conductivity as

$$\frac{\sigma_e(j\omega)}{\sigma_0} = \frac{1 + 2\sum v_i f(j\omega; a_i)}{1 - \sum v_i f(j\omega; a_i)}. \quad (1.7)$$

The models contain numerous electrochemical, electromagnetic, and geologic variables. The spherical case includes volume fraction and grain radius while the prolate spheroidal case includes volume fraction and semimajor and semiminor

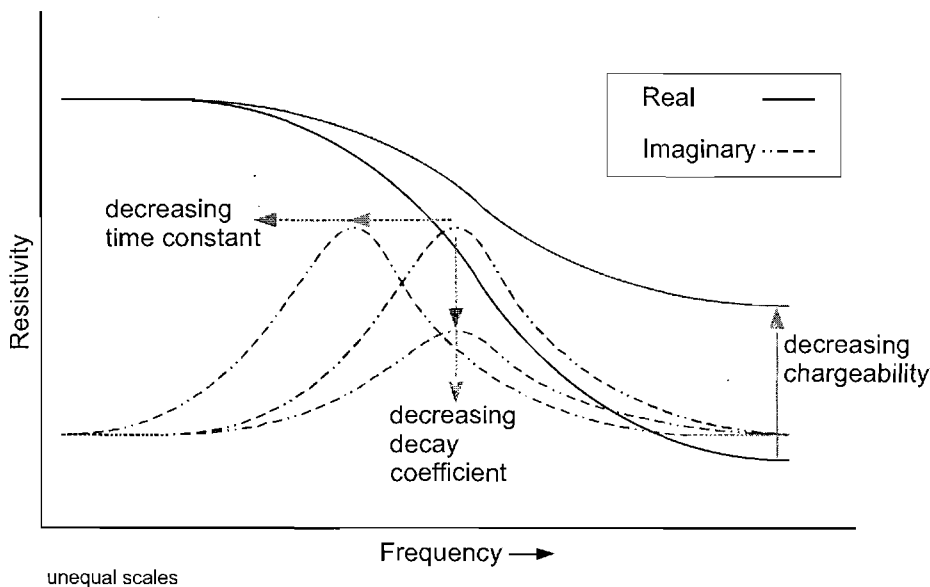


**Figure 1.8.** Complex resistivity behavior of the Cole-Cole model. The effect of changing chargeability ( $m$ ), time constant ( $\tau$ ), and decay coefficient ( $C$ ) from Equation 1.5 is illustrated.

**Table 1.2.** Maxwell equation variables from *Wong* [1979].

variable	units	explanation
$\sigma_e(j\omega)$	Ohm-m	effective complex conductivity
$\sigma_0$	Ohm-m	media conductivity
$v$	%	volume fraction
$f(\dots)$	-	frequency dependent reflection coefficient due to a sphere
$\omega$	Hertz	angular frequency

dimensions. For both models, *Wong* [1979] and *Wong and Strangway* [1981] were able to fit experimental data. *Mahan et al.* [1986] found the spherical case of *Wong's* model to describe recorded data well except at higher frequencies supporting the viability of the model, although it is limited to sulfide mineralization less than 16 percent by volume.

### 1.4.5 The Generalized Effective Medium Theory of IP

The Generalized Effective Medium Theory of IP (GEMTIP) is a new rigorous, mathematically formulated conductivity model constructed by *Zhdanov* [2005] and *Zhdanov* [2006]. This model uses Effective Medium theory to describe the complex resistivity of heterogeneous rocks. The GEMTIP conductivity model incorporates the physical and electrical characteristics of rocks at the grain scale into an analytic expression. These characteristics include grain size, grain shape, mineral conductivity, porosity, anisotropy, polarizability, mineral volume fraction, pore fluids, and more [*Zhdanov*, 2006]. The first analytic solution of this general theory is for spherical grains in a homogeneous matrix given by Equation 1.8. Each variable of the model is described in Table 1.3. The spherical solution of GEMTIP is tested in detail in later chapters and is able to model the IP effect on the rock scale. In principle this model could be used to determine mineralization or hydrocarbon saturation from recorded electrical data [*Zhdanov*, 2006].

$$\rho_{ef} = \rho_0 \left\{ 1 + \sum_{l=1}^N \left\{ f_l m_l \left\{ 1 - \frac{1}{1 + \{-i\omega\tau_l\}^{C_l}} \right\} \right\} \right\}^{-1}, \quad (1.8)$$

where:

$$m_l = 3 \frac{\rho_0 - \rho_l}{2\rho_l + \rho_0} \text{ and } \tau_l = \left\{ \frac{a_l}{2\alpha_l} \{2\rho_l + \rho_0\} \right\}^{1/C_l}. \quad (1.9)$$

## 1.5 Application

The IP effect has been successfully in exploration for several decades. The additional information beyond resistivity values from an IP survey can aide in the location of mineralization. The aforementioned interpretation techniques and conductivity models have been used to interpret field data. Three-dimensional forward modeling and inversion continues to improve interpretation and discrimination capabilities of this method.

**Table 1.3.** Descriptive guide for GEMTIP parameters.

Variable	Units	Name	Description
$\rho_{ef}$	Ohm-m	effective resistivity	resulting effective resistivity
$\rho_0$	Ohm-m	matrix resistivity	matrix resistivity of rock being modeled
$f_i$	-	grain volume fraction	volume fraction of each grain type
$m_i$	-	grain chargeability	grain chargeability of each grain type
$\omega$	Hertz	angular frequency	angular frequency of EM signal
$\tau_i$	second	time constant	time constant for each grain
$C_i$	-	decay coefficient	decay coefficient determined from empirical data
$\rho_i$	Ohm-m	grain resistivity	resistivity of each grain type
$a_i$	meter	grain radius	radius of each grain type
$\alpha_i$	$\frac{\text{Ohm}\cdot\text{m}^2}{\text{sec}^{\epsilon_i}}$	surface polarizability coefficient	behavior of charges on grain surface determined from empirical data

### 1.5.1 Data Collection

Induced polarization data are collected using one of the many common resistivity survey electrode configurations with Dipole-Dipole being common. Figure 1.9 shows the current transmitting electrodes and voltage recording receiving electrodes over a polarizable body (target). The recorded data can be either time domain or frequency domain or in some cases both and is commonly presented in pseudosection. An illustration for pseudosection plotting is given in Figure 1.10. An overview of common electrode arrays and their strengths and weaknesses is given in [Sumner, 1976] including sensitivity to EM coupling which can mask the IP response of geologic structures Wynn and Zonge [1975]; Zonge and Wynn [1975]; Pelton et al. [1978].

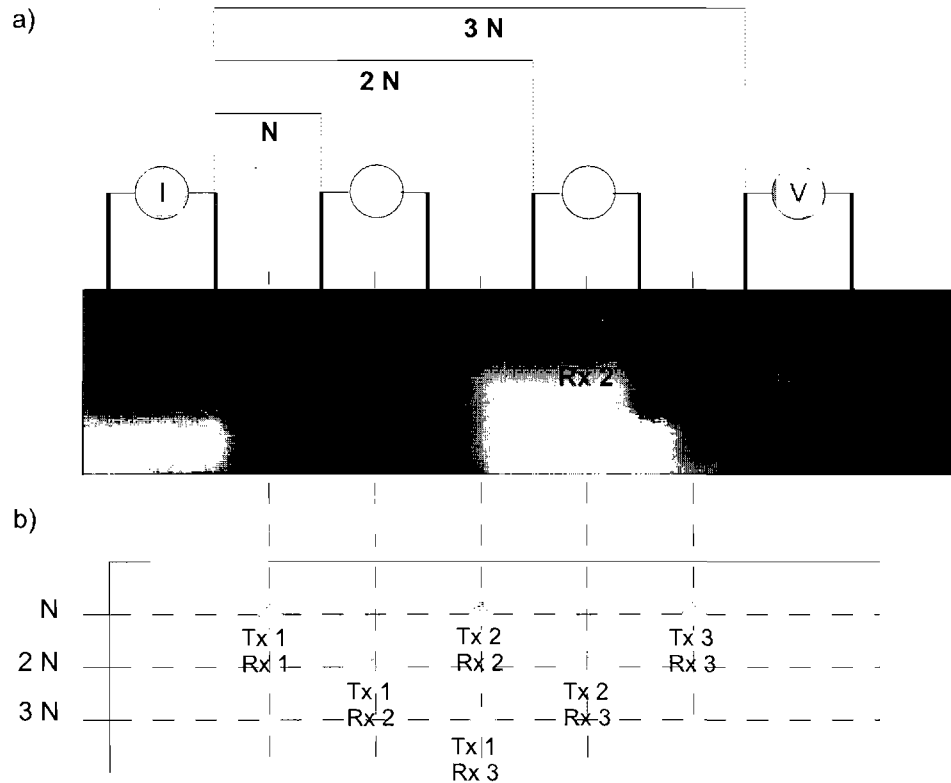


**Figure 1.9.** Illustration of an IP survey using the Dipole-Dipole array with a polarizable body as the target.

### 1.5.2 EM Coupling

EM coupling can be a problem for electrical survey methods [Wynn and Zonge, 1975; Zonge and Wynn, 1975; Pelton *et al.*, 1978] making IP data difficult to interpret. Its effect can be minimized by survey design [Sumner, 1976]. Pelton *et al.* [1978] found that Cole-Cole parameters for EM coupling to be different than those from IP response of mineralization and suggested its removal by a Cole-Cole model. Wynn and Zonge [1975] and Zonge and Wynn [1975] discuss EM coupling removal and interpretation. Additionally, integral equation method 3-D modeling models both EM coupling and the response from geoelectric structures [Hohmann, 1975; Wanamaker *et al.*, 1984; Lou, 1998; Lee and Zhdanov, 2005].

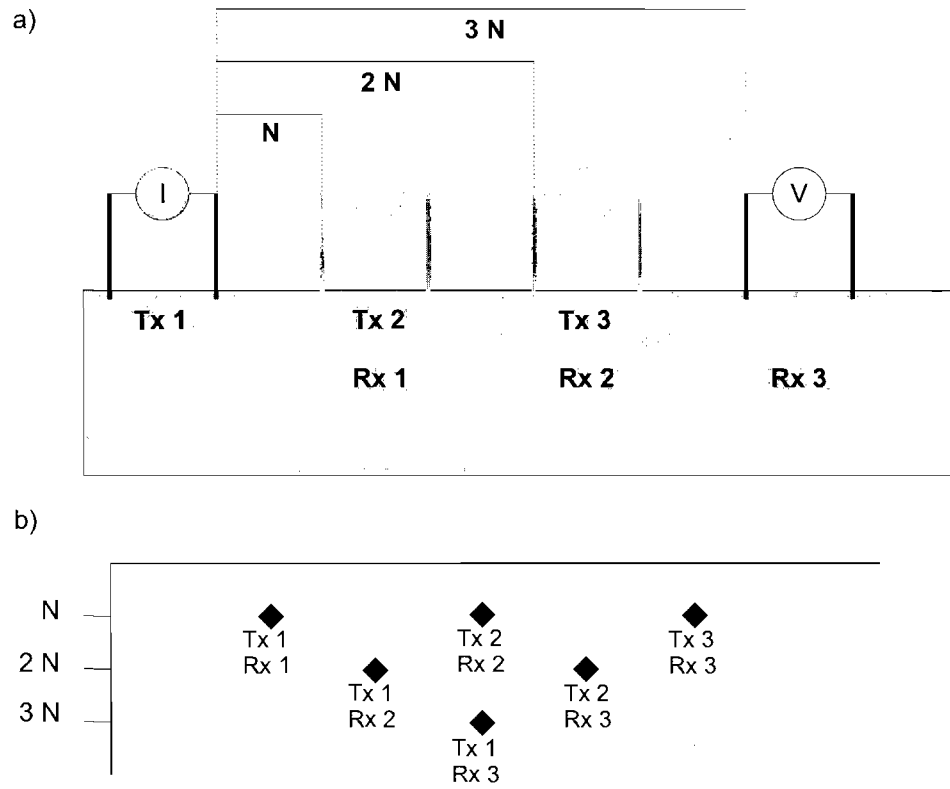


**Figure 1.10.** Dipole-Dipole survey and pseudosection plotting illustration. A pseudosection is created by plotting the computed apparent resistivity and phase as a function of N-spacing and horizontal position. N-spacing refers to the separation of the transmitting dipole and receiving dipole as a multiple of the dipole spacing. Apparent phase the angle formed between the real and imaginary part of the apparent resistivity. a) Transmitting (Tx) and receiving (Rx) electrodes shown. b) Apparent resistivity values computed from transmitter and receiver pairs listed are plotted as a function of N spacing.



### 1.5.3 3-D Modeling and Inversion

Three dimensional electromagnetic modeling is generally accomplished using either a finite element approach or an integral equation (IE) method approach, the latter will be focused on. The integral equation method was pioneered by *Hohmann* [1975] when he modeled 3-D anomalous structure in a uniform halfspace. The 3-D integral equation technique was expanded to include a layered earth background by *Wanamaker et al.* [1984]. Three-dimensional complex resistivity using the Cole-Cole model was modeled by *Lou* [1998]. By incorporating Cole-Cole modeling capability into the Consortium for Electromagnetic Modeling and Inversion EM IE code *Lee and Zhdanov* [2005] laid the ground work for the 3-D modeling using the GEMTIP conductivity model. With the improved forward modeling capabilities successful inversion techniques have been developed [*Cox and Zhdanov*, 2007; *Goold et al.*, 2007; *Yoshioka and Zhdanov*, 2005; *Yoshioka*, 2004; *Li and Oldenburg*, 2000; *Oldenburg and Li*, 1994].

### 1.5.4 Common Applications

IP parameters such as chargeability, phase, FE, PFE metal factor, Cole-Cole parameters, pseudosections, 3-D modeling and inversion have proven useful over the years of successful application of the IP method. Although the IP method has seen the most application in the mining industry it has proven useful for petroleum, hydrologic, and environment applications. Successful applications using both time domain and frequency domain are demonstrated in the following papers: *Seigel et al.* [1997], *Seigel* [1959], *Zonge and Wynn* [1975], *Major and Silic* [1981], *Collett and Katsube* [1973], *Vanhala and Peltoniemi* [1992], *Sumner* [1976], *Arce* [2006]. *Lou* [1998] demonstrates chargeability anomalies associated with petroleum reservoirs. The utility of the IP method for hydrology applications is given by *Slater* [2006]. Environmental applications of complex resistivity are given by *Olhoeft* [1985].

## 1.6 Summary

The recorded IP effect, caused by surface polarizability effects, in collected EM data provides additional information to the geoscientist. Many conductivity models seek to describe the phenomenon, with the newest, GEMTIP, incorporating many geoelectric parameters. This new model is tested and applied in the following chapters. In addition to the standard pseudosection presentation of resistivity, phase, chargeability and other IP data, 3-D modeling and inversion have been developed. These techniques seek to utilize the IP phenomenon to learn more about the subsurface geology. The IP effect and its modeling and application is a complex subject and cannot be fully addressed in this introduction. I suggest the excellent overviews by *Wait* [1959], *Sumner* [1976], *Lou* [1998], and *Reynolds* [1998] for further reading.

## CHAPTER 2

# TESTING THE GENERALIZED EFFECTIVE MEDIUM THEORY OF INDUCED POLARIZATION WITH PORPHYRY ANALOGS

### 2.1 Introduction

Studying the frequency dependent complex resistivity resulting from the induced polarization (IP) effect is important problem for electromagnetic (EM) geophysics. The Generalized Effective Medium Theory of IP (GEMTIP) [Zhdanov, 2006] seeks to describe the IP effect from rock composition at the grain scale and increase our understanding of the IP effect with the goal of mineral discrimination.

The IP effect has been successfully applied and studied for over 50 years. Several conductivity relaxation models have previously been developed including the empirical Cole-Cole model [Cole and Cole, 1941; Pelton *et al.*, 1978] and electrochemical models developed by Ostrander and Zonge [Ostrander and Zonge, 1978] and the Wong models [Wong, 1979; Wong and Strangway, 1981].

The widely accepted Cole-Cole model uses only bulk rock variables and does not address rock composition. The Wong models, although more comprehensive, have not been widely adapted.

The newly developed GEMTIP conductivity model by [Zhdanov, 2006] seeks to describe observed complex resistivity using rock composition. This new formulation models the multifrequency behavior of rocks using geoelectric parameters for each phase of the media.

In this research project, the complex resistivity data are collected for 16 rock samples to test the spherical grain analytic solution of GEMTIP formulated by *Zhdanov* [2006]. The synthetic rocks from the [*Ostrander and Zonge, 1978*] study are modeled and compared to their published data. An inversion routine to recover the surface polarizability coefficient and the decay coefficient is developed and tested using synthetic data. A detailed mineralogical analysis using optical methods and X-ray tomography is conducted for three of the 16 rock samples. Using the mineralogical information as GEMTIP variables for the inversion, the surface polarizability coefficient ( $\alpha$ ) and the decay coefficient ( $C$ ) are recovered from the measured EM data.

## 2.2 GEMTIP Overview

The Generalized Effective Medium Theory of Induced Polarization (GEMTIP) allows the complex (real and imaginary) spectral behavior of rock conductivity to be predicted based on the grain-scale composition and physical properties. GEMTIP is based on the effective-medium theory, which provides a unified mathematical method to study heterogeneity, multiphase structure, and polarizability of rocks. The geoelectrical parameters of a new conductivity model are determined by the petrophysical properties of the rock including: mineralization type and/or fluid content, mineralization volume fraction and/or porosity, mineral geometry and/or pore size, matrix composition, anisotropy, and the polarizability of formations. The spherical case of GEMTIP gives effective resistivity ( $\rho_{ef}$ ) as:

$$\rho_{ef} = \rho_0 \left\{ 1 + \sum_{i=1}^N \left\{ f_i m_i \left\{ 1 - \frac{1}{1 + \{-i\omega\tau_i\}^{C_i}} \right\} \right\} \right\}^{-1}, \quad (2.1)$$

where:

$$m_i = 3 \frac{\rho_0 - \rho_i}{2\rho_i + \rho_0} \text{ and } \tau_i = \left\{ \frac{a_i}{2\alpha_i} \{2\rho_i + \rho_0\} \right\}^{1/C_i}. \quad (2.2)$$

Disseminated sulfides have been chosen as the closest analog to the spherical case of GEMTIP. Figure 2.1 shows idealized multiphase disseminated mineralization for which Equation 2.1 predicts complex effective resistivity. Table 2.1 provides a full explanation of each variable in Equation 2.1.

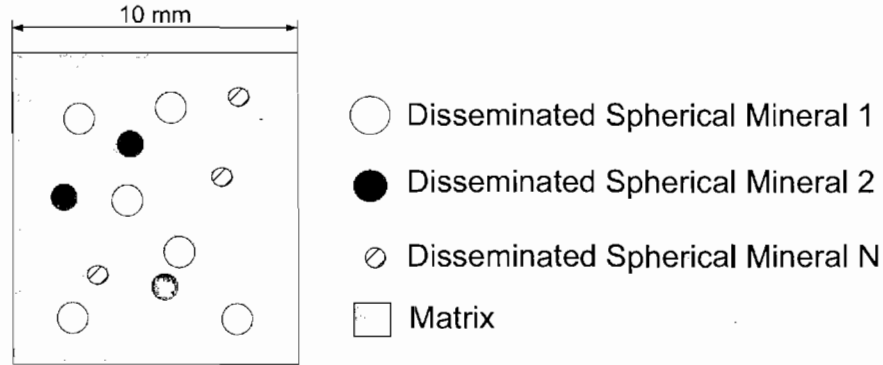


**Figure 2.1.** Conceptual illustration of disseminated mineralization. The figure illustrates the basic geometrical input parameters for modeling with the spherical case of GEMTIP, including mineral size, mineral types, and mineral volume fractions. The complete list of GEMTIP variables is given in Table 2.1.

**Table 2.1.** Descriptive guide for GEMTIP parameter.

Variable	Units	Name	Description
$\rho_{ef}$	Ohm-m	effective resistivity	resulting effective resistivity
$\rho_0$	Ohm-m	matrix resistivity	matrix resistivity of rock being modeled
$f_l$	-	grain volume fraction	volume fraction of each grain type
$m_l$	-	grain chargeability	grain chargeability of each grain type
$\omega$	Hertz	angular frequency	angular frequency of EM signal
$\tau_l$	second	time constant	time constant for each grain
$C_l$	-	decay coefficient	decay coefficient determined from empirical data
$\rho_l$	Ohm-m	grain resistivity	resistivity of each grain type
$a_l$	meter	grain radius	radius of each grain type
$\alpha_l$	$\frac{\text{Ohm}\cdot\text{m}^2}{\text{sec}^{\epsilon_l}}$	surface polarizability coefficient	behavior of charges on grain surface determined from empirical data

Figure 2.2 illustrates the application of GEMTIP by correlating variables with a polished sample of a quartz monzonite containing disseminated sulfides. In Figure 2.2 the pyrite phase is modeled and the chalcopyrite phase would be modeled by adding another term to the summation and using  $\rho_2$ ,  $a_2$ ,  $\alpha_2$ , etc. The inclusion of matrix resistivity, mineral grain size, mineral resistivity, mineral volume fraction, the decay coefficient, and the surface polarizability coefficient make GEMTIP a comprehensive conductivity model.

### 2.3 Comparison to 1978 Ostrander and Zonge Data

The first test of the spherical case of GEMTIP was to compare it to published data. *Ostrander and Zonge* [1978] studied synthetic rocks containing disseminated chalcopyrite and/or pyrite. Synthetic rocks bearing either pyrite and/or chalcopyrite at specific grain sizes were constructed using a matrix of known resistivity.

$$\rho_{ef} = \rho_0 \left\{ 1 + \sum_{l=1}^N \left\{ f_l m_l \left\{ 1 - \frac{1}{1 + \{-i\omega\tau_l\}^{C_l}} \right\} \right\} \right\}^{-1}$$

$$m_l = 3 \frac{\rho_0 - \rho_l}{2\rho_l + \rho_0} \text{ and } \tau_l = \left\{ \frac{a_l}{2\alpha_l} \{2\rho_l + \rho_0\} \right\}^{1/C_l}$$

**Figure 2.2.** Illustration of equation parameters and their relationship to a rock sample SB03 with disseminated pyrite and chalcopyrite mineralization. The figure illustrates the input parameters for the pyrite phase. The chalcopyrite would be modeled by adding an additional ( $l = 2$ ) term to the summation. GEMTIP variables are described in Table 2.1.

Complex resistivity measurements were made for each synthetic rock. *Ostrander and Zonge* [1978] plotted the peak IP response frequency as a function of grain size for synthetic rocks containing either pyrite or chalcopyrite. Figure 2.3 plots the modeled complex resistivity curves of a rock containing disseminated pyrite at different radii. The modeled complex resistivity curves for a rock containing disseminated chalcopyrite at different radii are shown in Figure 2.4. The peak IP response occurs at higher frequency as grain radii decreases for both pyrite and chalcopyrite containing rocks. The GEMTIP modeled data and the *Ostrander and Zonge* [1978] empirical data are plotted in Figure 2.5. The GEMTIP modeled data yields the same trend of peak IP response frequency as the empirical results with respect to grain size. Table 2.2 presents the GEMTIP variables used and the known parameters from Ostrander and Zonge. The empirical parameters  $\alpha$  and  $C$  are held constant for each mineral. These parameters were adjusted for each mineral until a good fit to the empirical data was established. The exact volume fraction of chalcopyrite and pyrite used by Ostrander and Zonge for each sample is unknown. Figure 2.6 demonstrates that variations in volume fraction do not cause a large change in the peak IP frequency, indicating the comparison to be accurate as long as the volume fraction for each grain size distribution sample was kept between 5 % and 30 % sulfides.

*Schwartz* [1962] proposed  $\tau$  is related to grain size and observed peak IP frequency to be related to  $\frac{1}{\text{radius}^2}$ . Grain size is included in the models proposed by *Wong* [1979] and *Wong and Strangway* [1981]. *Mahan et al.* [1986] observed peak IP frequency to vary as  $\frac{1}{\text{radius}^2}$  for smaller grains and  $\frac{1}{\text{radius}}$  for larger grains. GEMTIP can model the IP effect of grain size.

## 2.4 Alpha and C Inversion on Synthetic Data

An inversion routine to obtain the two empirical parameters in of the GEMTIP conductivity model (Equation 2.1), the surface polarizability coefficient(s) ( $\alpha$ ) and the decay coefficient(s) ( $C$ ) was formulated. The inversion uses the Regularized

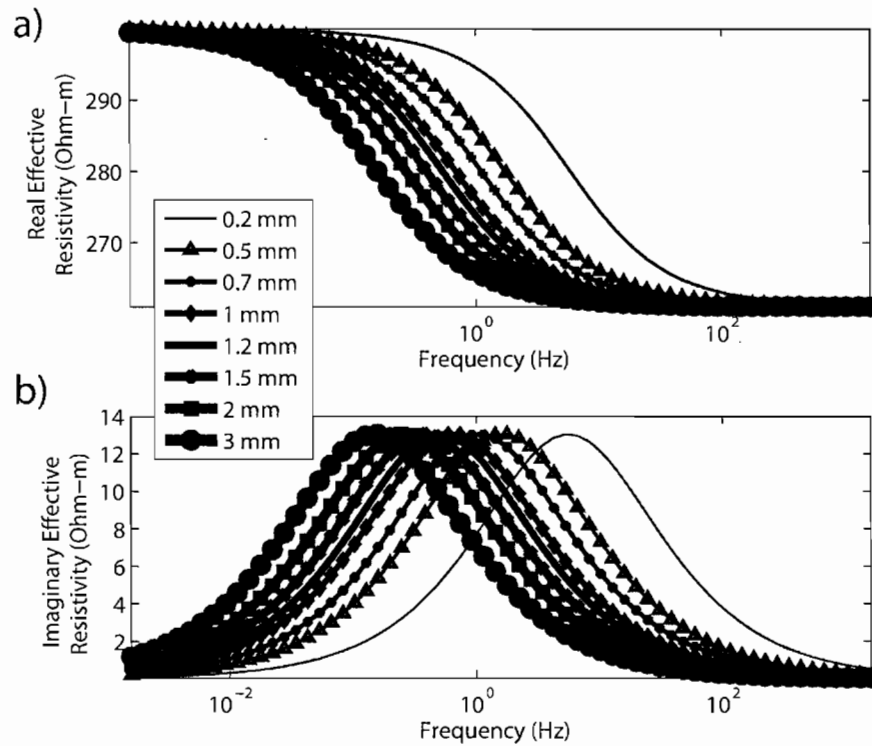


**Figure 2.3.** GEMTIP models of *Ostrander and Zonge* [1978] synthetic rocks containing pyrite. The location of the maximum imaginary resistivity is the frequency of the maximum IP response. Notice how the frequency of the maximum IP response increases with a decrease in grain size. See Table 2.2 for the GEMTIP variables used.

Newton approach described in *Zhdanov* [2002]. Three related algorithms were developed using this approach:

1. Two-phase inversion: This routine solves for one disseminated phase that occurs at one grain size.
2. N-phase inversion: This routine solves for N disseminated phases with one grain size per phase. A rock containing two or more disseminated minerals would require this approach.



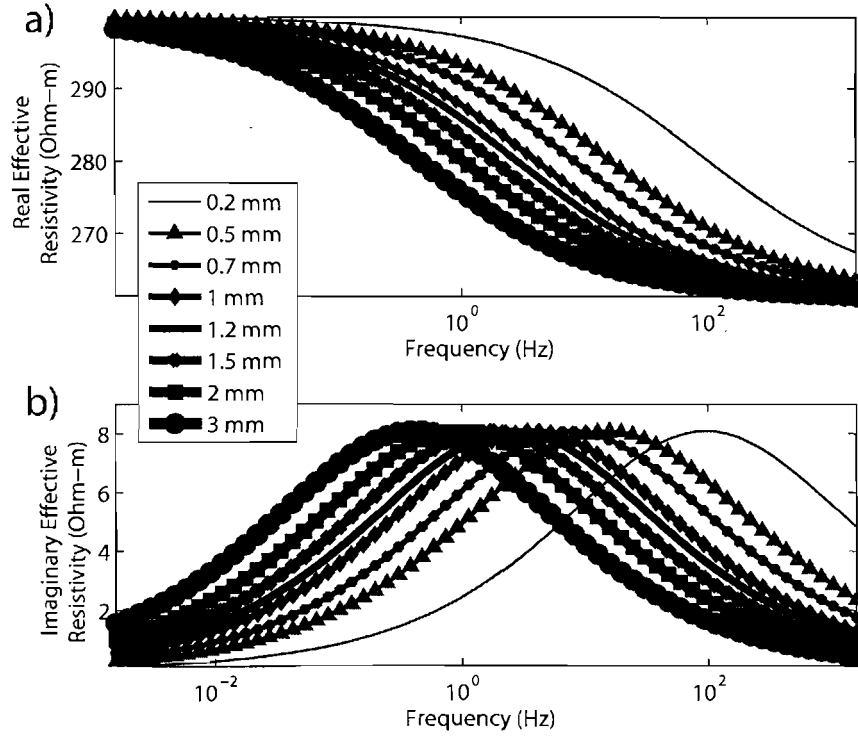


**Figure 2.4.** GEMTIP models of *Ostrander and Zonge* [1978] synthetic rocks containing chalcopyrite. For a given grain size, the frequency of the maximum IP effect is higher for chalcopyrite as compared to pyrite by choosing a larger  $\alpha$  for chalcopyrite. Table 2.2 lists the GEMTIP variables used.

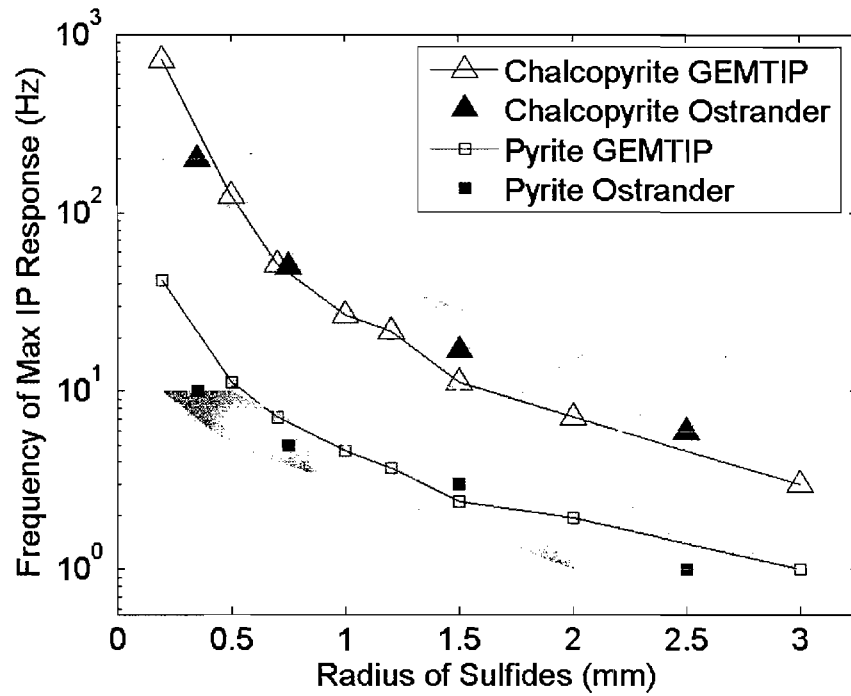
3. Two-phase inversion for  $N$  grain sizes: This routine solves for one  $\alpha$  and one  $C$  for  $N$  disseminated grain sizes. A rock containing one disseminated mineral at multiple grain sizes would require this algorithm.

Figure 2.7 illustrates each inversion routine developed. The inversion algorithm used to minimize the misfit is given by:

$$r_n = A(m_n) - d \quad (2.3)$$

$$\delta m_n = H^{-1} F^* r_n \quad (2.4)$$

$$m_{n+1} = m_n + \delta m_n, \quad (2.5)$$



**Figure 2.5.** Fit of GEMTIP predicted data with empirical measurements of *Ostrander and Zonge* [1978] rock-scale Induced Polarization study. The good fit of the GEMTIP modeled data with the empirical data indicates GEMTIP can accurately model the trend in peak IP response as a function of grain size. The gray shading indicates the range of grain sizes for each measurement of maximum IP response. For example the pyrite synthetic rock plotted at 2.5 mm contains pyrite grains from 2 mm to 3 mm. Refer to Table 2.2 for the GEMTIP variables used.

where

$$A = \text{GEMTIP}(\rho_{ef})$$

$$m = [\alpha \ C]$$

$$d = \text{EM measurements}$$

$$F = \left[ \frac{d\rho_{ef}}{d\alpha} \quad \frac{d\rho_{ef}}{dC} \right]$$

$$H = [FF^* + RI]$$

$$R = \text{regularization parameter}$$

$$\text{misfit} = |A(m_n) - d|^2.$$

The Frechet ( $F$ ) derivative for the developed algorithm is a matrix formed by the partial derivative with respect to  $\alpha$  and the partial derivative with respect to  $C$ . For

**Table 2.2.** Comparison of GEMTIP parameters for CEMI and *Ostrander and Zonge* [1978]

Variable	Units	CEMI	Ostrander and Zonge
$\rho_{ef}$	Ohm-m	-	300 +- 75
$\rho_{matrix}$	Ohm-m	300	-
$f_{chalcopryrite}$	%	15	-
$f_{pyrite}$	15	-	-
$C_{chalcopryrite}$	-	0.6	-
$C_{pyrite}$	-	0.8	-
$\rho_{chalcopryrite}$	Ohm-m	0.004 <sup>a</sup>	-
$\rho_{pyrite}$	Ohm-m	0.3 <sup>a</sup>	-
$a_{chalcopryrite}$	mm	0.2, 0.5, 0.7, 1, 1.2, 1.5, 2, 3	0.2-0.5, 0.5-1, 1-2, 2-3
$a_{pyrite}$	mm	0.2, 0.5, 0.7, 1, 1.2, 1.5, 2, 3	0.2-0.5, 0.5-1, 1-2, 2-3
$\alpha_{chalcopryrite}$	$\frac{\text{Ohm}\cdot\text{m}^2}{\text{sec}^{\alpha}}$	4	-
$\alpha_{pyrite}$	$\frac{\text{Ohm}\cdot\text{m}^2}{\text{sec}^{\alpha}}$	2	-

<sup>a</sup> *Nabighian* [1988]

the two-phase inversion, both the analytic and brute force Frechets were developed. Testing indicated similar performance of the analytic and brute force Frechets; therefore the easier to implement brute force Frechet was used for the other three inversions. Generally, this problem is overdetermined, except when disseminated mineral phases outnumber recorded frequencies. The two-phase inversion is stable and usually unique; see results in Figures 2.8, Table 2.3 and Figure 2.9. N-phase inversion results are generally good but certain parameter combinations produce a  $\rho_{ef}$  curve that has multiple solutions. Figure 2.10 shows good model parameter convergence from the  $\rho_{ef}$  data in Figure 2.11 produced by the parameters given in Table 2.4. In contrast Figure 2.12 shows poor convergence from the the inputs listed in Table 2.5 and corresponding data in Figure 2.13. The results from testing the two-phase inversion for N grain sizes are presented in Figures 2.14 and 2.15. Table 2.6 shows the good recovery of  $\alpha$  and  $C$ . A family of successful GEMTIP inversion routines were developed for application to measured EM data.

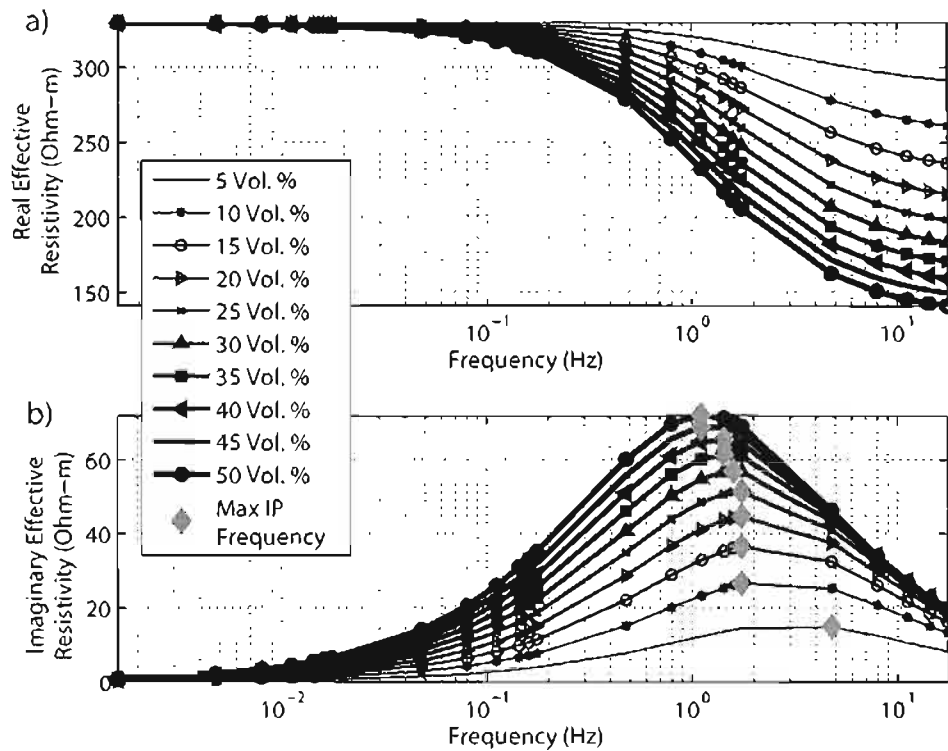


Figure 2.6. The small effect of volume fraction on maximum IP frequency is shown in the graphed data are for 1 mm pyrite grains. Table 2.2 shows the variables used.

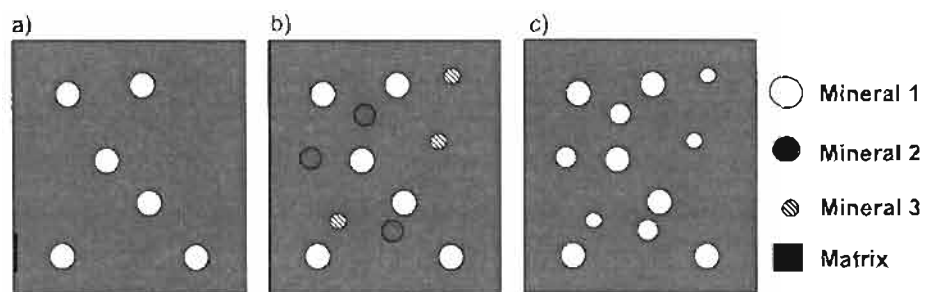


Figure 2.7. Illustrations of the three developed inversion routines. a) Two-phase, matrix and one disseminated phase. b) N-phase, matrix with N disseminated phases. c) Two-phase N grain sizes, one disseminated phase with N grain sizes.

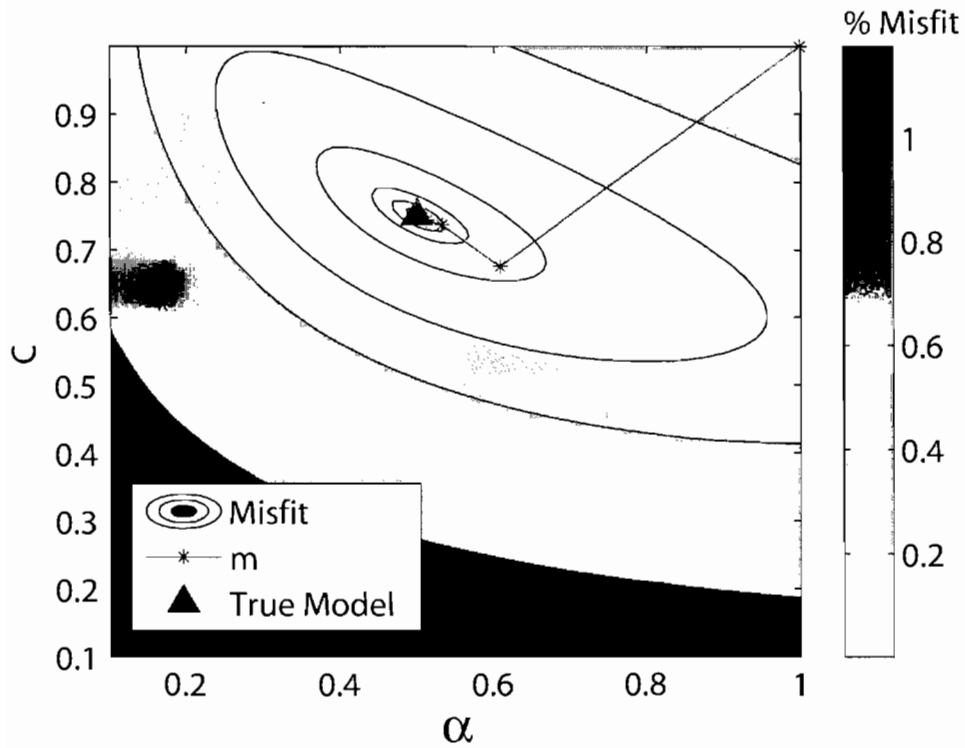
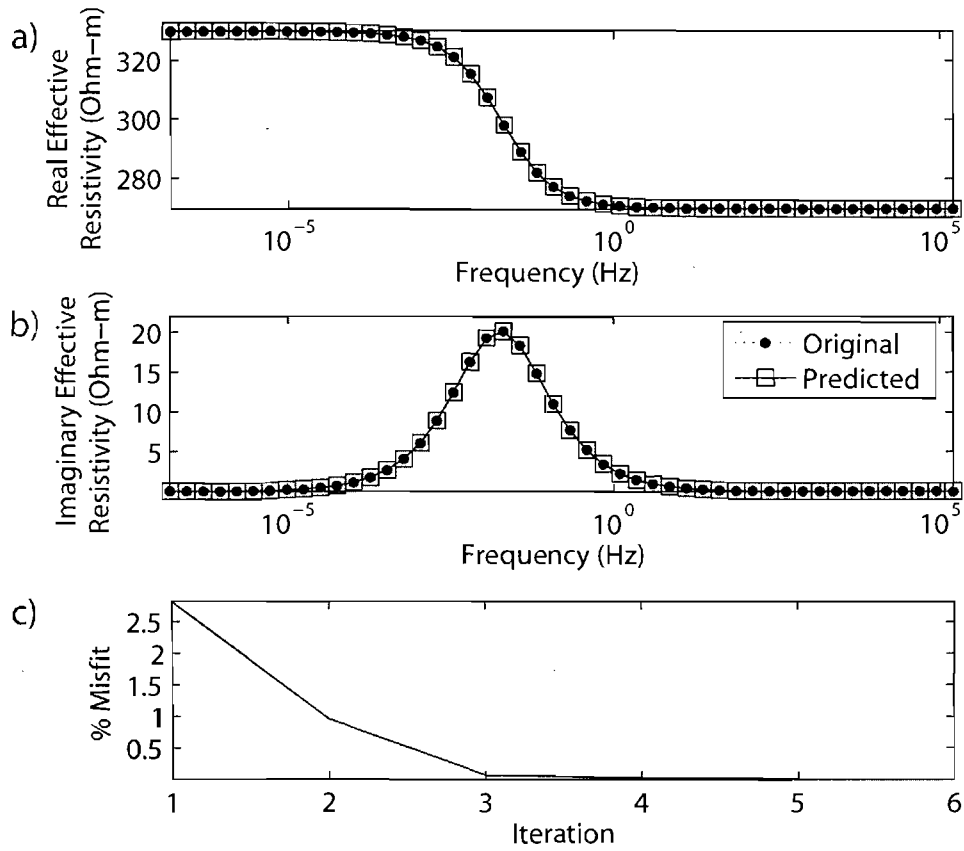


Figure 2.8. Misfit plot for two-phase inversion of synthetic data.

Table 2.3. Two-phase inversion GEMTIP variables.

Variable	Units	Original	Recovered
$\rho_{matrix}$	Ohm-m	330	-
$f$	7.5	-	-
$C$	-	0.75	0.75
$\rho_{phase1}$	Ohm-m	0.3	-
$a$	mm	12.5	-
$\alpha$	$\frac{\text{Ohm}\cdot\text{m}^2}{\text{sec}^2}$	0.5	0.5
$R$	-	-	2000



**Figure 2.9.** Data fit for two-phase inversion of synthetic data. a) Real effective resistivity, b) Imaginary effective resistivity, c) Misfit vs. iteration.

**Table 2.4.** Four-phase media inversion GEMTIP variables that produce good convergence.

Variable	Units	Original	Recovered
$\rho_{matrix}$	Ohm-m	330	-
$f$	%	5 7 2	-
$C$	-	0.5 0.75 0.8	0.5 0.75 0.8 <sup>a</sup>
$\rho$	Ohm-m	0.004 0.3 0.1	-
$a$	mm	0.1 1 10	-
$\alpha$	$\frac{\text{Ohm}\cdot\text{m}^2}{\text{sec}^2}$	0.9 0.25 0.1	0.9 0.25 0.1 <sup>a</sup>
$R$	-	-	2000

<sup>a</sup>Imaginary part less than 1%.

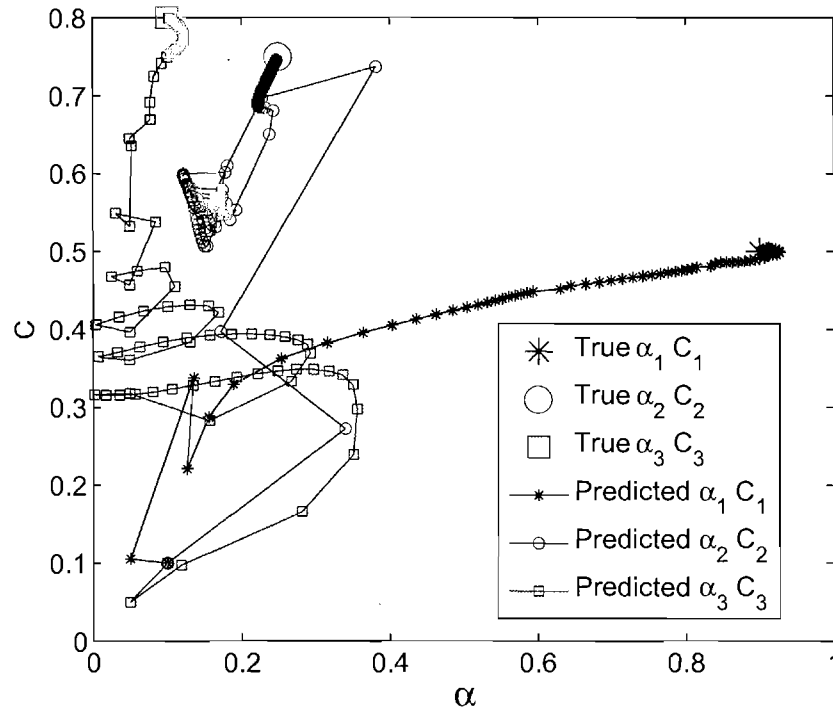


**Figure 2.10.** Convergence plot for a simulated four-phase media (three disseminated phases) where model parameters produce good convergence. The values of  $\alpha$  and  $C$  are recovered.

**Table 2.5.** Four-phase media inversion GEMTIP variables that produce poor convergence.

Variable	Units	Original	Recovered
$\rho_{matrix}$	Ohm-m	330	-
$f$	%	5 7 2	-
$C$	-	0.5 0.75 0.8	0.5+0.008i 0.58+0.016i 0.44+0.01i
$\rho$	Ohm-m	0.004 0.3 0.1	-
$a$	mm	0.1 1 10	-
$\alpha$	$\frac{\text{Ohm}\cdot\text{m}^2}{\text{sec}^2}$	0.9 0.1 0.5	0.86+0.05i 0.08+0.07i 0.67+0.73i
$R$	-	-	2000

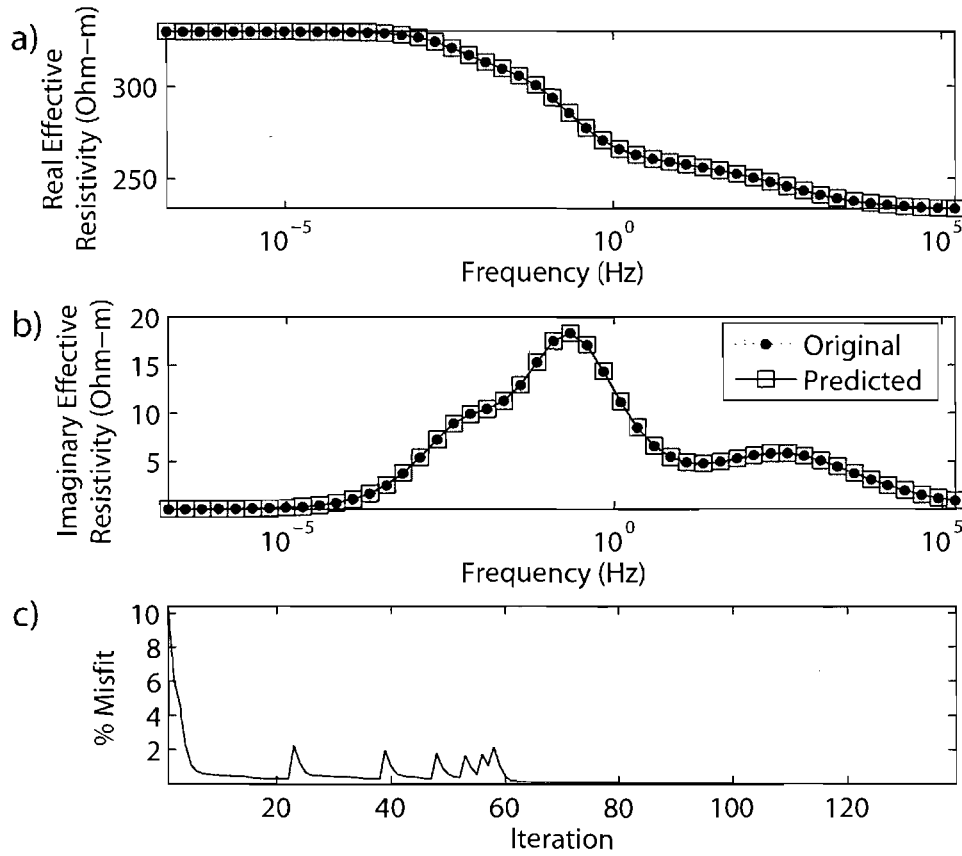


**Figure 2.11.** Data fit for a four-phase media inversion where model parameters produce good convergence. a) Real effective resistivity, b) Imaginary effective resistivity, c) Misfit vs. iteration.

**Table 2.6.** Two-phase N grain sizes inversion GEMTIP variables.

Variable	Units	Original	Recovered
$\rho_{matrix}$	Ohm-m	330	-
$f$	%	1000 random numbers of order $10^{-2}$	-
$C$	-	0.75	0.75
$\rho$	Ohm-m	0.3	-
$a$	mm	1000 random numbers of order $10^0$	-
$\alpha$	$\frac{\text{Ohm}\cdot\text{m}^2}{\text{sec}^{\epsilon t}}$	0.5	0.5
$R$	-	-	1000



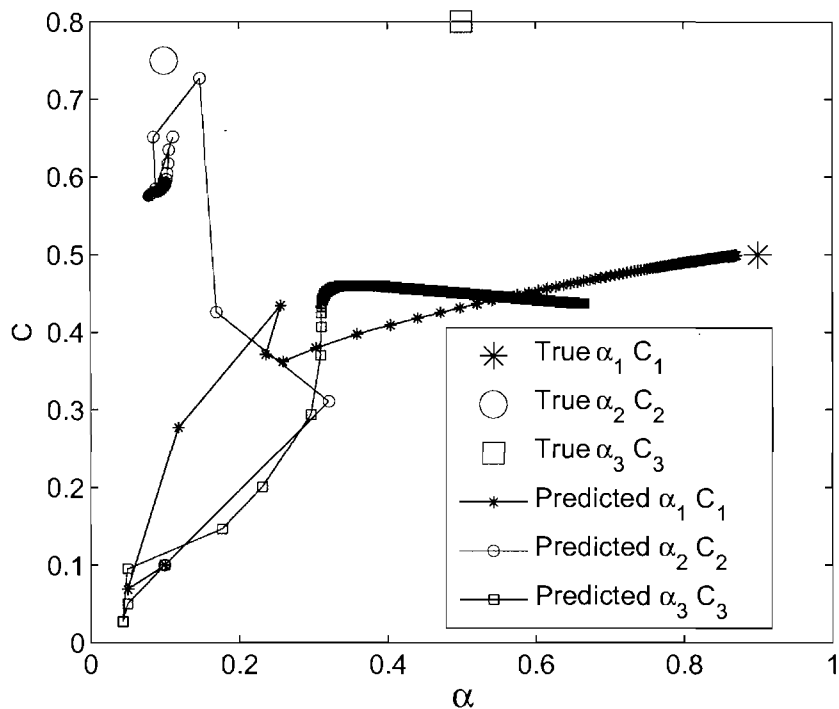


**Figure 2.12.** Convergence plot a for four-phase media inversion where model parameters produce poor convergence. The values of  $\alpha$  and  $C$  are poorly recovered due to the nonunique nature of the solution. Comparing the three unique peaks of Figure 2.11 to the two unique peaks for three model parameters of Figure 2.13 it is evident the solution is nonunique.

## 2.5 Geologic Analog and Samples Chosen for Analysis

Three rocks containing disseminated sulfide mineralization were chosen for analysis as the best analog to the spherical case of GEMTIP. The predominant large discrete pyrite grains, relatively homogeneous matrix, and good EM response made sample K01 the first choice for detailed analysis. Sample K01 is a monzonite from the Kori Kollo mine in Bolivia with disseminated pyrite and a predominantly sericite and quartz matrix (Figure 2.16). Pyrite grains in sample K01 are a few millimeters in diameter. To test GEMTIP on fine dissemination, sample M02 was chosen. Figure 2.17 shows the submillimeter pyrite grains in sample M02 from Milford, Utah. To analyze a three-phase media sample SB03 was chosen from Silver Bell

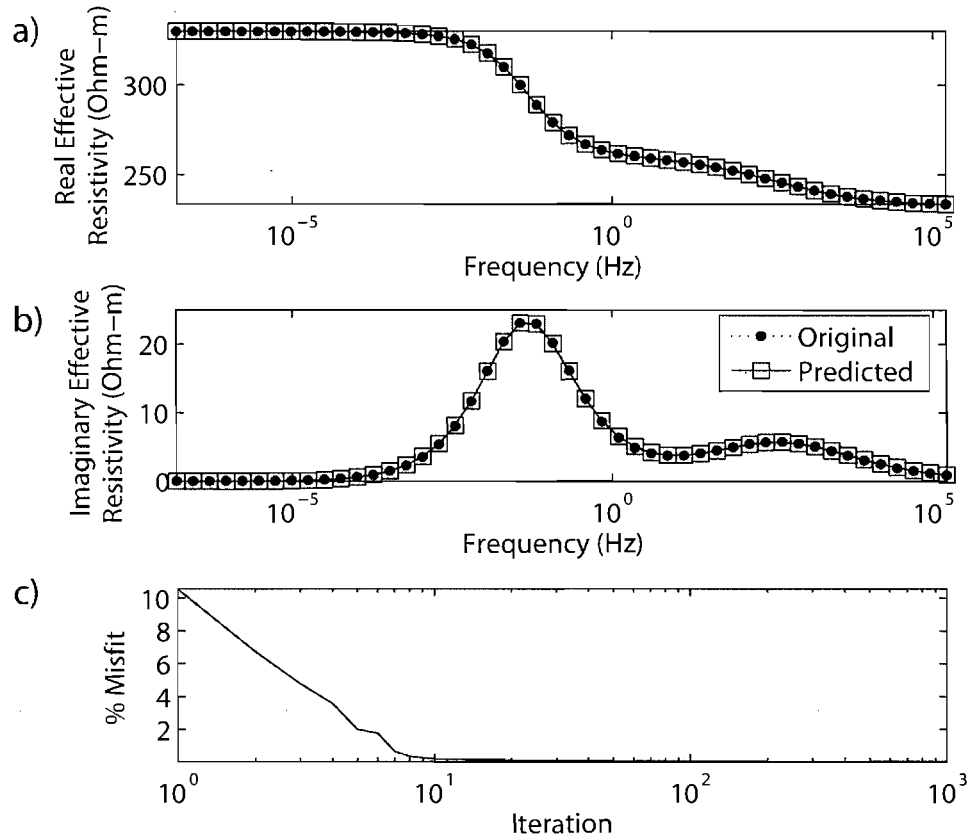


**Figure 2.13.** Data fit for a four-phase media inversion where model parameters produce poor convergence. a) Real effective resistivity, b) Imaginary effective resistivity, c) Misfit vs. iteration.

mine, Arizona. Disseminated chalcopyrite and pyrite can be seen in the photograph of sample SB03 (Figure 2.18). A detailed mineralogical description of each sample is presented in Table 2.7.

## 2.6 X-ray Microtomography

For a better understanding of the 3-D structure and composition of each sample, X-ray microtomography data were acquired. The X-ray microtomography machine creates a 3-D volume of attenuation coefficients stored as voxels (3-D pixels). These attenuation coefficients can be used to determine rock composition. For the application of this study the attenuation coefficients are used to distinguish

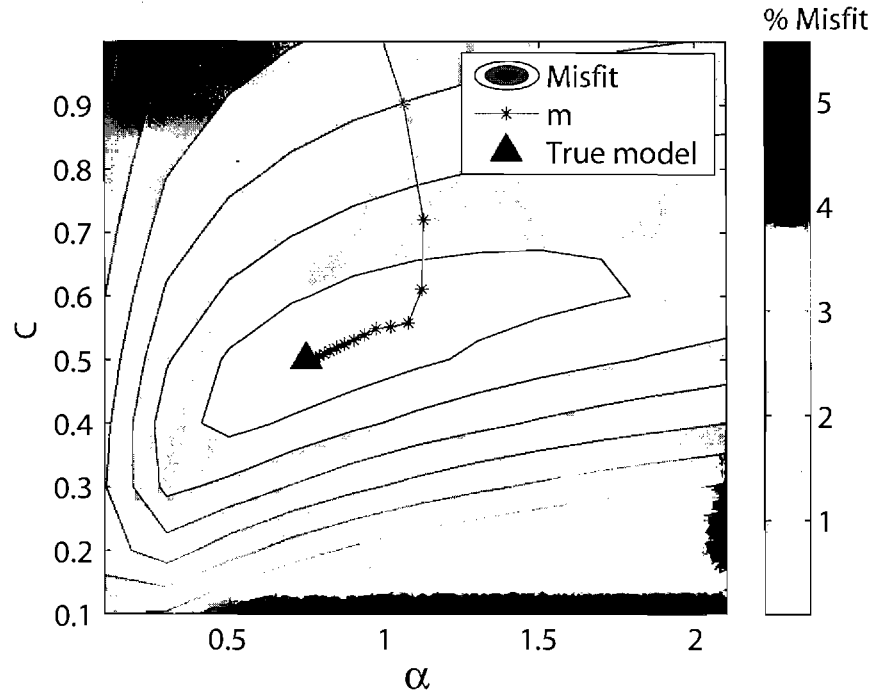


**Figure 2.14.** Misfit plot for two-phase N grain size inversion

sulfides from the matrix. The smallest voxel size the machine is capable of is  $5\mu\text{m}$  for a 1 cm sample [Miller and Lin, 2004]. Samples can be as large as 40 mm and have densities up to  $8\text{g/cc}$  [Miller and Lin, 2004]. For this study one to three 7 mm diameter cores drilled from the samples used for EM measurements were analyzed with a  $20\mu\text{m}$  voxel size for K01, M02, and SB03. For each sample a 3-D image was produced, highlighting the sulfide phases (Figures 2.19, 2.20, and 2.21). Qualitative analysis was conducted by viewing the 3-D images and approximating grain radii. In addition to the 3-D image, the volume fraction, grain size, and surface area can be determined by X-ray microtomography. The data acquisition software's automatic grain-picking routine creates a table of individual grains and their geometric properties. Grain radii are calculated from the grain volumes using an approximation assuming spherical grains given by:

$$radius_{grain\ n} = \left\{ voxels_{grain\ n} \frac{3}{4\pi} \left\{ 20 \frac{\mu\text{m}}{\text{voxel}} \right\}^3 \right\}^{1/3}. \quad (2.6)$$

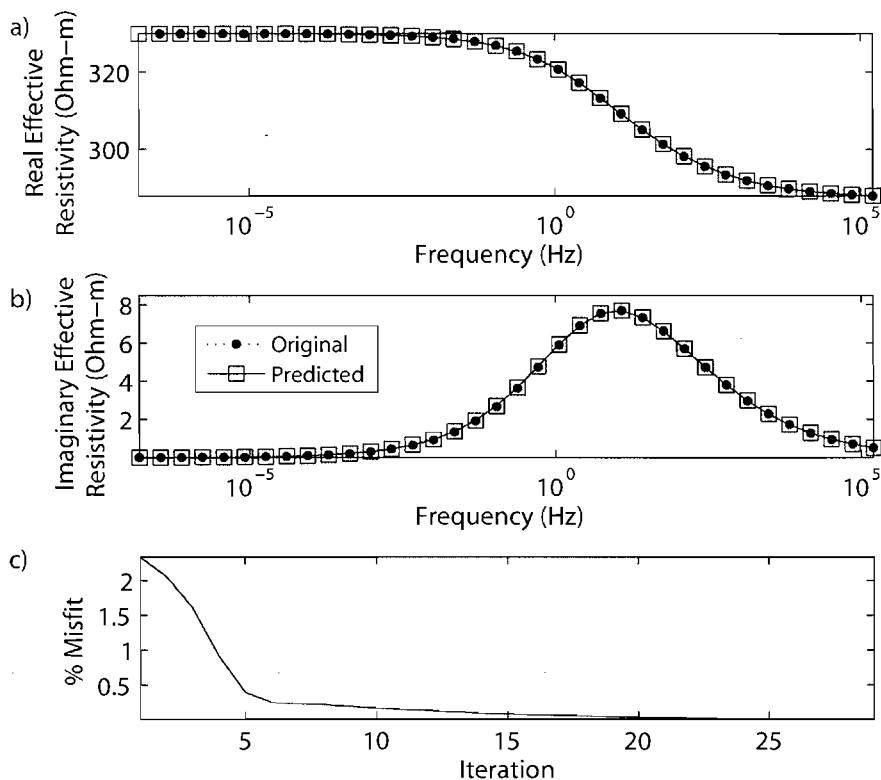


**Figure 2.15.** Data fit for Two-phase N grain sizes inversion. a) Real effective resistivity, b) Imaginary effective resistivity, c) Misfit vs. iteration.

A second program, based on marching cubes [Lorenson and Cline, 1987], determines the surface area of the disseminated minerals by using a mesh fitting algorithm. Additionally, individual grains are separated into polygon files for viewing and analysis. Select polygon files were analyzed to determine maximum grain dimension, surface area, and volume. Table 2.7 outlines the detailed quantitative and qualitative information gained from the X-ray microtomography data. Sample size in combination with the number of samples used in the X-ray tomography accounted for only a small fraction of the EM sample volume. Digital X-ray tomography data are included in Appendix B. X-ray microtomography provided important quantitative and qualitative information for modeling using GEMTIP.

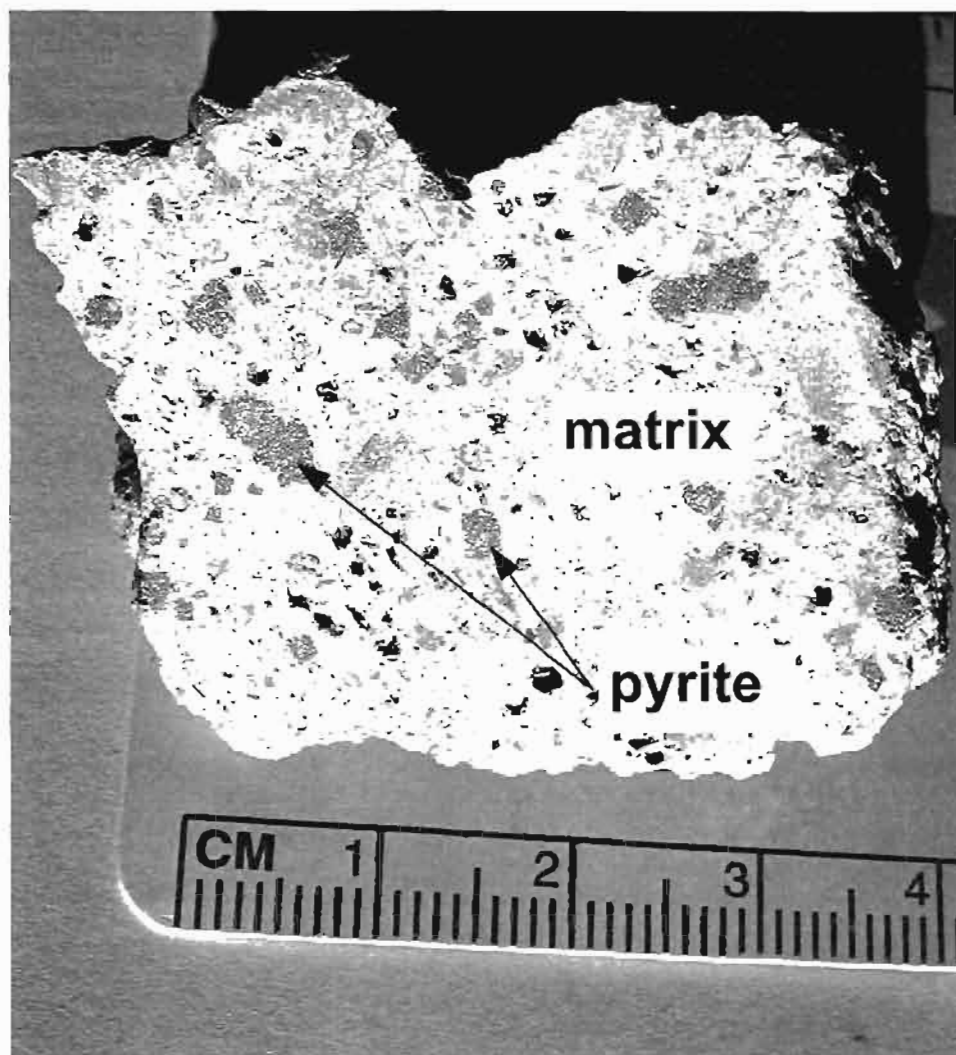


Figure 2.16. Sample K01, Korri Kollo, Bolivia, pyrite in a predominately sericite matrix.

**Table 2.7.** Sample mineralogical assessment summary.

Method	Matrix Composition	Pyrite Volume Fraction	Pyrite Radius	Chalcoyrite Volume Fraction	Chalcoyrite Radius
<b>Sample K01</b>					
Optical	sericite, quartz	10%	between 1 and 2.5 mm	-	-
X-ray Tomography Quantitative	-	7% <sup>a</sup>	478 grains with 90% of the cumulative grain volume from 15 grains of 0.5 to 1.3 mm and 50% from two grains of 1.1 and 1.3 mm <sup>b</sup>	-	-
X-ray Tomography Qualitative	-	-	predominantly 1 to 2 mm with smaller grains	-	-
<b>Sample M02</b>					
Optical	quartz	1%	0.03 to 0.1 mm	-	-
X-ray Tomography Quantitative	-	2%	20979 grains with 90% of the cumulative grain volume from 4000 grains of 0.05 to 0.7 mm	-	-
X-ray Tomography Qualitative	-	-	predominantly 1 mm with smaller grains	-	-
<b>Sample SB03</b>					
Optical	sericite, quartz	5%	0.05 to 1 mm	2%	0.05 to 0.5 mm
X-ray Tomography Quantitative	-	0.95%	1526 grains with 90% of the cumulative grain volume from 50 grains of 0.15 to 1 mm	0.02%	455 grains with 90% of the cumulative grain volume from 46 grains of 0.04 to 0.2 mm
X-ray Tomography Qualitative	-	-	0.05 to 1 mm	-	0.075 mm

<sup>a</sup>Found by dividing the total number of voxels associated with the mineral by the total number of voxels making the core.

<sup>b</sup>Approximation using Equation 2.6 for each grain identified by the automatic detection algorithm.

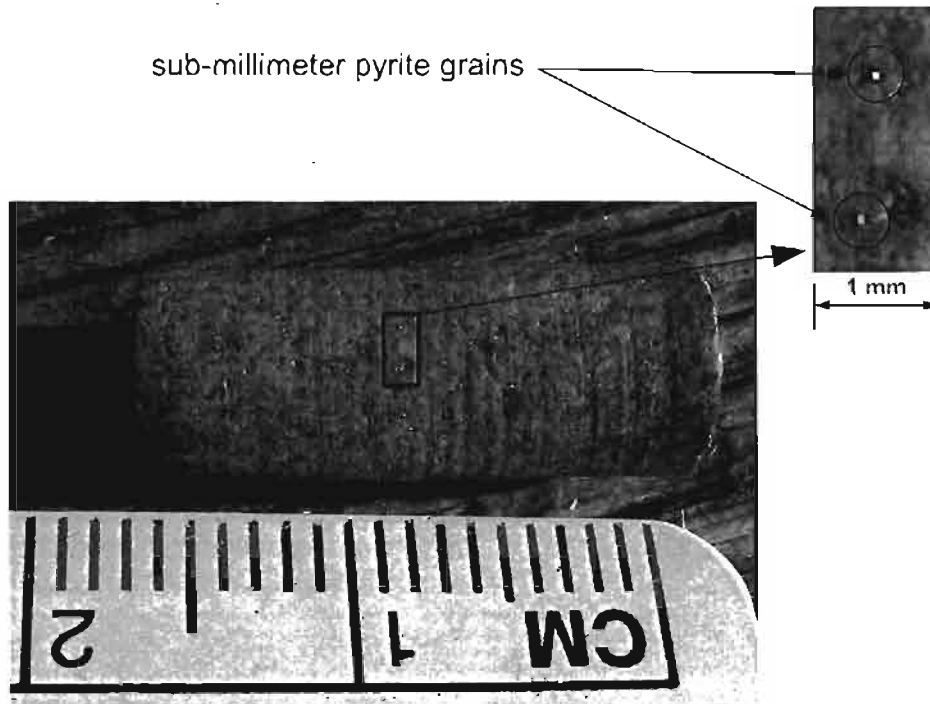


Figure 2.17. Sample M02, Milford, Utah, pyrite in feldspar and quartz matrix.

## 2.7 EM Measurements

The viability of the new GEMTIP conductivity model was tested with multi frequency EM measurements acquired for 16 rock samples at Zonge Engineering and Research Organization Inc, Tuscon, Arizona. Photographs of the measurement system are shown in Figures 2.22 and 2.23. Frequency domain data were recorded for 36 frequencies from 0.0156 Hz to 9216 Hz. A DC measurements and time domain data were collected. The DC measurement was used to establish matrix resistivity. The time domain data were not analyzed for this study. Density and porosity measurements were also acquired. From the frequency domain data, real and imaginary apparent resistivity were calculated. The calculated apparent resistivity is analogous to the predicted effective resistivity of the GEMTIP conductivity model. Recorded apparent resistivity for samples K01, M02, and SB03 are presented in Figure 2.24 and their data are in Appendix A. Both *Pelton et al.* [1978] and

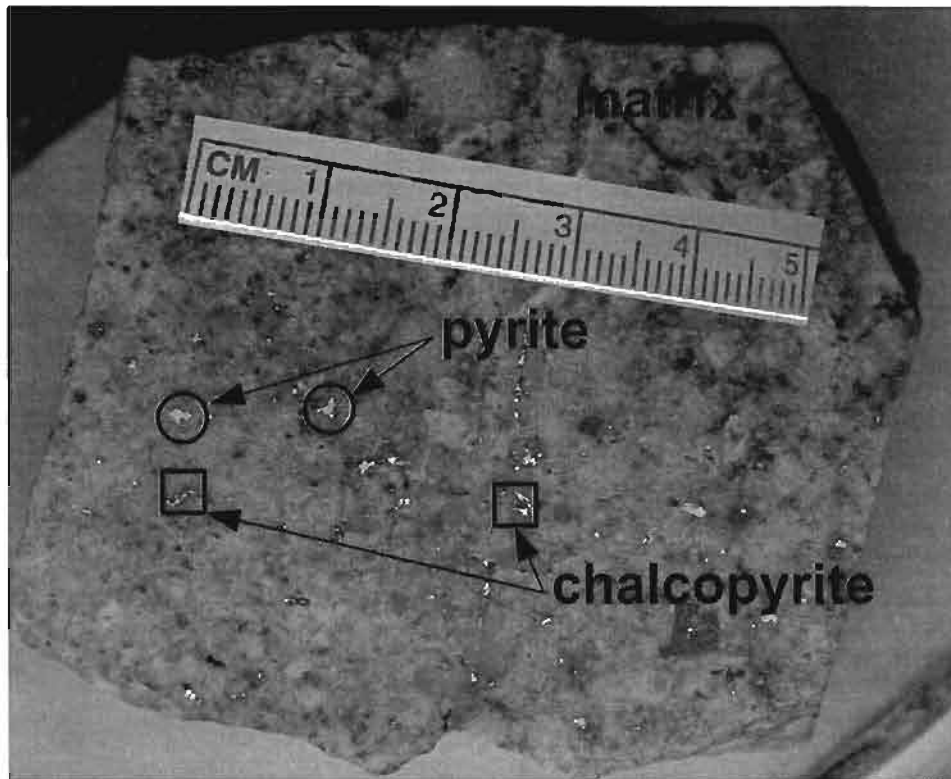


Figure 2.18. Sample SB03, Silver Bell, Arizona, chalcopyrite and pyrite in a feldspar and quartz matrix.

*Mahan et al.* [1986] observe a similar phase/imaginary part increase at higher frequencies (near  $10^3$  Hz) that is seen in the data from samples K01 M02, and SB03. Mahan attributed this to dielectric behavior at higher frequencies. Mahan also observed this behavior to start at lower frequencies for increasing matrix resistivity. Although sample SB03 contains chalcopyrite and pyrite it does not exhibit two IP peaks, possibly due to the order of magnitude greater volume fraction of the pyrite. Samples K01, M02, and SB03 are chosen for further analysis. The EM data for the additional 13 samples not selected for detailed analysis are included in Appendix B.



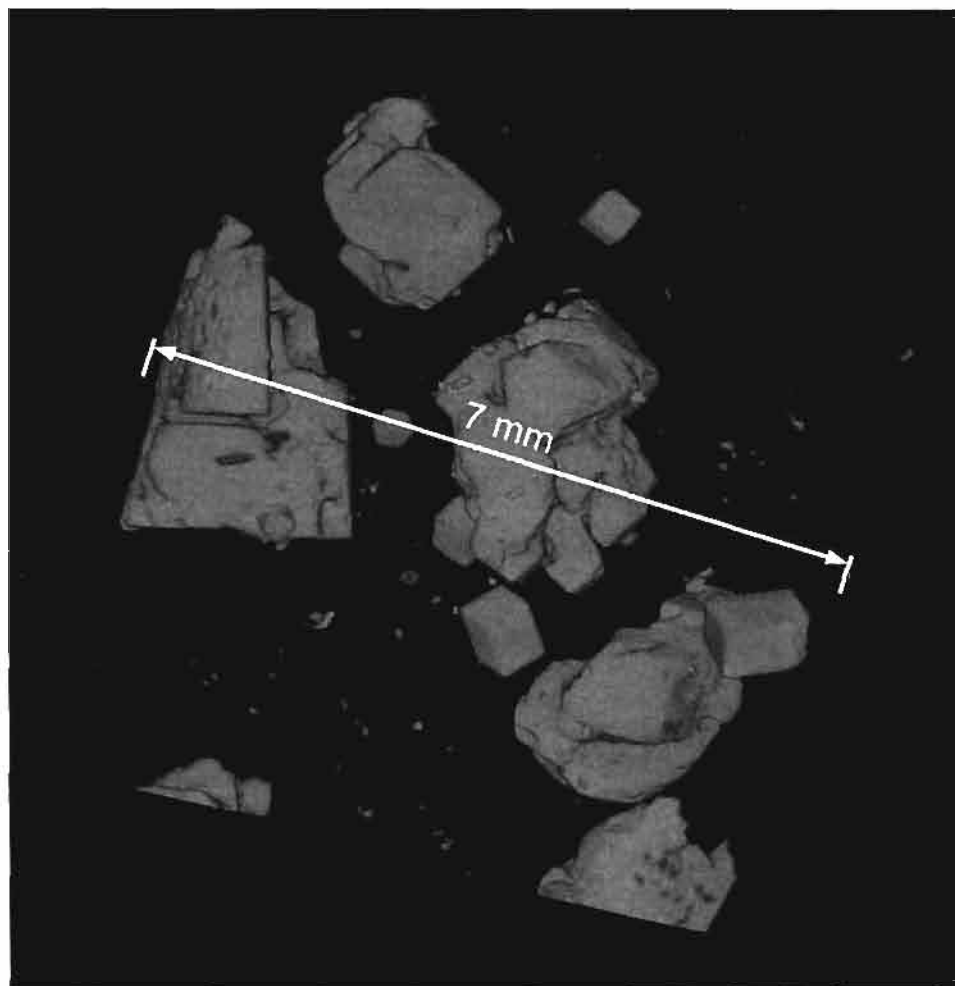


Figure 2.19. X-ray tomography image of Sample K01, Korri Kollo, Bolivia, pyrite in sericite and quartz matrix. The image has been optimized to show the pyrite.

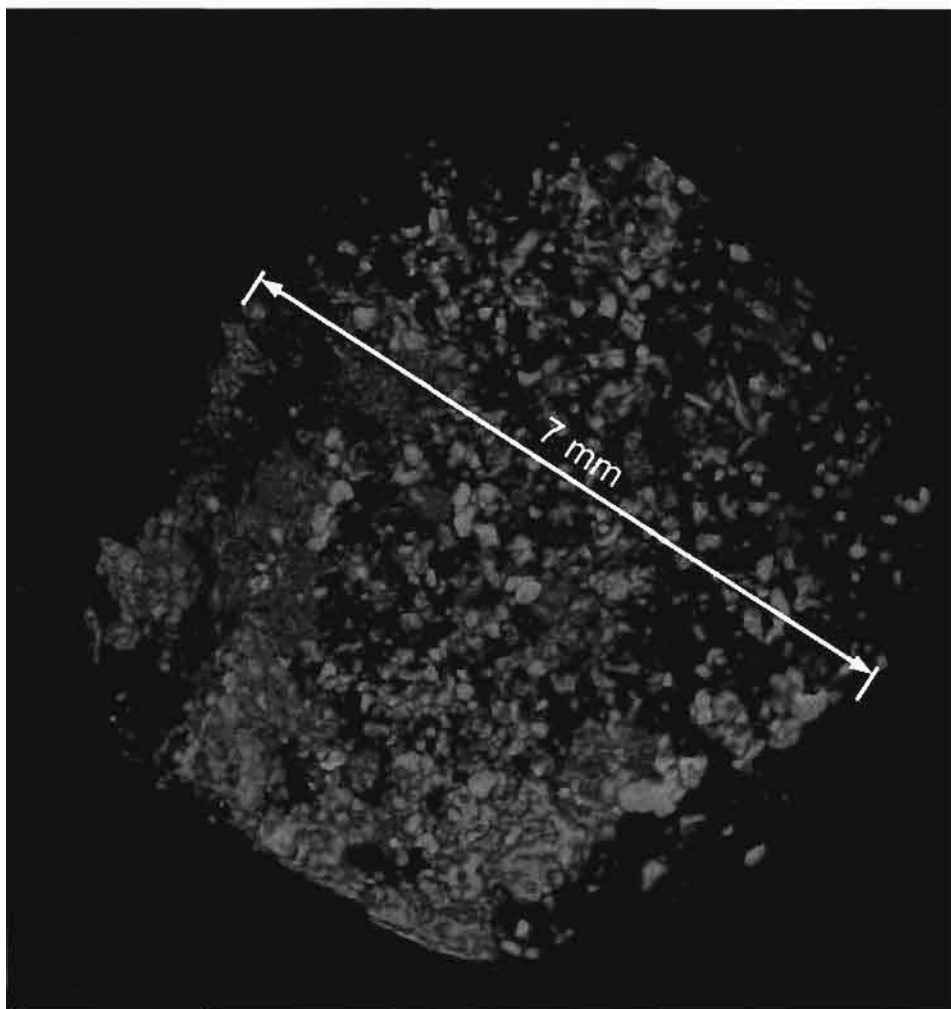
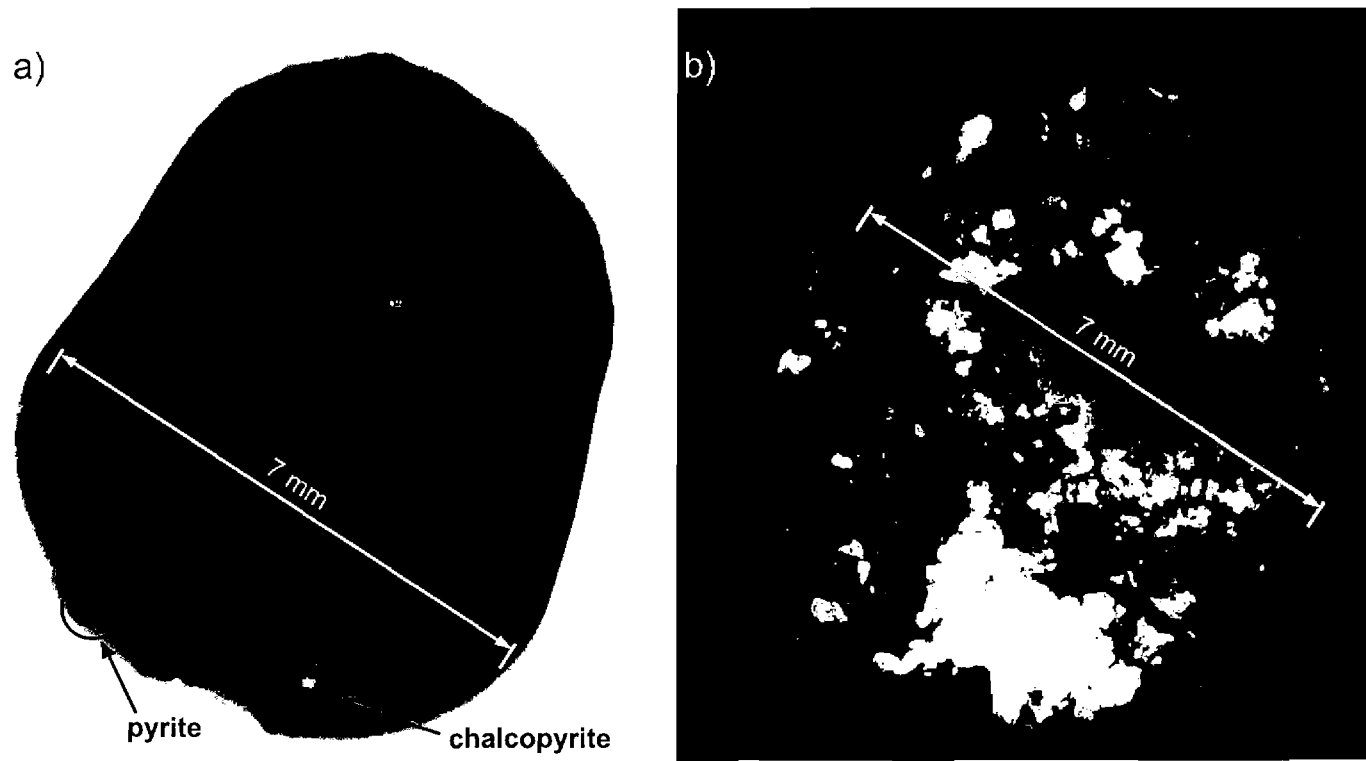


Figure 2.20. X-ray tomography image of Sample M02, Milford, Utah, pyrite in a feldspar and quartz matrix. The image has been optimized to show the pyrite.



**Figure 2.21.** X-ray tomography image of Sample SB03, Silver Bell, Arizona, chalcopyrite and pyrite in a feldspar and quartz matrix. a) Full core. b) Sulfides highlighted.

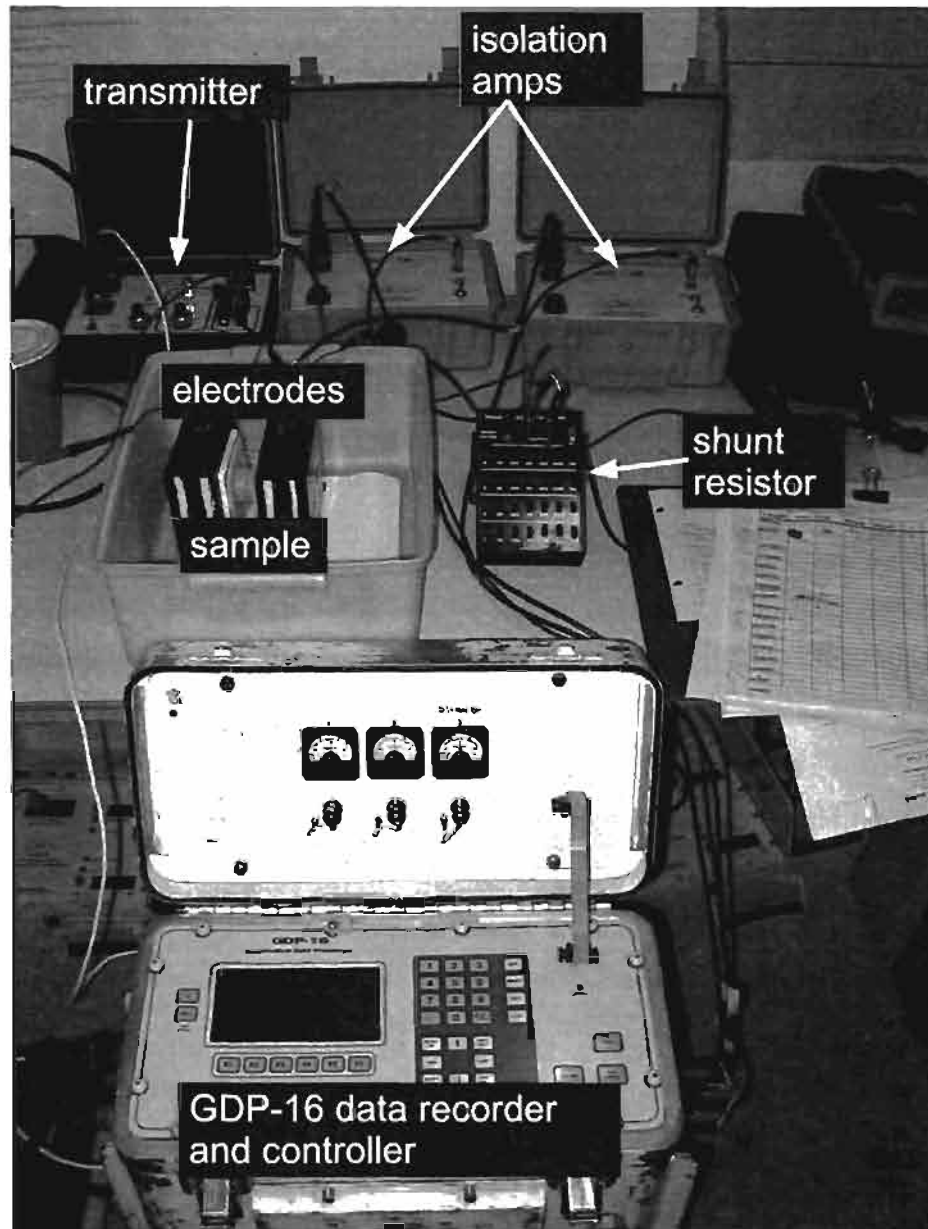
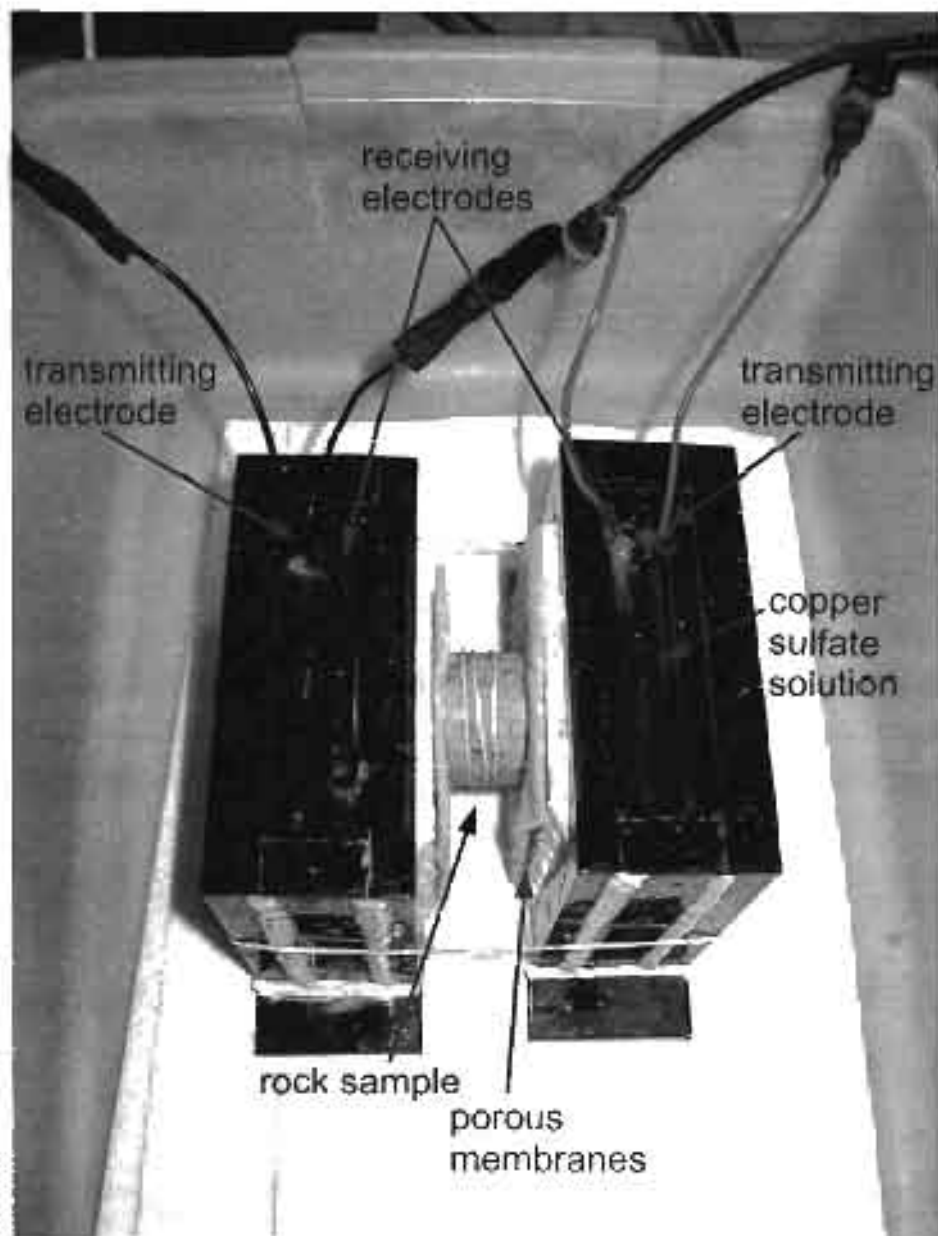
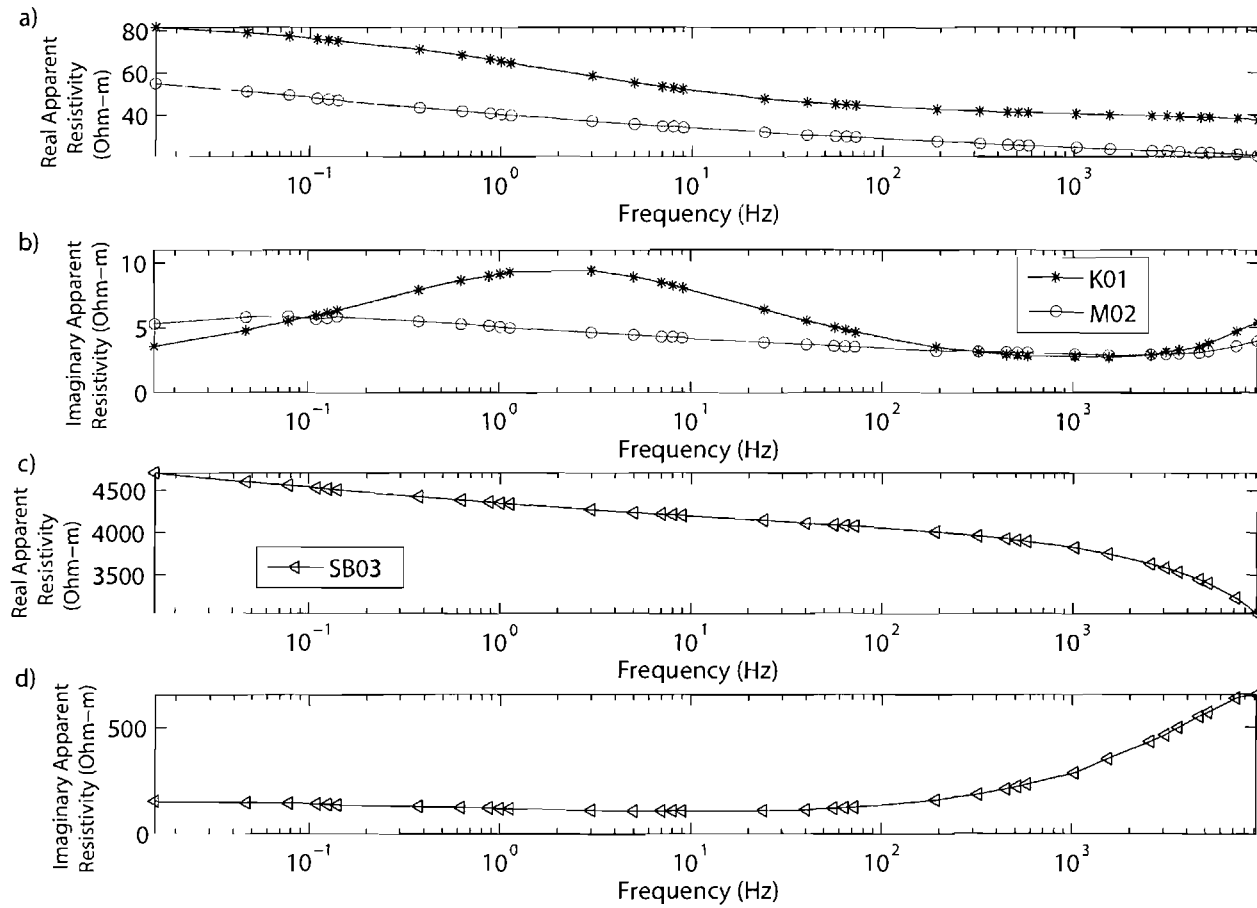


Figure 2.22. Recording system used at Zonge Engineering and Research Organization Inc. to obtain EM measurements.



**Figure 2.23.** Sample holder, rock sample, and receiving and transmitting electrodes. Note the rubber band to prevent surface current flow across the rock sample surface.



**Figure 2.24.** Apparent resistivity for samples K01, M02, and SB03. a) Real apparent resistivity for K01 and M02. b) Imaginary apparent resistivity for K01 and M02. c) Real apparent resistivity for SB03. d) Imaginary apparent resistivity for SB03.

## 2.8 GEMTIP Models of Rock Samples

GEMTIP models are built to fit the observed complex resistivity data using the information gained for each sample by the mineralogical assessment. Applying the developed GEMTIP inversion routines to the measured EM data enabled the recovery of  $\alpha$  and  $C$ . It was necessary to use a multiple of the volume fraction and  $m$  to achieve a good data fit from the GEMTIP models. This provided insight into problems of using of the current analytic solution based on a spherical grain assumption. Volume fraction ( $f$ ) and  $m$  are grouped into a new term  $k$  defined as:

$$k = f_i m_i, \quad (2.7)$$

where:

$$m_i = 3 \frac{\rho_0 - \rho_l}{2\rho_l + \rho_0} \quad (2.8)$$

to clarify discussion of the results. All data sets required a shift in the imaginary part given by Table 2.8.

### 2.8.1 Sample K01

The complex resistivity data for sample K01 were inverted for  $\alpha$  and  $C$  with the two-phase inversion algorithm with good results. The best data fit was achieved when three times  $k$  ( $3k$ ) was used. The misfit functional for  $3k$  is shown in Figure 2.25. Inversion results for the unmodified equation and  $3k$  are presented in Figure 2.25. The original predicted imaginary data and the  $3k$  predicted imaginary data fit the observed data well. The real data decay much faster as frequency increases than the original predicted data, while the  $3k$  predicted data decay more like

**Table 2.8.** Imaginary data shift to enable better inversion.

Sample	Imaginary shift
K01	-3
M02	-3
SB03	-125

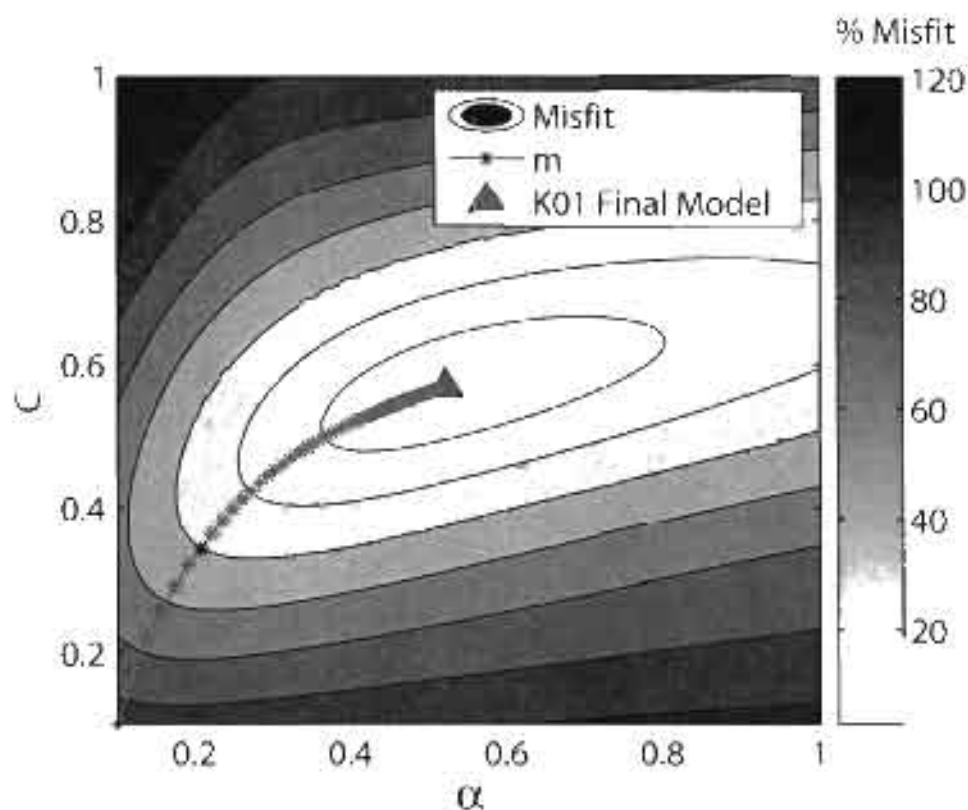


**Figure 2.25.** Misfit functional for two-phase inversion of Sample K01 when  $3k$  is used. Only imaginary data were used for inversion.

the observed data. Recovered  $\alpha$  and  $C$  values are listed in Table 2.9 with other inversion parameters. The complex resistivity data were combined with grain size distribution information from the X-ray tomography analysis and inverted using the two-phase  $N$  grain sizes inversion routine. To reduce the overdetermined nature of the problem, the 15 largest grain radii and their associated normalized volume fraction from the X-ray tomography were used. These 15 grains represented 90% of the pyrite volume in the sample. As with the previous inversion the real data decay faster than the predicted data requiring  $5k$  to be used for the best inversion results, shown in Figures 2.27 and 2.28. The variables used for this inversion are outlined in Table 2.10



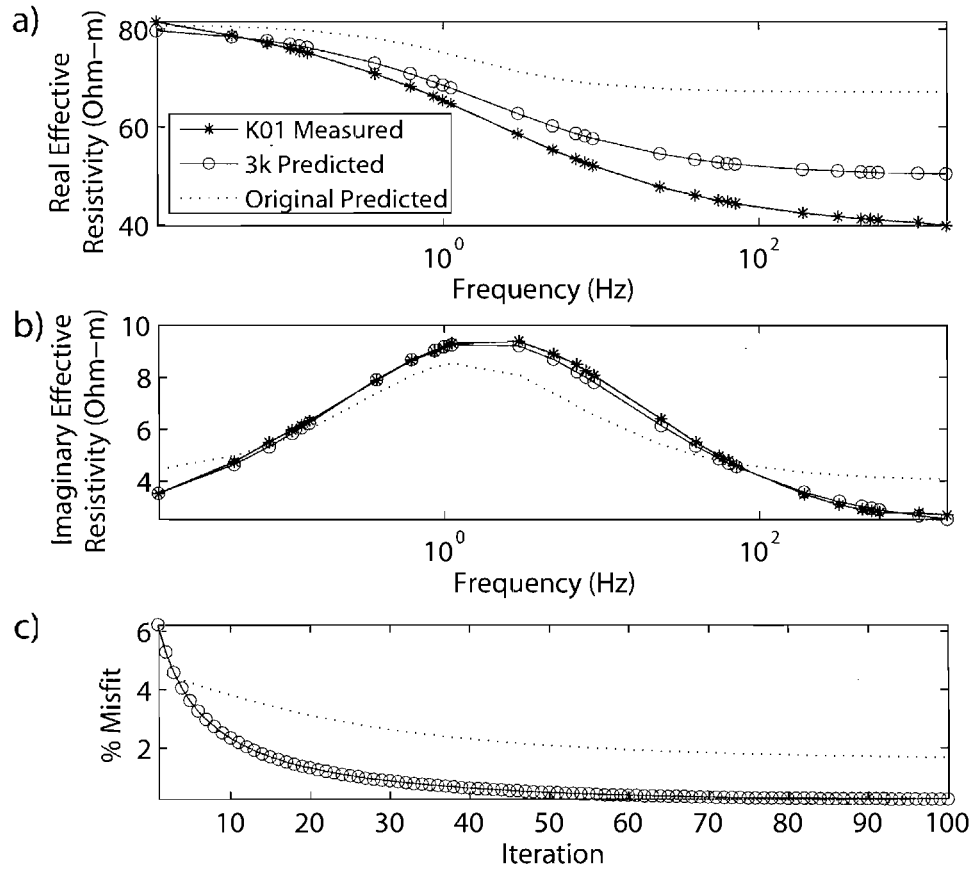


**Figure 2.26.** Inversion results for two-phase inversion of Sample K01 for  $k$  and  $3k$ . Only imaginary data were used for inversion. When  $3k$  is used data fit is improved and the misfit is lower. a) Real effective resistivity, b) Imaginary effective resistivity, c) Misfit vs. iteration.

**Table 2.9.** Variables for two-phase inversion of K01 for  $3k$ .

Variable	Units	Known	Recovered
$\rho_{matrix}$	Ohm-m	81	-
$f$	%	7	-
$C$	-	-	0.57
$\rho_{pyrite}$	Ohm-m	0.3	-
$a$	mm	2	-
$\alpha$	$\frac{\text{Ohm}\cdot\text{m}^2}{\text{sec}^2}$	-	0.57
$R$	-	-	10000

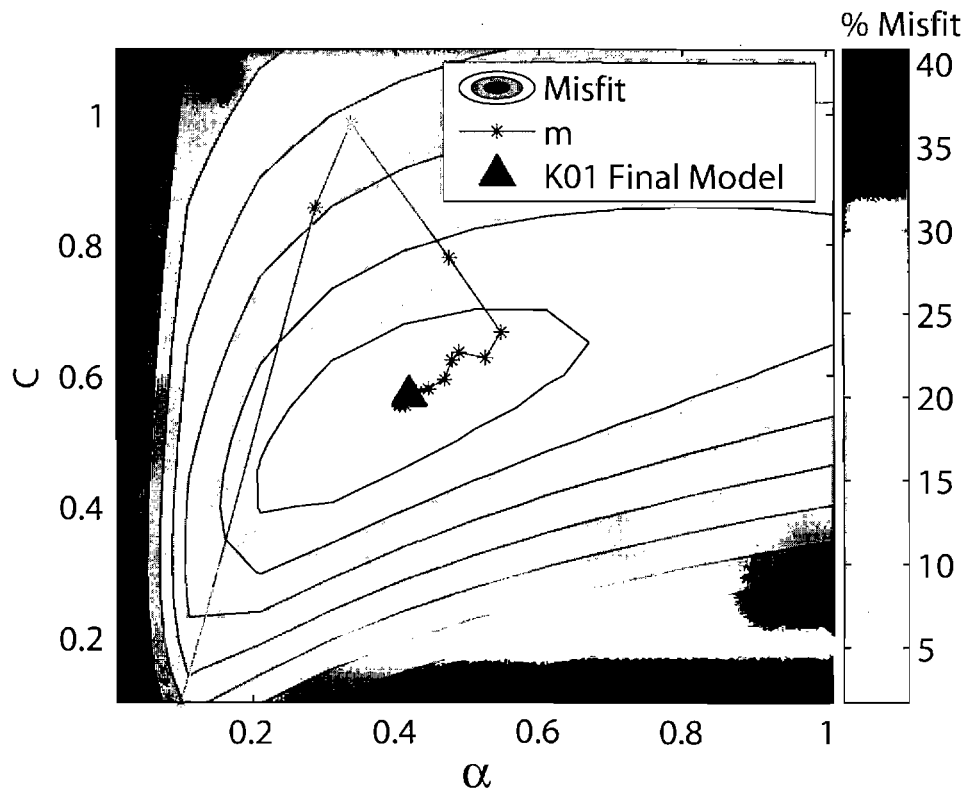


**Figure 2.27.** Misfit functional for  $N$  grain sizes one  $\alpha$  one  $C$  inversion of Sample K01 for  $5k$ .

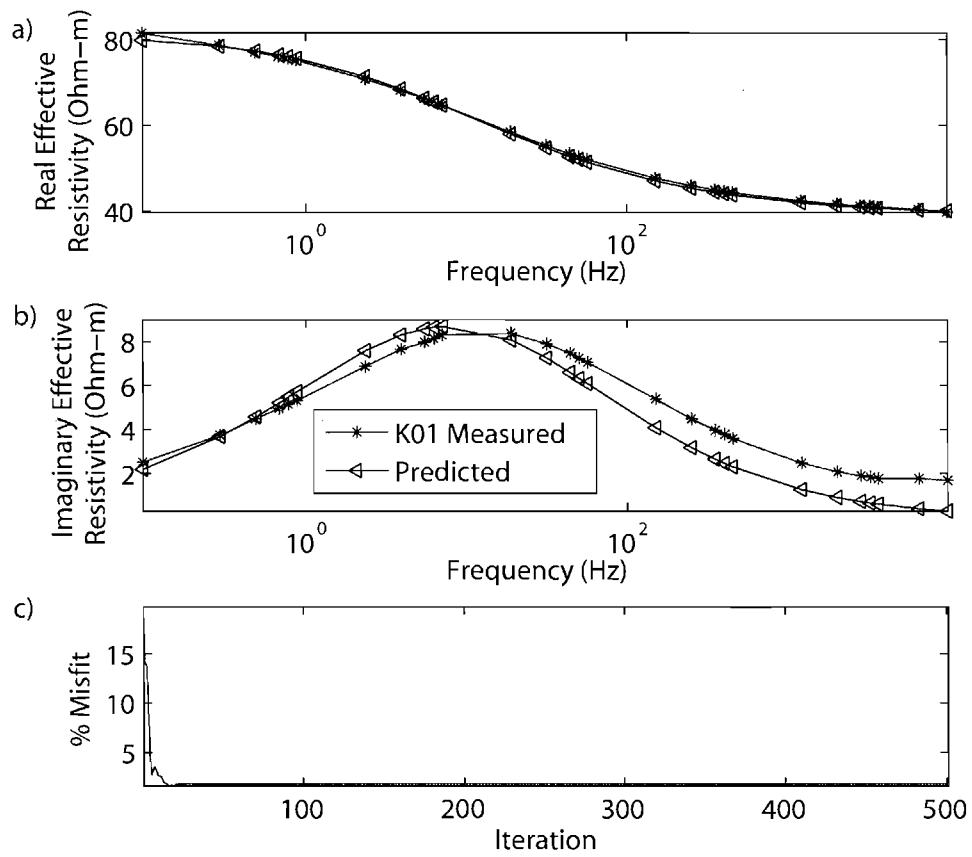


**Figure 2.28.** Inversion results for N grain sizes one  $\alpha$  one C inversion of Sample K01 for 5k. a) real effective resistivity, b) imaginary effective resistivity, c) misfit vs. iteration.

**Table 2.10.** Variables for N grain sizes one  $\alpha$  one  $C$  inversion of K01 for  $5k$ 

Variable	Units	Known	Recovered
$\rho_{matrix}$	Ohm-m	81 Ohm-m	-
$f$	%	7% total	-
$C$	-	-	0.42+0.03i
$\rho_{pyrite}$	Ohm-m	0.3	-
$a$	mm	15 sizes; 0.5 to 1.3 mm <sup>a</sup>	-
$\alpha$	$\frac{\text{Ohm}\cdot\text{m}^2}{\text{sec}^{\epsilon t}}$	-	0.57+0.07i
$R$	-	-	1000

<sup>a</sup>From X-ray tomography data analysis (See Table2.7.)

### 2.8.2 Sample M02

EM data for sample M02 were inverted with moderate success using the two-phase inversion algorithm. Both the real and imaginary data were used for the inversion, with the imaginary data multiplied by 7 to increase their influence. A multiple of  $k$  was needed for best results. Recovered values of  $\alpha$  and  $C$  are listed in Table 2.11. Figures 2.29 and 2.30 show inversion results when  $12k$  is used. The complex nature of the M02 pyrite grains caused radii determined from the volume approximation method given by Equation 2.6 to be an order of magnitude smaller than the maximum radii measured from selected marching cubes analysis polygon files. For this reason a second inversion was tried with a larger grain size (2 mm) with improved results, shown by figure 2.30.

**Table 2.11.** Variables for two-phase inversion of M02 for  $12k$ .

Variable	Units	Known	Recovered
$\rho_{matrix}$	Ohm-m	55	-
$f$	%	2	-
$C$	-	-	0.54 +0.30i
$\rho_{pyrite}$	Ohm-m	0.3	-
$a$	mm	0.1	-
$\alpha$	$\frac{\text{Ohm}\cdot\text{m}^2}{\text{sec}^{\epsilon t}}$	-	0.70 +0.04i
$R$	-	-	75000

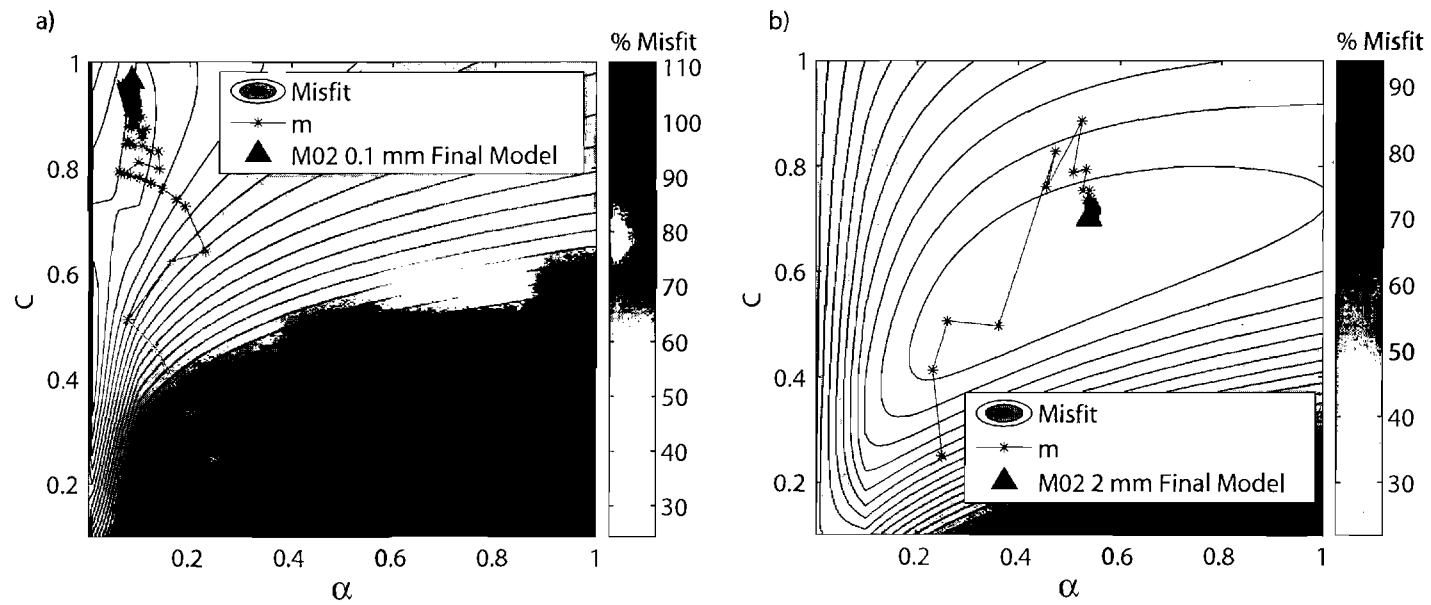


**Figure 2.29.** Misfit functionals for two-phase inversion of Sample M02 when  $12k$  is used. Real and imaginary data were used for inversion. Using a larger grain size improves the character of the misfit functional. a) Misfit Functional for 0.1 mm grain radius. b) Misfit functional for 2 mm grain radius.

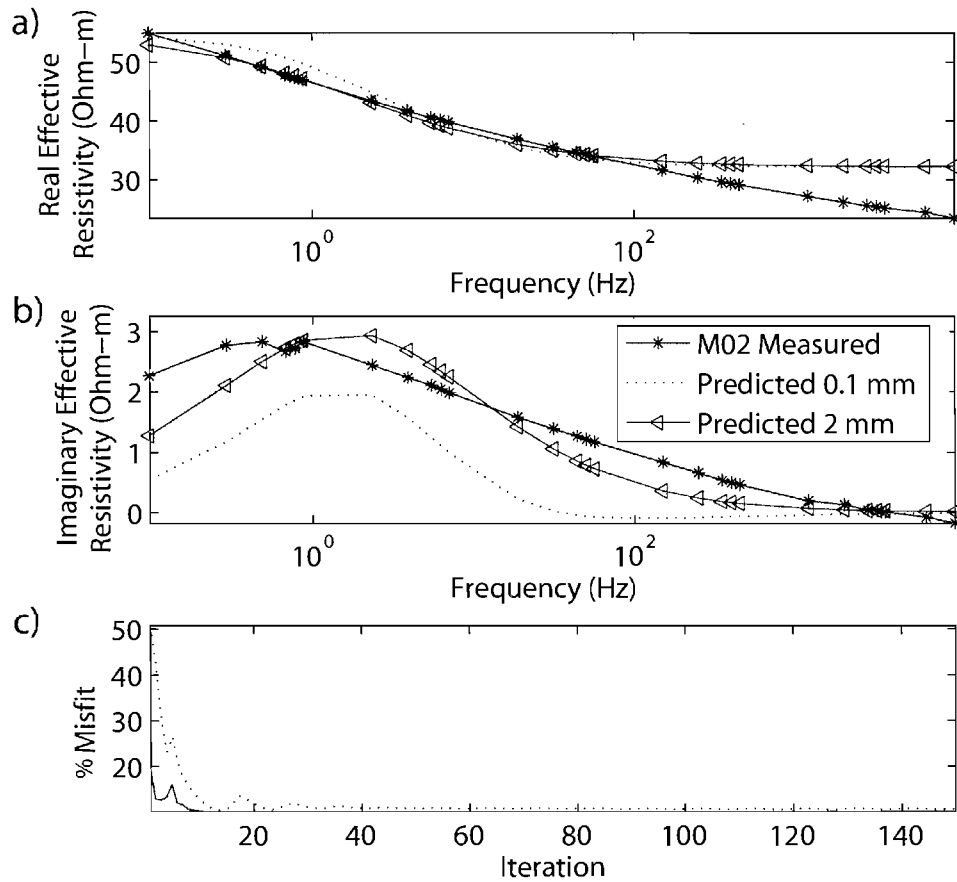


**Figure 2.30.** Inversion results for two-phase inversion of Sample M02 for 12k . Real and imaginary data were used for inversion. Data fit is improved by using the larger grain size from the qualitative marching cubes analysis. a) real effective resistivity, b) imaginary effective resistivity, c) misfit vs. iteration.

### 2.8.3 Sample SB03

Sample SB03 required the use of the N-phase inversion routine. Both the real and imaginary data were inverted to recover  $\alpha_1$ ,  $\alpha_2$ ,  $C_1$ , and  $C_2$ . In order to achieve the best results 10k for pyrite and 70k for chalcopyrite were used. The surface area to volume ratio is around seven times greater assuming spheres for the smaller chalcopyrite grains. Figure 2.31 shows the convergence of the inversion in model space. Predicted data, observed data, and misfit as a function of iteration are shown in Figure 2.32. GEMTIP is unable to model the higher frequency behavior of the complex resistivity for this sample. *Mahan et al.* [1986] encountered a similar difficulty fitting the *Wong* [1979] model to higher frequency data. Mahan felt the higher frequency data were influenced by the dielectric effect. The inversion resulted in a larger  $\alpha$  value than the other two samples. Table 2.12 outlines recovered and known variables for the inversion of SB03 data. The predicted data fit to the measured data is acceptable, but it required complex values of  $\alpha$  and necessitated  $C$  to be forced real.

**Table 2.12.** Variables for two-phase inversion of SB03 for  $3k$ .

Variable	Units	Known	Recovered
$\rho_{matrix}$	Ohm-m	81	-
$f_{pyrite}$	%	1	-
$f_{chalcopyrite}$	%	0.02	-
$C_{pyrite}$	-	-	0.29
$C_{chalcopyrite}$	-	-	0.35
$\rho_{pyrite}$	Ohm-m	0.3	-
$\rho_{chalcopyrite}$	Ohm-m	0.004	-
$a_{pyrite}$	mm	0.5	-
$a_{chalcopyrite}$	mm	0.075	-
$\alpha_{pyrite}$	$\frac{\text{Ohm}\cdot\text{m}^2}{\text{sec}^{c_i}}$	-	4+4.5i
$\alpha_{chalcopyrite}$	$\frac{\text{Ohm}\cdot\text{m}^2}{\text{sec}^{c_i}}$	-	4.5+1.1i
$R$	-	-	10000

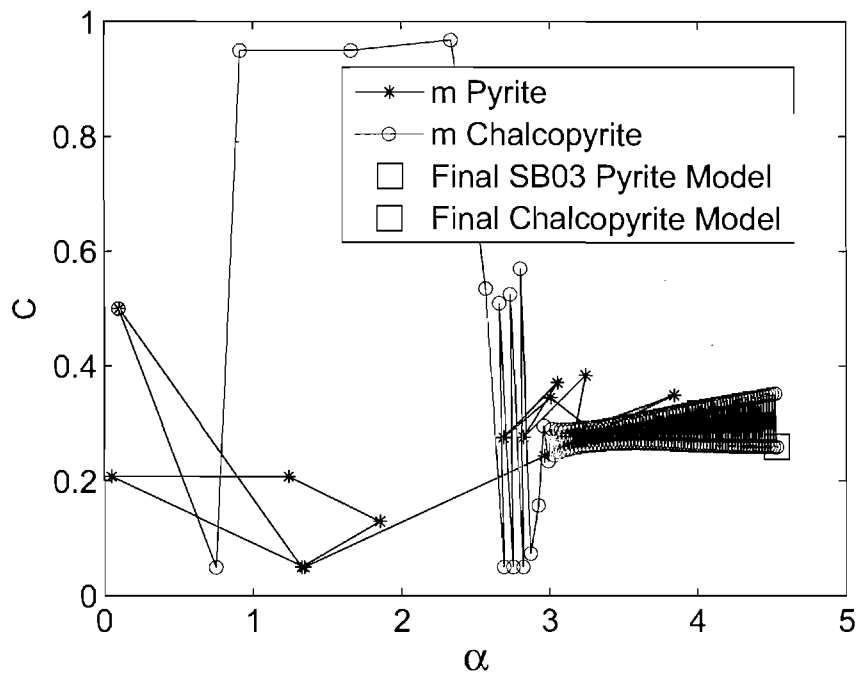


**Figure 2.31.** Convergence plot in model space for three phase inversion of Sample SB03 when  $10k$  is used for pyrite and  $70k$  is used for chalcopyrite. Real and imaginary data were used for inversion.  $C$  was forced to be real.

#### 2.8.4 Discussion

All inversions required a multiple of  $k$  to be used for best results. Volume fraction is well constrained; therefore the error most likely lies in the term  $m$ . In both approaches by Wong [Wong, 1979; Wong and Strangway, 1981] a volume fraction greater than the true value was needed to achieve a good agreement with the observed data. The term  $m$  is derived using a spherical grain assumption. Surface area is generally considered the controlling factor of IP phenomena [Slater, 2006; Frasier, 1964; Sumner, 1976; Lou, 1998]. Many pyrite grains in sample K01 exhibit cubic form and others are elongated spheroids. For sample K01 the true surface area to volume ratio is 4.5 times greater than the spherical surface area to volume ratio assuming a radius of 2 mm. Because the multiple of  $k$  needed appeared to be related to surface area, rigorous surface area and volume calculations were conducted, shown by Table 2.13. Mahan *et al.* [1986] observed peak IP frequency



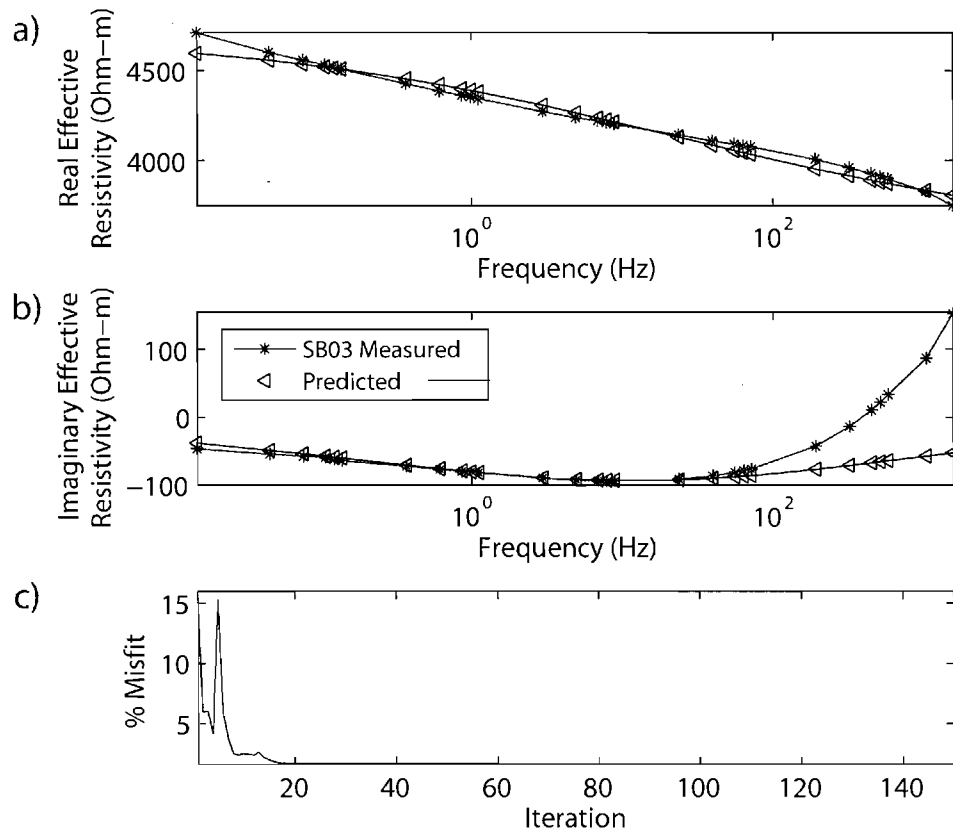


**Figure 2.32.** Inversion results for for three phase inversion of Sample SB03 when  $10k$  is used for pyrite and  $70k$  is used for chalcopyrite. Real and imaginary data were used for inversion.  $C$  was forced to be real. a) Real effective resistivity. b) Imaginary effective resistivity. c) Misfit vs. iteration.

to vary as  $\frac{1}{radius^2}$  for smaller grains and  $\frac{1}{radius}$  for larger grains implying surface area could be playing an important role, as the smaller grains have more surface area per volume. A new derivation with a grain dependent surface area per unit volume term could be in order. For example, the geometric factor relating surface area to radii for a sphere is  $\frac{3}{radius}$ , and for a cube containing the sphere it would be  $\frac{6}{radius}$ . This term could be user selectable depending on expected grain shape.

Sample K01 showed the best inversion results with the most reasonable  $\alpha$  and  $C$  values. This is most likely due to the classic shape of the imaginary apparent resistivity curve and the fact the complete IP peak is well captured by the recorded frequencies; additionally K01 has the simplest grain structure (see Figure 2.33).

The inversion results for M02 and SB03, especially the imaginary data fit, are not as good, but promising. Possible problems could include, more complex media, the need for more data, noisier data, and incorrect geometrical assumptions. The spherical grain assumption is best fulfilled by sample K01. A large portion of M02's grains are interconnected, irregular, and elongated. The pyrite and chalcopyrite in sample SB03 are irregularly shaped and often are in close proximity. To illustrate complex grain geometries select grains for each sample are presented in Figure 2.33. Geometrical information for each the selected grains is presented in Table 2.14. The complex shapes exhibited by the sulfides in samples M02 and SB03 show the difficulty in assigning a radius using volume. This complexity could also lead to the errors in the term  $\tau$  of Equation 2.1 because it is a function of radius. The radius from volume approximation used could underestimate the "effective radius" controlling the IP phenomenon, meaning the complex grains are actually behaving like much larger radii spherical grains. This may explain why K01's peak IP frequency is similar to that observed by Ostrander and Zonge's for similar grains sizes, while the recorded peak IP frequency is considerably lower than Ostrander and Zonge's for samples M02 and SB03. The results prove the difficulty of applying spherical assumptions to geophysical problems. The inversions performed and their matched predicted data support the viability of the GEMTIP conductivity model, but new analytic solutions need to be explored.

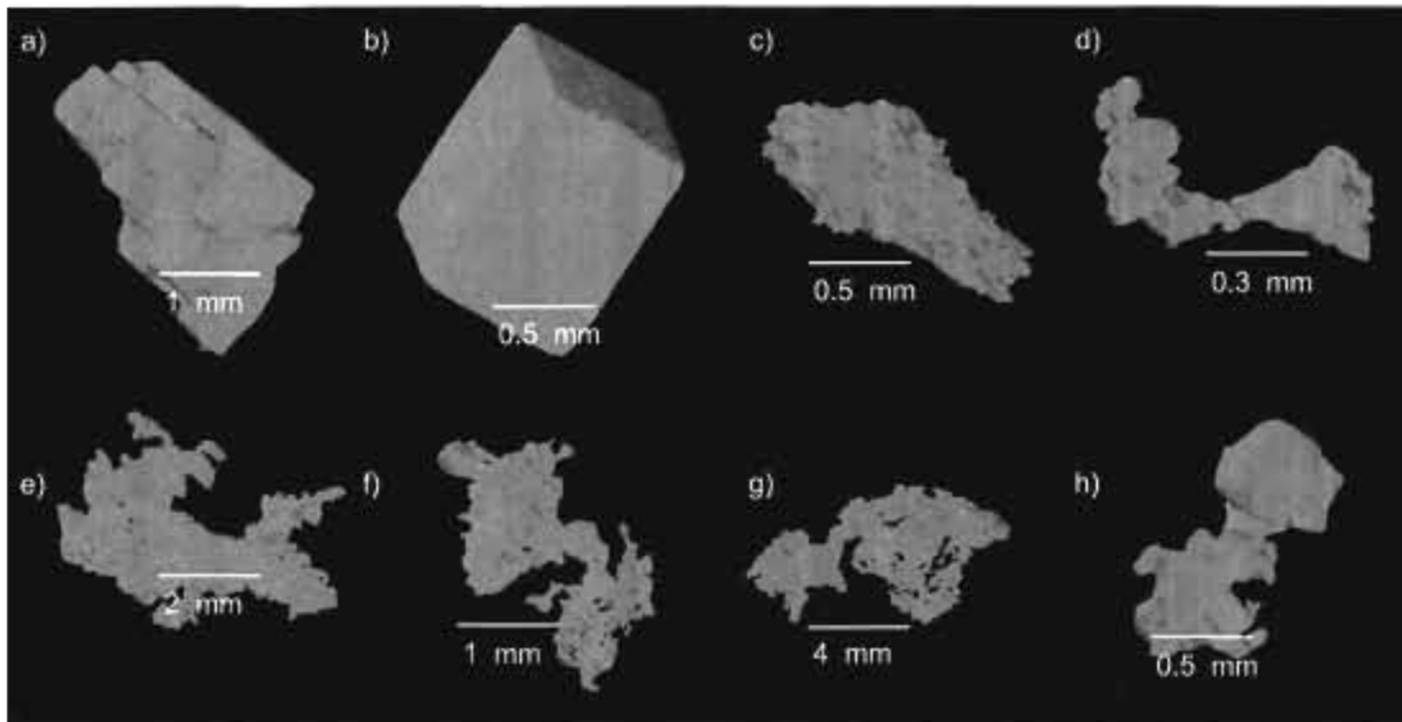


Figure 2.33. Individual grain images from marching cubes analysis. a) and b) Sample K01. c) and d) Sample SB03 chalcopyrite. e) and f) Sample M02. g) and h) Sample SB03 pyrite. Table 2.14 has geometric information for each grain show in this figure.

**Table 2.13.** True surface area to volume ratios of samples K01, M02, and SB03 (pyrite and chalcopyrite). The trend in true SAVR follows the trend of multiples of k used. There is good agreement between the multiple of k used and  $\frac{\text{true SAVR}}{\text{spherical SAVR}}$  for sample K01.

Sample	Assumed Grain Size	Resulting Total Surface Area	Spherical Assumption Surface Area to Volume Ratio	True Total Sulfide Volume	True Total Sulfide Surface Area	True Surface Area to Volume Ratio (SAVR)	k Multiple Used	$\frac{\text{true SAVR}}{\text{spherical SAVR}}$
Units	mm	m <sup>2</sup>	m	m <sup>3</sup>	m <sup>2</sup>	m	-	-
K01	2	$6.06 \cdot 10^{-5}$	1500	$4.04 \cdot 10^{-8}$	$2.75 \cdot 10^{-4}$	6810	3, 5 <sup>a</sup>	4.54
M02	0.1	$6.63 \cdot 10^{-4}$	30000	$2.21 \cdot 10^{-8}$	$8.34 \cdot 10^{-4}$	3780	12	1.26
SB03 pyrite	0.075	$5.05 \cdot 10^{-5}$	6000	$8.41 \cdot 10^{-9}$	$1.96 \cdot 10^{-4}$	23300	10	3.89
SB03 chalcopyrite	0.02	$5.56 \cdot 10^{-6}$	40000	$1.39 \cdot 10^{-10}$	$7.73 \cdot 10^{-6}$	55600	70	1.39

<sup>a</sup>For a radii of 2 mm  $3k$  was used. When using the 15 largest grain radii  $5k$  was used.

**Table 2.14.** Geometric information for grains shown in Figure 2.33. Grain ID refers to the letter assigned in Figure 2.33. Surface area and volume were computed using marching cubes [Lorensen and Cline, 1987].

Grain ID	Sample	Maximum Dimension	Volume	Surface Area	Surface Area to Volume Ratio
		mm	m <sup>3</sup>	m <sup>2</sup>	m
a	K01	3.9	3.2 <sup>5</sup>	3.4 <sup>10</sup>	9.6 <sup>4</sup>
b	K01	1.7	2.1 <sup>6</sup>	1.1 <sup>11</sup>	1.9 <sup>5</sup>
c	SB03 chalcopyrite	1.6	1.4 <sup>6</sup>	2.5 <sup>12</sup>	5.5 <sup>5</sup>
d	SB03 chalcopyrite	0.6	3.2 <sup>7</sup>	2.5 <sup>13</sup>	1.2 <sup>6</sup>
e	M02	5.0	3.0 <sup>5</sup>	5.6 <sup>11</sup>	5.3 <sup>5</sup>
f	M02	2.6	6.4 <sup>6</sup>	7.7 <sup>12</sup>	8.3 <sup>5</sup>
g	SB03 pyrite	8.6	7.8 <sup>5</sup>	2.1 <sup>10</sup>	3.7 <sup>5</sup>
h	SB03 pyrite	1.4	2.6 <sup>6</sup>	6.5 <sup>12</sup>	4.0 <sup>5</sup>

## CHAPTER 3

# DEPOSIT SCALE MODELING OF A PORPHYRY SYSTEM, GEMTIP APPLICATION ON A LARGE SCALE

### 3.1 Introduction

Porphyry deposits are an important exploration target and are economic depending on mineralization type. The ability to discriminate mineral content of a porphyry system would be useful to exploration geoscientists; therefore 3-D EM modeling of this complex geologic system is conducted to assess the effect of pyrite and chalcopyrite mineralization. Three dimensional integral equation method modeling was first conducted by *Hohmann* [1975] when he modeled 3-D anomalous structure in a uniform halfspace. *Wanamaker et al.* [1984] expanded the integral equation technique was to include a layered earth background. Three dimensional complex resistivity using the Cole-Cole model was modeled by *Lou* [1998]. By incorporating Cole-Cole modeling capability into the Consortium for Electromagnetic Modeling and Inversion EM IE code *Lee and Zhdanov* [2005] aided the development of 3-D modeling using the GEMTIP conductivity model. Successful complex resistivity inversion techniques have been developed [*Cox and Zhdanov*, 2007; *Goold et al.*, 2007; *Yoshioka and Zhdanov*, 2005; *Yoshioka*, 2004]. Prior 3-D IP modeling has not included the GEMTIP model and mineralization types. Extensive forward modeling of porphyry systems has not been conducted in the past. To facilitate modeling a porphyry system the Simple Porphyry Model is developed to include all the classic zones of a porphyry system. The Simple Porphyry Model is modeled using the Integral Equation method EM forward modeling code IBCEM3DIP developed by the Consortium for Electromagnetic Modeling and Inversion (CEMI) [*Lee and*

*Zhdanov*, 2005; *Wanamaker et al.*, 1984; *Hohmann*, 1975]. The new conductivity model GEMTIP is added to IBCEM3DIP to include mineralogy information (i.e. sulfide type, etc.). A specialized front end to IBCEM3DIP is developed to input the geometry of The Simple Porphyry Model into IBCEM3D. Forward modeling of the Simple Porphyry Model with different sulfide distributions is conducted.

### 3.2 Porphyry Overview

To put the 3-D EM modeling of this study into better context a simple overview of porphyry systems follows. Porphyry systems are associated with magmatic intrusions that form the root of a strata volcano. Hydrothermal circulation in the intrusion and preexisting country rocks is responsible for the mineralization. Figure 3.1 illustrates the many zones of hydrothermal alteration. Mineralization occurring in the intrusion forms the porphyry deposit while distal mineralization in veins and fractures is often responsible for skarn type deposits. In general the hydrothermal fluids deposit a pyrite shell (phyllitic zone) around the intrusion and a smaller mineralized zone (ore zone). Commonly, later weathering effects of meteoric waters create two new zones, the enriched zone, and a leached cap shown in Figure 3.2. For the case of a copper-bearing porphyry the meteoric waters remove copper and other elements from the leached cap leaving behind hematite, other oxides and/or sulfates. The copper rich fluids from the leached cap concentrate copper by converting chalcopyrite to chalcocite in the enriched zone. Chalcocite is 78% by weight copper compared to chalcopyrite which is 33% copper by weight. Porphyry deposits are an interesting and complex geologic system of economic importance.

### 3.3 Simple Porphyry Model Development

A simplified model of a porphyry system was developed to test mineral discrimination, detectability, the effects of nearby geologic structures, and optimal survey design. For modeling purposes the Simple Porphyry Model was constructed based on known geologic information [*Titley*, 1982; *Pierce and Bolm*, 1995]. Geoelectric values are shown in Figure 3.3 (*J. Inman, pers. commun.*). The simplified porphyry

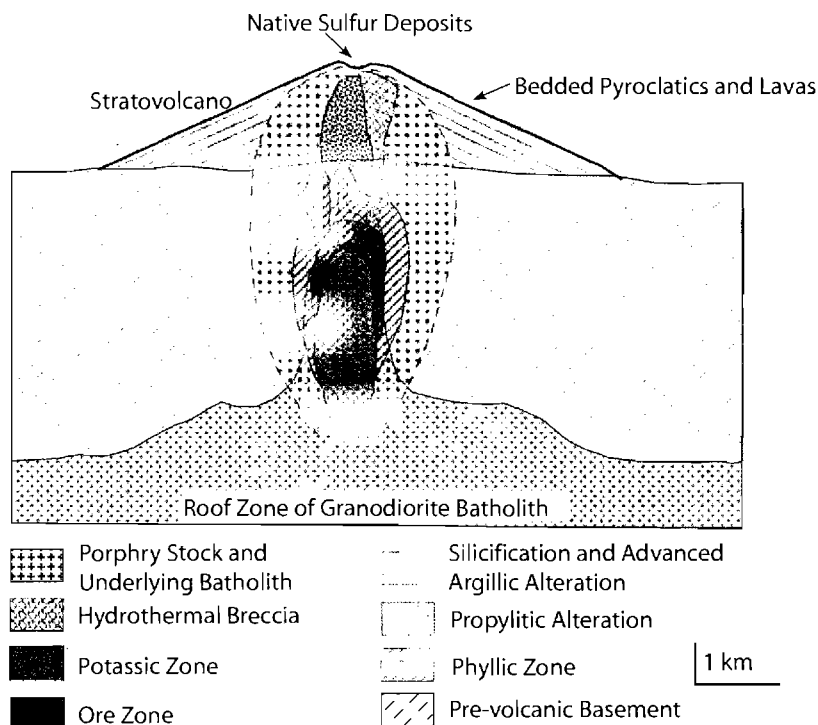


**Figure 3.1.** A geologic overview of the creation of a porphyry deposit after *Sillitoe* [1973]. Idealized porphyry copper system shown in the magmatic hydrothermal phase. Modified from E. U. Petersen (pers. communication.)

model, shown in Figure 3.4, incorporates the classic zones seen in many porphyry deposits including supergene zones: leached cap, enriched zone and the unweathered zones: pyrite shell, ore zone, and barren core of the intrusion. A normal fault was also included near the deposit. This simplified geometry allows for easy modeling using the newly developed front end to IBCEM3DIP

### 3.4 GEMTIP Incorporation into INTEM

The GEMTIP conductivity model is now incorporated into the MATLAB based existing CEMI forward modeling code IBCEM3DIP *Lee and Zhdanov* [2005]. IBCEM-3DIP allows the modeling of an additional anomalous domain, the IBC body, to serve as an inhomogeneous background. Four conductivity options are now available for use in IBCEM3DIP: direct current, conductivity and phase (constant IP across



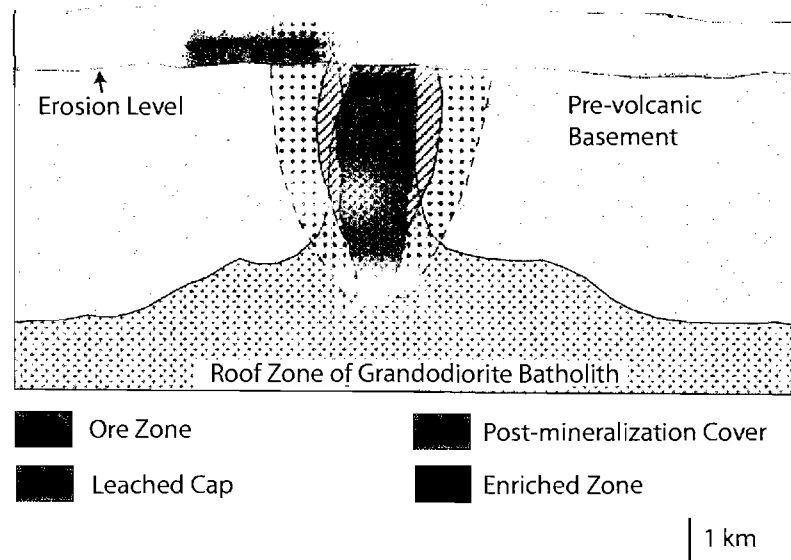


**Figure 3.2.** A geologic overview of a supergene weathered porphyry deposit after *Sillitoe* [1973]. Enriched zone shown in dark grey. Leached cap shown in dark red. Modified from *E. U. Petersen* (pers. communication.)

all frequencies), Cole Cole, and GEMTIP. The first deposit scale application of GEMTIP was to conduct forward modeling of porphyry ore deposit rocks using the developed Simplified Porphyry Model (Figure 3.4).

### 3.5 Simple Porphyry Model Front End

In order to create the complex geometry of a the Simple Porphyry Model a custom front end to IBCEM3DIP was created. This code uses several geometric logic statements to assign a 1-D layered earth background, fill the anomalous domain, and create a fault structure with the IBC body. These three features are identified in Figure 3.5. All the classic zones illustrated in the Simple Porphyry Model are included as shown by Figure 3.5. Fault geometry, cover geometry, and deposit depth can be easily changed. Additionally, enriched zone thickness, leached cap

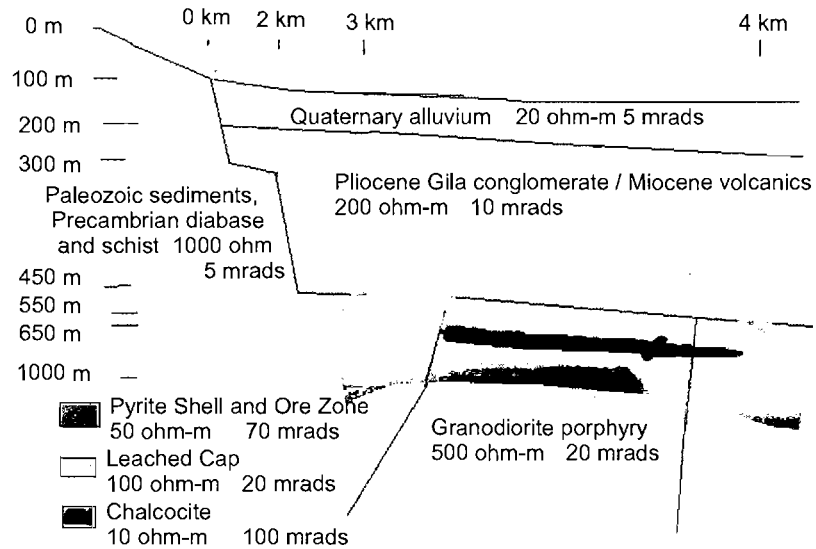


**Figure 3.3.** Schematic Southwest US copper porphyry geological/geophysical model (J. Inman, pers. commun.). It contains basic scale information, geologic units, and geoelectrical properties. A normal fault shown on the left side.

thickness, intrusion diameter, deposit aspect ratio, pyrite shell geometry, ore zone geometry, and other individual deposit characteristics can be changed. Geoelectric parameters including GEMTIP variables are assigned for each rock type in the model. With the newly developed front end, complex geoelectric structures can be easily modeled with IBCEM3DIP.

### 3.6 Deposit Scale Forward Modeling

Forward modeling of a porphyry system is accomplished using the new front end to IBCEM3DIP. GEMTIP variables are assigned to the enriched zone, pyrite shell and ore zone to see their effect on the deposit scale. The effective resistivity of the enriched zone, pyrite shell and ore zone is plotted in Figure 3.6. Geometry was based on the Simplified Porphyry Model. Resistivity values were based on the the Southwest US porphyry model shown in Figure 3.3. Figure 3.5 gives a 3-D

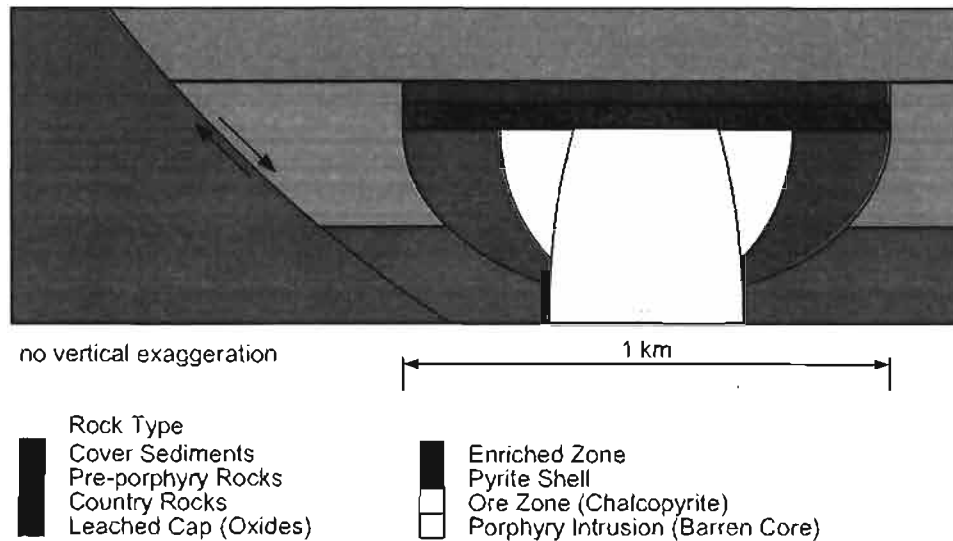


**Figure 3.4.** The Simplified Porphyry Model. Representation of a simplified porphyry system that can be easily modeled using CEMI EM forward modeling codes. This representation incorporates the classic zones of a porphyry deposit and a normal fault.

view of the forward models created. A 2-D 5000 m dipole-dipole survey was used perpendicular to the strike of the fault and crossing the center of the deposit. Four variations of the basic model: Model 1, Model 2, Model 3, and Model 4 are shown in cross section in Figure 3.7. The resulting pseudosections from Models 1, 2, 3, and 4 are presented in Figures 3.8, 3.9, 3.10, and 3.11. Tables 3.1, 3.3, 3.4 and 3.2 give details of each model, deposit geometry, and survey design details. An illustration of how a pseudo section is created is shown by Figure 3.12.

Forward modeling results for Model 1 in Figures 3.8 and 3.9 show a conductivity and phase anomaly centered around the ore body. The fault has some effect in the resistivity data but little effect in the phase data due to the low polarizability assigned to the basement rocks. Although the sulfide distribution is different for Models 2, 3, and 4 the apparent resistivity data at 1 Hz and 8 Hz look similar. In contrast the apparent phase data are distinct for each model. The similar resistivity pseudosections are explained by the similar resistivity values of the pyrite shell and ore zone. The ore zone and pyrite shell were assigned different IP parameters based on previous studies [Pelton *et al.*, 1978; Ostrander and Zonge, 1978] assigning

**Table 3.1.** Geometry of 3-D porphyry model.

Unit	Depth to Top (m)	Thickness (m)	Diameter (m)
Cover Sediments	-	50	-
Pre-porphyry Rocks	50	500	-
Country Rocks	550	-	-
Leached Cap	50	100	1000
Enriched Zone	150	100	1000
Pyrite Shell	250	≈600	1000
Chalcopyrite	250	≈300	660
Porphyry Intrusion	250	1300	400

**Table 3.2.** Modeling parameters and performance summary for synthetic data presented in Figures 3.8, 3.9, 3.10, and 3.11.

Survey Type	2-D 200 m dipole dipole
survey length	5000 m
Tx Rx Pairs	1430 per frequency
frequencies	0.125, 0.5, 1, 4, 8, and 16 Hz
Conductivity Model	GEMTIP
Anomalous Body	2000 cells
IBC Body	2000 cells
PC Time	5 hours
PC Type	2 GHz Pentium, 2 GB RAM

pyrite with a stronger IP response (see Figure 3.6). These differences produce the unique phase data. The distinction in phase and corresponding complex resistivity underscore the importance of complex resistivity and the IP effect for EM mineral exploration.

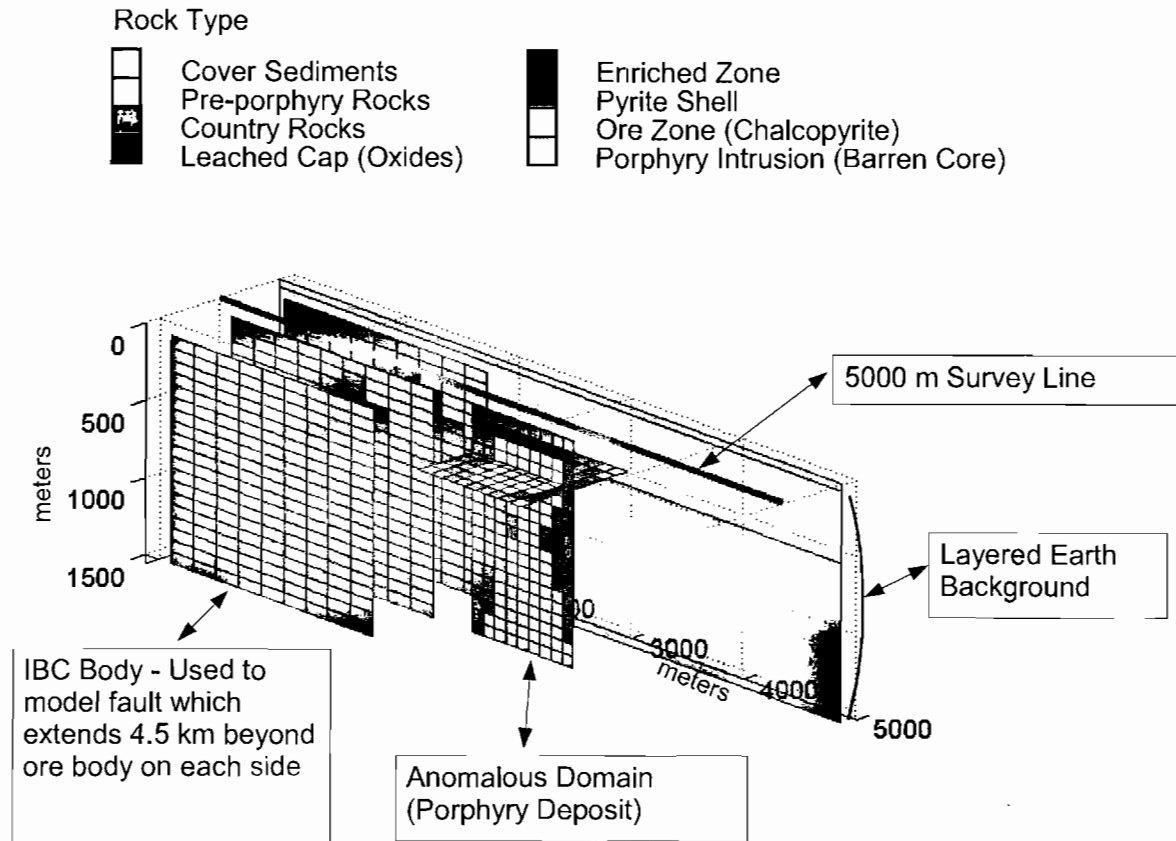


**Figure 3.5.** The framework for porphyry forward modeling using the CEMI developed code IBCEM3DIP for MATLAB . The above diagram shows the anomalous domain, the location of the survey line, the layered earth background, and the inhomogeneous background (IBC body) for the data presented in Figures 3.8, 3.9, 3.10, and 3.11. Complete details of survey design and model descriptions are give in Tables 3.1, 3.3, 3.4 and 3.2.

**Table 3.3.** Geoelectric and mineralogic parameters for all Model 1.

Model 1								
Geologic Unit	$\rho_{matrix}$	Phase 1	$\rho_{phase1}$	$f_{phase1}$	Multiple of $k$	$a_{phase1}$	$\alpha_{phase1}$	$C_{phase1}$
	Ohm-m		Ohm-m	%		mm	$\frac{Ohm \cdot m^2}{sec^2}$	
Cover Sediments	20	-	-	-	-	-	-	-
Pre-porphyry Rocks	200	-	-	-	-	-	-	-
Country Rocks	1000	-	-	-	-	-	-	-
Leached Cap	100	-	-	-	-	-	-	-
Enriched Zone	10	chalcocite	0.004 <sup>a</sup>	10	10	1	0.85	0.5
Pyrite Shell	50	pyrite	0.3	5	10	2.5	0.5	0.75
Ore Zone	40	chalcopyrite	0.004	5	10	1	0.85	0.5
Porphyry Intrusion	500	-	-	-	-	-	-	-

<sup>a</sup>Nabighian [1988]

**Table 3.4.** Geoelectric and mineralogical parameters for all Models 2-4.

<b>Model 2</b>	$\rho_{matrix}$	Phase 1	$\rho_{phase1}$	$f_{phase1}$	Multiple of $k$	$a_{phase1}$	$\frac{\alpha_{phase1}}{sec^c}$	$C_{phase1}$
Geologic Unit	Ohm-m		Ohm-m	%		mm		
Cover Sediments	20	-	-	-	-	-	-	-
Pre-porphyry Rocks	200	-	-	-	-	-	-	-
Country Rocks	1000	-	-	-	-	-	-	-
Leached Cap	100	-	-	-	-	-	-	-
leached cap			not present in model					
Enriched Zone			not present in model					
Pyrite Shell	50	pyrite	0.3	5	10	2.5	0.5	0.75
Ore Zone	40	chalcopyrite	0.004	5	10	1	0.85	0.5
Porphyry Intrusion	500	-	-	-	-	-	-	-
<b>Model 3</b>	$\rho_{matrix}$	Phase 1	$\rho_{phase1}$	$f_{phase1}$	Multiple of $k$	$a_{phase1}$	$\frac{\alpha_{phase1}}{sec^c}$	$C_{phase1}$
Geologic Unit	Ohm-m		Ohm-m	%		mm		
Cover Sediments	20	-	-	-	-	-	-	-
Pre-porphyry Rocks	200	-	-	-	-	-	-	-
Country Rocks	1000	-	-	-	-	-	-	-
Leached Cap			not present in model					
Enriched Zone			not present in model					
Pyrite Shell		chalcopyrite shell	used to test IP effect of increased chalcopyrite					
Ore Zone	40	chalcopyrite	0.004	5	10	1	0.85	0.5
Porphyry Intrusion	500	-	-	-	-	-	-	-
<b>Model 4</b>	$\rho_{matrix}$	Phase 1	$\rho_{phase1}$	$f_{phase1}$	Multiple of $k$	$a_{phase1}$	$\frac{\alpha_{phase1}}{sec^c}$	$C_{phase1}$
Geologic Unit	Ohm-m		Ohm-m	%		mm		
Cover Sediments	20	-	-	-	-	-	-	-
Pre-porphyry Rocks	200	-	-	-	-	-	-	-
Country Rocks	1000	-	-	-	-	-	-	-
Leached Cap			not present in model					
Enriched Zone			not present in model					
Pyrite Shell	50	pyrite	0.3	5	10	2.5	0.5	0.75
Ore Zone			no economic mineralization, only pyrite present					
Porphyry Intrusion	500	-	-	-	-	-	-	-

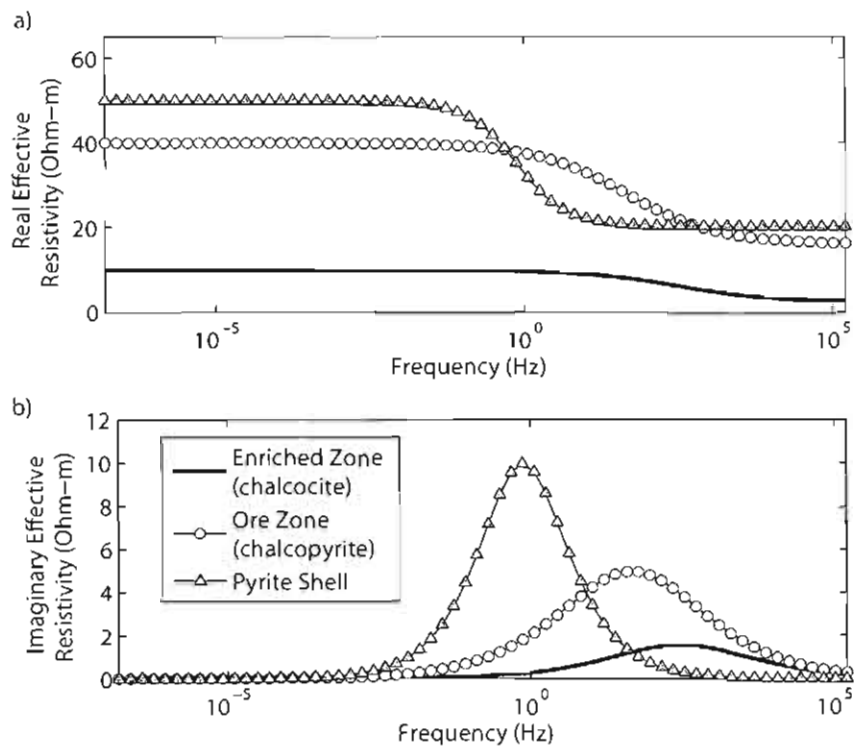


**Figure 3.6.** GEMTIP plots for Porphyry Model units with IP behavior. a) Real effective resistivity. b) Imaginary effective resistivity



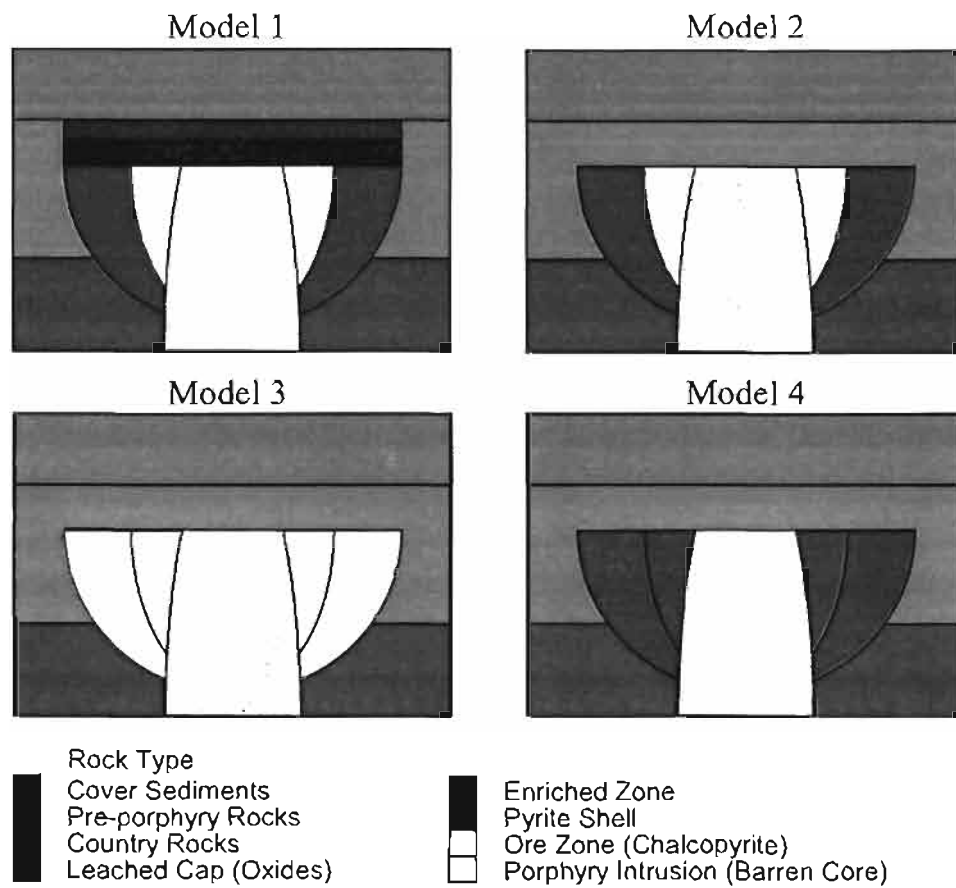
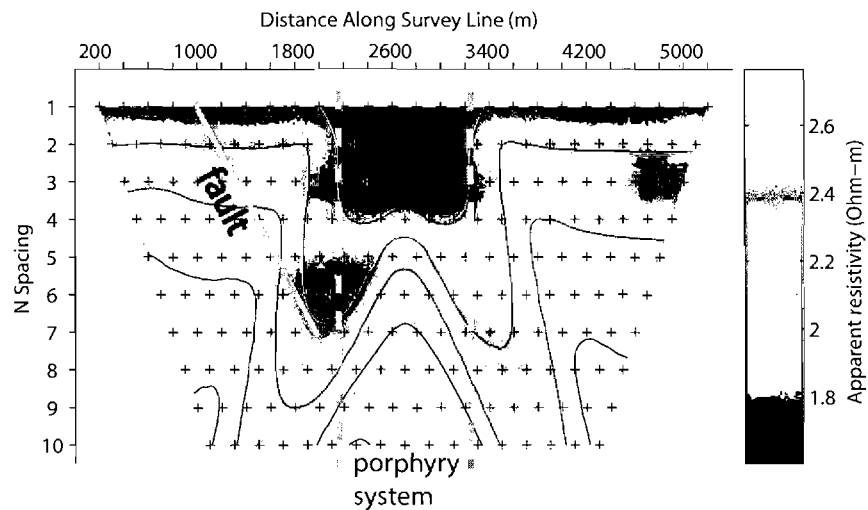
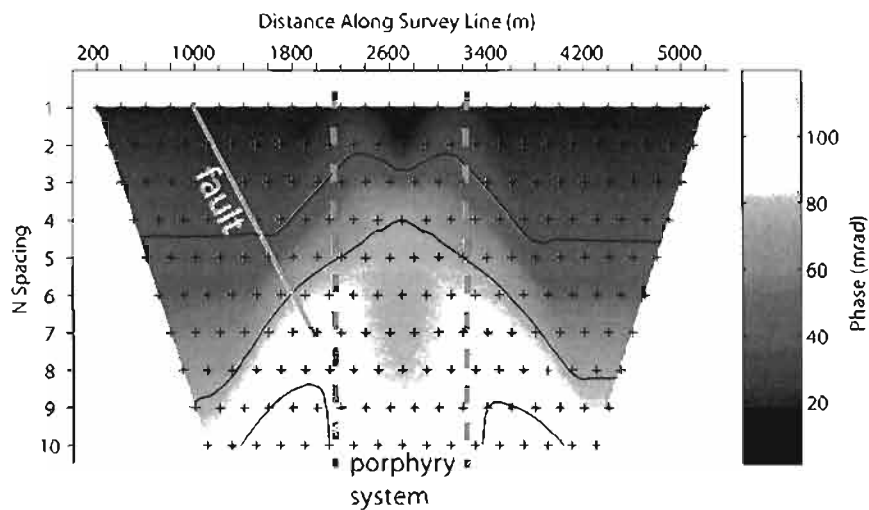


Figure 3.7. Cross sections of Models 1, 2, 3, and 4.



**Figure 3.8.** Model 1 apparent resistivity pseudosection for 1 Hz data. For this 200 m dipole-dipole survey configuration an N-spacing of three would indicate the center transmitting dipole is 600 m from the center of the receiving dipole. N-spacing can be difficult to correlate directly with depth; therefore pseudo sections are better at giving horizontal information. A conductivity low blankets the mineralized porphyry system in the center. Influence of the fault is seen in the right side of the pseudosection where the apparent resistivity is higher and creates left to right asymmetry in the response produced by the ore body. This representation of the data is useful in finding the horizontal extent of the ore body, but does not accurately indicate depth to the ore body or vertical extent. An inversion may be useful to determine these parameters.



**Figure 3.9.** Model 1 apparent phase pseudosection for 1 Hz data. Apparent phase is computed from the angle formed between the real and imaginary part of the apparent resistivity. A phase anomaly due to the ore body is symmetric about the center. Phase anomalies can indicate the presence of sulfide mineralization. Influence of the fault is not seen in the phase data as it does not have a strong IP response. Again, this representation of the data is useful in finding the horizontal extent of the ore body, but does not indicate depth to the ore body or vertical extent.

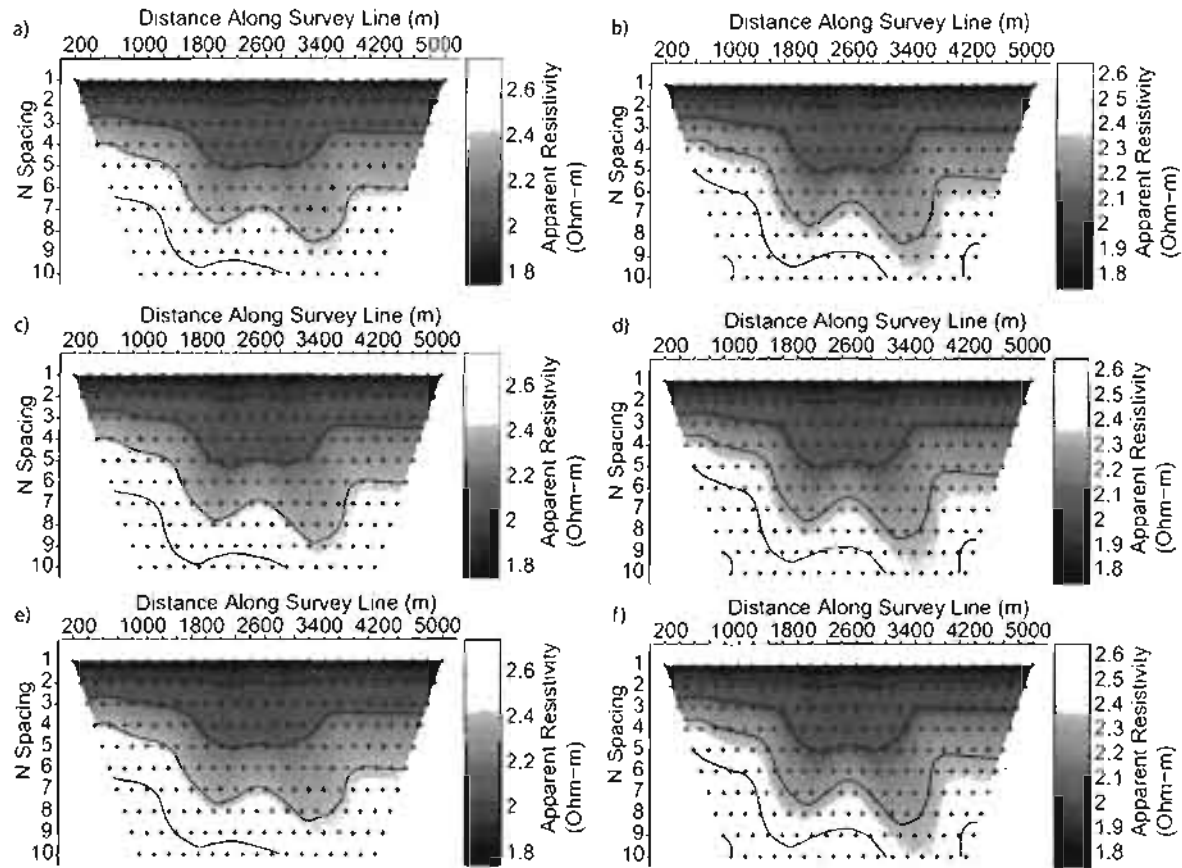


Figure 3.10. Apparent resistivity pseudosections. The apparent resistivity pseudosections for 1 Hz and 8 Hz data are similar for all Models 2 through 4. Table 3.4 gives an overview of each model. a) Model 2, 1 Hz data. b) Model 2, 8 Hz data. c) Model 3, 1 Hz data. d) Model 3, 8 Hz data. e) Model 4, 1 Hz data. f) Model 4, 8 Hz data.

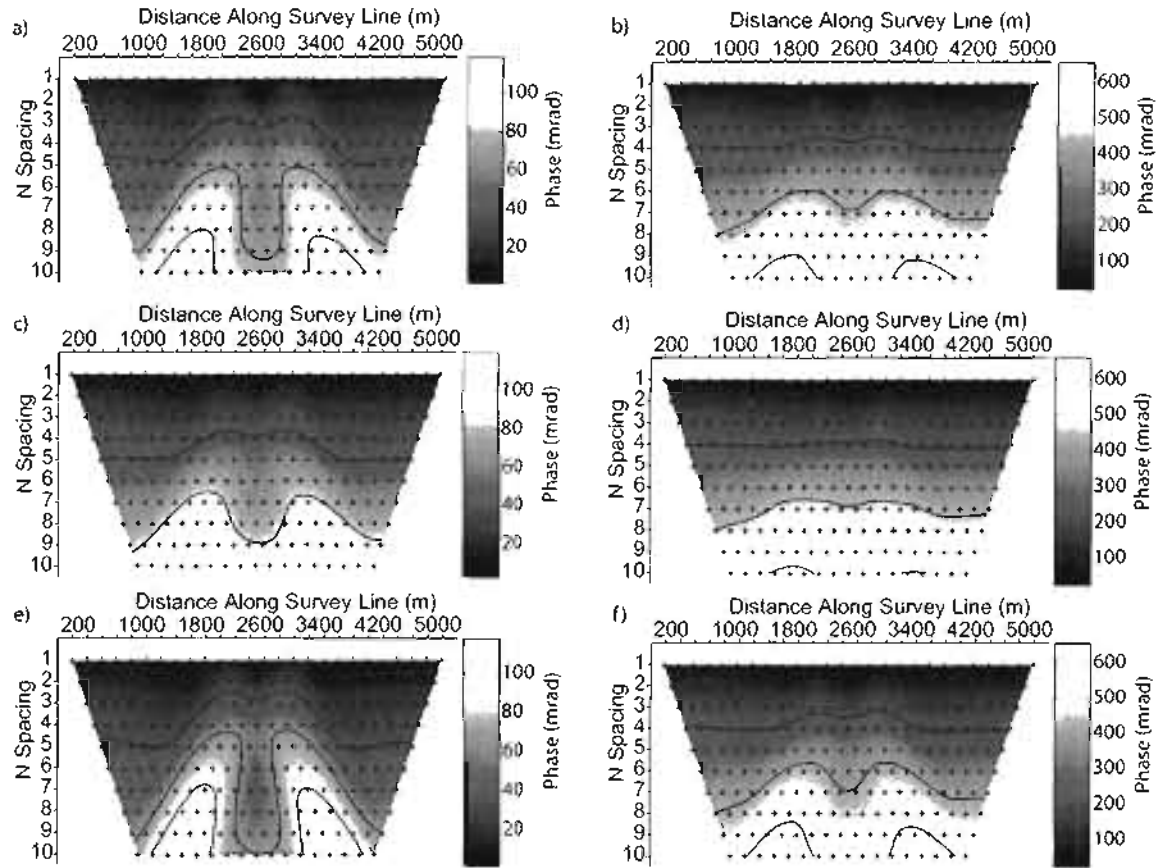
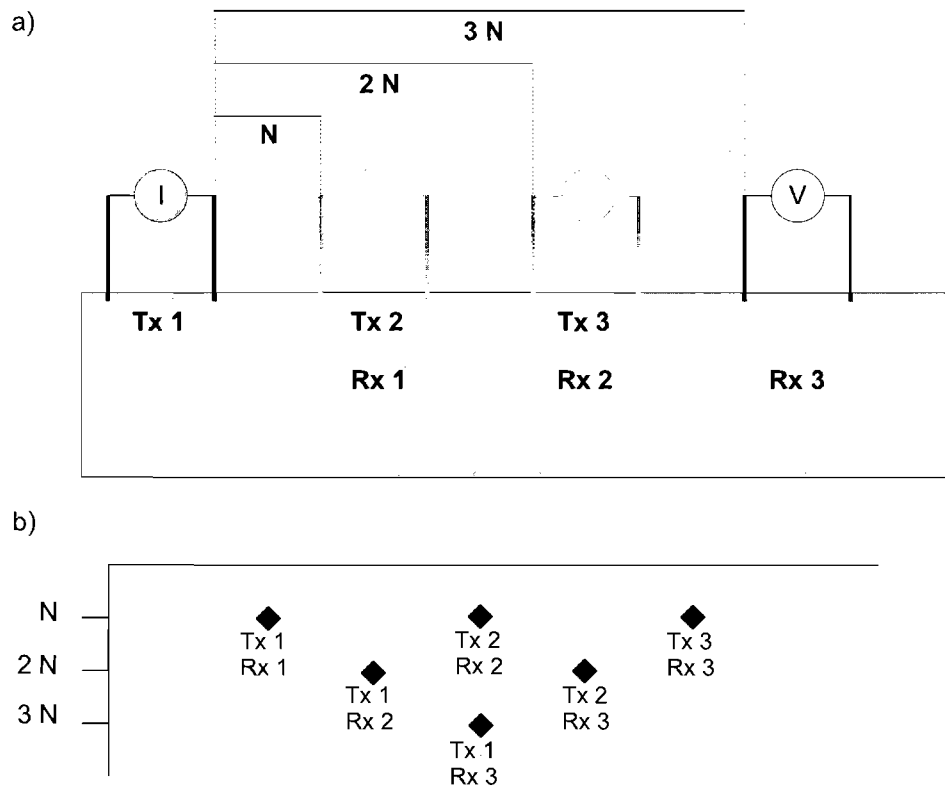


Figure 3.11. Apparent phase pseudosections. The apparent phase pseudosections for 1 Hz and 8 Hz different for Models 2 through 4 with the all pyrite model showing the largest phase response. The differences in the plots show the importance of understanding the complex resistivity and using it for interpretation. a) Model 2, 1 Hz data. Detail of each model as located in Table 3.4. b) Model 2, 8 Hz data. c) Model 3, 1 Hz data. d) Model 3, 8 Hz data. e) Model 4, 1 Hz data. f) Model 4, 8 Hz data.



**Figure 3.12.** Dipole-dipole survey and pseudosection plotting illustration. A pseudosection is created by plotting the computed apparent resistivity and phase as a function of  $N$ -spacing and horizontal position.  $N$ -spacing refers to the separation of the transmitting dipole and receiving dipole as a multiple of the dipole spacing. Apparent phase is the angle formed between the real and imaginary part of the apparent resistivity. a) Transmitting (Tx) and receiving (Rx) electrodes shown. b) Apparent resistivity values computed from transmitter and receiver pairs listed are plotted as a function of  $N$  spacing.

## CHAPTER 4

### CONCLUSIONS

#### 4.1 Conclusions

A new conductivity model based on Effective Medium Theory is presented. Using published data as a comparison, GEMTIP produced the same trend of peak IP frequency as a function of grain size. Inversion routines to recover the two empirical parameters  $\alpha$  and  $C$  were developed. X-ray tomography, and optical mineralogy were used to determine the composition and structure of the rock samples. The X-ray tomography proved useful in understanding the complex geometries, grain sizes, and surface area to volume relationships of the disseminated sulfides. Complex resistivity values were computed from multifrequency EM measurements collected from 0.0156 Hz to 9216 Hz. The combination of complex resistivity data and careful mineralogical assessment provided a good data set to assess the GEMTIP conductivity model. The spherical case of GEMTIP can fit measured data, but it is evident that the spherical case does not fully represent the complex nature of the disseminated sulfides. GEMTIP modeling for Sample K01 was most successful due to the relatively simple sulfide grain geometries. The derived term  $m$  should reflect the surface area per unit volume. It is possible that the term  $\tau$  could also be changed to reflect effective radius or surface area to better represent the complex geometries observed. This study provides encouraging evidence of that the GEMTIP model is truly describing the observed IP phenomenon.

To test the deposits scale effect of changes in sulfide distribution the Simplified Porphyry Model was developed to for modeling using the CEMI EM forward modeling code IBCEM3DIP. A new front end for this code was developed to to handle the complex geometry of a porphyry deposit. The GEMTIP conductivity model was added to IBCEM3DIP. Each sulfide zone was given unique IP parameters

based on observed data [*Pelton et al.*, 1978; *Ostrander and Zonge*, 1978]. Changes in chalcopyrite and pyrite distribution had significant effect on the phase data. The resistivity pseudosections had little variation when chalcopyrite and pyrite distribution was changed. This underscores the value of IP data over standard resistivity data and its ability to discriminate between sulfides.

The 3-D modeling example presented shows how grain-scale information effects deposit scale data. Additional simulations can easily be accomplished to assess optimal survey design, ore body detectability, and sulfide discrimination with

The 3-D forward modeling study in combination with the rock scale inversion techniques developed provide the framework for 3-D inversion of the individual parameters of the GEMTIP conductivity model and a better understanding of the IP effect from the grain scale to the deposit scale leading the way to mineral discrimination.

## 4.2 Future Directions / Recommendations

With these promising first results new forms of  $m$  and  $\tau$  should be investigated to more accurately represent the disseminated mineral forms found in nature and reflect surface area to volume ratios of the modeled phases. Once new analytic solutions are developed more studies should be conducted with a greater variety and number of rock samples to continue to test GEMTIP.

One possibility would be a more controlled experiment than the current using synthetic rocks composed of a known matrix and ball bearings homogeneously distributed. This would allow complete control of volume fraction, radius, surface area, grain resistivity, and matrix resistivity. To test elongated shapes, needle bearings could be used. Improved data collection techniques could also aid in the testing of GEMTIP. GEMTIP sets the stage for rock composition discrimination for EM methods.



## APPENDIX A

### EM DATA

Sample ID	Zonge ID	Frequency (Hz)	Normalized Magnitude	Total Resistivity (Ohmm)	Phase (mrad)
K01	12	0	1	81.53	0
K01	12	0.0156	1.00	55.05	43.16
K01	12	0.0469	0.97	53.24	60.15
K01	12	0.0781	0.95	52.17	71.24
K01	12	0.1094	0.94	51.44	78.45
K01	12	0.125	0.93	51.16	81.34
K01	12	0.1406	0.93	50.88	84.28
K01	12	0.375	0.87	48.11	111.51
K01	12	0.625	0.84	46.34	126.96
K01	12	0.875	0.82	45.06	136.83
K01	12	1	0.81	44.55	140.46
K01	12	1.125	0.80	44.05	144.17
K01	12	3	0.73	39.91	161.38
K01	12	5	0.69	37.78	162.47
K01	12	7	0.66	36.45	159.60
K01	12	8	0.65	35.98	157.88
K01	12	9	0.65	35.52	156.13
K01	12	24	0.59	32.47	134.66
K01	12	40	0.57	31.24	119.90
K01	12	56	0.56	30.56	110.73
K01	12	64	0.55	30.33	107.29
K01	12	72	0.55	30.10	103.81
K01	12	192	0.52	28.72	82.01
K01	12	320	0.51	28.17	73.87
K01	12	448	0.51	27.86	70.26
K01	12	512	0.50	27.76	68.95
K01	12	576	0.50	27.65	67.63
K01	12	1024	0.50	27.34	68.16
K01	12	1536	0.49	26.92	67.34
K01	12	2560	0.48	26.60	72.50
K01	12	3072	0.48	26.59	78.75
K01	12	3584	0.48	26.38	82.16
K01	12	4608	0.48	26.17	89.97
K01	12	5120	0.48	26.24	96.86
K01	12	7168	0.47	25.86	122.71
K01	12	9216	0.46	25.42	144.48

Sample ID	Zonge ID	Frequency (Hz)	Normalized Magnitude	Total Resistivity (Ohmm)	Phase (mrad)
M02	14	0	1	55.00	0
M02	14	0.0156	1.00	4729.05	96.10
M02	14	0.0469	0.94	4404.57	113.80
M02	14	0.0781	0.90	4244.95	119.02
M02	14	0.1094	0.88	4121.95	118.46
M02	14	0.125	0.87	4088.19	121.62
M02	14	0.1406	0.86	4054.41	124.83
M02	14	0.375	0.80	3746.32	125.91
M02	14	0.625	0.76	3595.88	126.23
M02	14	0.875	0.74	3503.05	126.29
M02	14	1	0.74	3468.46	126.05
M02	14	1.125	0.73	3433.82	125.82
M02	14	3	0.68	3186.31	124.55
M02	14	5	0.65	3064.54	124.16
M02	14	7	0.63	2986.90	123.66
M02	14	8	0.63	2958.52	123.47
M02	14	9	0.62	2930.19	123.28
M02	14	24	0.58	2725.22	121.88
M02	14	40	0.56	2624.07	120.94
M02	14	56	0.54	2560.38	119.62
M02	14	64	0.54	2538.04	119.41
M02	14	72	0.53	2515.69	119.19
M02	14	192	0.50	2346.82	117.91
M02	14	320	0.48	2263.29	119.68
M02	14	448	0.47	2209.96	119.12
M02	14	512	0.47	2190.40	119.58
M02	14	576	0.46	2170.85	120.04
M02	14	1024	0.45	2108.53	120.16
M02	14	1536	0.43	2026.61	120.79
M02	14	2560	0.42	1955.62	127.20
M02	14	3072	0.41	1952.08	129.26
M02	14	3584	0.41	1909.39	133.50
M02	14	4608	0.40	1873.14	140.59
M02	14	5120	0.40	1880.69	144.66
M02	14	7168	0.39	1826.21	167.18
M02	14	9216	0.38	1780.18	193.87

Sample ID	Zonge ID	Frequency (Hz)	Normalized Magnitude	Total Resistivity (Ohmm)	Phase (mrad)
SB03	1	0	1	4707.50	0
SB03	1	0.0156	1.00	81.57	32.62
SB03	1	0.0469	0.98	79.72	31.59
SB03	1	0.0781	0.97	78.98	31.32
SB03	1	0.1094	0.96	78.45	31.06
SB03	1	0.125	0.96	78.24	30.57
SB03	1	0.1406	0.96	78.03	30.09
SB03	1	0.375	0.94	76.66	28.81
SB03	1	0.625	0.93	75.95	28.05
SB03	1	0.875	0.93	75.50	27.45
SB03	1	1	0.92	75.33	27.26
SB03	1	1.125	0.92	75.17	27.08
SB03	1	3	0.91	73.99	25.77
SB03	1	5	0.90	73.42	25.24
SB03	1	7	0.90	73.06	25.21
SB03	1	8	0.89	72.92	25.20
SB03	1	9	0.89	72.77	25.18
SB03	1	24	0.88	71.77	26.14
SB03	1	40	0.87	71.22	27.62
SB03	1	56	0.87	70.87	29.05
SB03	1	64	0.87	70.73	29.72
SB03	1	72	0.87	70.60	30.39
SB03	1	192	0.85	69.40	39.30
SB03	1	320	0.84	68.64	47.04
SB03	1	448	0.83	68.08	53.65
SB03	1	512	0.83	67.85	56.74
SB03	1	576	0.83	67.62	59.86
SB03	1	1024	0.82	66.50	75.06
SB03	1	1536	0.80	65.18	94.22
SB03	1	2560	0.78	63.31	119.88
SB03	1	3072	0.77	62.54	130.26
SB03	1	3584	0.76	61.76	141.74
SB03	1	4608	0.74	60.32	161.02
SB03	1	5120	0.73	59.64	168.65
SB03	1	7168	0.70	56.81	200.12
SB03	1	9216	0.66	53.84	219.14

## APPENDIX B

### ELECTRONIC DATA

The included DVD-Data disk contains EM Data, rock sample photos, X-Ray tomography data, thesis source files.

#### **Folder EMdata**

This folder contains complex resistivity measurements for 16 rock samples in Excel and comma delimited text format. Also included are notes from measurement and Zonge reference materials.

#### **Folder RockSamplePhotos**

This folder contains rock sample photos in JPEG format and rock sample database in both Excel and comma delimited text formats

#### **Folder XrayTomography**

This folder contain the X-ray tomography data in four subfolders: **Voxel**, **Polygon**, **Movies**, and **Grains**. Subfolder Voxel contains the voxel data in UN-SINT8 format which can be viewed using the Windows program 3DView available for free from [http://www.rmrsystems.co.uk/volume\\_rendering.htm](http://www.rmrsystems.co.uk/volume_rendering.htm) or other similar voxel imaging program. Voxel data files have extension "raw". The files with extension "sct" explain the voxel data file format. Subfolder Polygon contain ASCII polygon mesh files created using the Marching Cubes technique [*Lorensen and Cline*, 1987]. These files can be viewed with Mesh Viewer found at <http://mview.sourceforge.net/>. The subfolder Movies contains video clips of the X-ray tomograpahy images in AVI format. A catalogs grain volume fraction for each volume of data are contained in the subfolder Grains in comma delimited text format.

#### **Folder Thesis**

Latex source files for this thesis and figures in encapsulated postscript format (in subfolder figs)

## REFERENCES

- Arce, J. R. (2006), High resolution 2D and 3D modeling of IP anomalies for various gold bearing deposits in Peruvian mining and exploration programs using the Pole-Pole array, (min 2.7), in *76th Annual International Meeting*, Society of Exploration Geophysicists.
- Cole, K. S., and R. H. Cole (1941), Dispersion and absorption in dielectrics, *Journal of Chemical Physics*, *9*, 289–300.
- Collett, L. S., and T. J. Katsube (1973), Electrical parameters of rocks in developing geophysical techniques, *Geophysics*, *38*, 76–91.
- Cox, L. H., and M. S. Zhdanov (2007), New advances in fast rigorous 3D inversion of airborne electromagnetic data, in *Proc. Ann. Mtg.*, Consortium for Electromagnetic Modeling and Inversion.
- Frasier, D. C. (1964), Conductivity spectra of rocks from the Craigmont ore environment, *Geophysics*, *29*, 832–847.
- Goold, J., L. H. Cox, and M. S. Zhdanov (2007), Integral equation method for 3-D modeling of electromagnetic fields in complex structures with inhomogeneous background conductivity, in *Proc. Ann. Mtg.*, Consortium for Electromagnetic Modeling and Inversion.
- Hohmann, G. W. (1975), Three-dimensional induced polarization and electromagnetic modeling, *Geophysics*, *40*, 309–324.
- Lee, S. K., and M. S. Zhdanov (2005), Integral equation method for 3-D modeling of electromagnetic fields in complex structures with inhomogeneous background conductivity, in *Proc. Ann. Mtg.*, Consortium for Electromagnetic Modeling and Inversion.
- Li, Y., and D. W. Oldenburg (2000), 3-D inversion of induced polarization data, *Geophysics*, *65*, 1931–1945.
- Lorenson, W. E., and H. Cline (1987), Marching cubes: A high resolution 3D surface construction algorithm, in *Proceedings of the 14th annual conference on Computer graphics and interactive techniques*, p. 163169, SIGGRAPH: ACM Special Interest Group on Computer Graphics and Interactive Techniques.
- Lou, Y. (1998), *Theory and application of spectral induced polarization*, Society of exploration geophysicists, 268 p.

- Mahan, M. K., J. D. Redman, and D. W. Strangway (1986), Complex resistivity of synthetic sulphide bearing rocks, *Geophysical Prospecting*, *34*, 743–768.
- Major, J., and J. Silic (1981), Restrictions on the use of Cole-Cole dispersion models in complex resistivity interpretation, *Geophysics*, *46*, 916–831.
- Maxwell, J. C. (1891), *A treatise in electricity and electromagnetism (1959 edition)*, Dover Publications, New York, 224 pp.
- Miller, J. D., and C. L. Lin (2004), Three-dimensional analysis of particulates in mineral processing systems by cone beam X-ray microtomography, *Minerals & Metallurgical Processing*, *21*(3), 113–124.
- Nabighian, M. N. (1988), *Electromagnetic Methods in Applied Geophysics*, *01*, Society of Exploration Geophysicists, 528 p.
- Oldenburg, D. W., and Y. Li (1994), Inversion of induced polarization data, *Geophysics*, *59*, 1327–1341.
- Olhoeft, G. R. (1985), Low frequency electrical properties, *Geophysics*, *50*, 2492–2503.
- Ostrander, A. G., and K. L. Zonge (1978), Complex resistivity measurements of sulfide-bearing synthetic rocks, in *48th Ann. Internat. Mtg.*, Society of Exploration Geophysicists.
- Pelton, W. H., J. G. Ward, J. G. Hallof, W. R. Sill, and P. H. Nelson (1978), Mineral discrimination and removal of inductive coupling with multifrequency IP, *Geophysics*, *43*, 588–609.
- Pierce, F. W., and J. G. Bolm (1995), *Porphyry Copper Deposits of the American Cordillera*, *Arizona Geological Society Digest 20*, Arizona Geological Society Digest 20.
- Reynolds, J. M. (1998), *An Introduction to Applied and Environmental Geophysics*, John Wiley and Sons.
- Schwartz, G. (1962), A theory of low-frequency dielectric dispersion of colloidal particles in electrolyte solution, *Journal of Physical Chemistry*, *66*, 2636–2642.
- Seigel, H. O. (1959), Mathematical formulation and type curves for induced polarization, *Geophysics*, *24*, 547–565.
- Seigel, H. O., H. Vanhala, and S. N. Sheard (1997), Some case histories of source discrimination using time-domain spectral IP, *Geophysics*, *62*, 1394–1408.
- Sillitoe, R. H. (1973), The tops and bottoms of porphyry copper deposits, *Geophysics*, *68*, 799–815.

- Slater, L. (2006), Near surface electromagnetic characterization of hydraulic conductivity: from petrophysical properties to aquifer geometries, in *18th Electromagnetic Induction Workshop*, The International Association of Geomagnetism and Aeronomy.
- Sumner, J. S. (1976), *Principles of induced polarization for geophysical exploration*, Elsevier, New York, 277 pp.
- Titley, S. R. (1982), *Advances in Geology of the Porphyry Copper, Southwestern North America*, University of Arizona Press, 560 p.
- Vanhala, H., and M. Peltoniemi (1992), Spectral IP studies of Finnish ore prospects, *Geophysics*, *57*, 1545–1555.
- Wait, J. R. (1959), *The variable-frequency method*, Pergamon, Oxford.
- Wanamaker, P. E., G. W. Hohmann, and W. A. SanFilipo (1984), Electromagnetic modeling of three-dimensional bodies in layered earths using integral equations, *Geophysics*, *49*, 60–74.
- Wong, J. (1979), An electrochemical model of the induced-polarization phenomenon in disseminated sulfide ores, *Geophysics*, *44*, 1245–1265.
- Wong, J., and D. W. Strangway (1981), Induced polarization in disseminated sulfide ores containing elongated mineralization, *Geophysics*, *46*, 1258–1268.
- Wynn, J. C., and K. L. Zonge (1975), EM coupling, its intrinsic values, its removal and the cultural coupling problem, *Geophysics*, *40*, 831–850.
- Yoshioka, K. (2004), Development of fast methods of multitransmitter EM data inversion for mineral exploration, Ph.D. thesis, Department of Geology and Geophysics, University of Utah.
- Yoshioka, K., and M. S. Zhdanov (2005), Three-dimensional nonlinear regularized inversion of the induced polarization data based on the Cole-Cole mode, *Physics of the Earth and Planetary Interiors*, *150*, 29–73.
- Zhdanov, M. S. (2002), *Geophysical Inverse Theory and Regularization Problems*, 628 pp., Elsevier.
- Zhdanov, M. S. (2005), New geophysical technique for mineral exploration and mineral discrimination based on electromagnetic methods, u. S. Patent application U-3885.
- Zhdanov, M. S. (2006), Generalized effective medium theory of the complex resistivity of multi-phase heterogeneous rocks, in *Proc. Ann. Mtg.*, pp. 1–24, Consortium for Electromagnetic Modeling and Inversion.
- Zonge, K. L., and J. C. Wynn (1975), Recent advances and applications in complex resistivity measurements, *Geophysics*, *40*, 851–864.



Zonge, K. L., W. A. Sauck, and J. S. Sumner (1972), Comparison of time, frequency, and phase measurements in induced polarization, *Geophysical Prospecting*, 20, 626-648.